Effects of Histotripsy on Bacterial Viability in Suspension

Pratik Anirudha Ambekar

A dissertation

submitted in partial fulfillment of the

requirements for the degree of

Doctor of Philosophy

University of Washington

2025

Reading Committee:

Thomas Matula, Chair

Michael Bailey

Peter Dahl

Program Authorized to Offer Degree:

Mechanical Engineering

University of Washington

Abstract

Effects of Histotripsy on Bacterial Viability in Suspension

Pratik Anirudha Ambekar

Chair of the supervisory committee:
Thomas Matula
Department of Bioengineering

This dissertation explores the bactericidal effects of histotripsy, a cavitation-based focused ultrasound therapy, on two bacteria in suspension namely *Escherichia coli* and *Staphylococcus aureus*, for potential application in abscess treatment. Abscesses are localized encapsulated collections of pus and bacteria that present a clinical challenge. Histotripsy can non-invasively reduce the bacterial burden in the abscess by rupturing bacterial cell walls via intense cavitation. To understand histotripsy process on bacteria in suspension, two regimens of histotripsy (shock-scattering histotripsy and boiling histotripsy) were applied *in vitro* on bacterial suspensions at frequencies ranging from 0.81 MHz to 3.25 MHz, at 1% duty cycle, and bacterial viability was quantified by the plate count assay. Cavitation was quantified by passive cavitation detection, plane-wave B-mode imaging and high-speed photography. Results showed that both regimens reduced *E. coli* counts significantly. Cavitation cloud size in shock-scattering histotripsy quantified

by high-speed photography strongly predicted the *E. coli* inactivation. Subsequently, plane-wave B-mode imaging was applied to estimate cavitation cloud size enabling the prediction of *E. coli* inactivation rates in future clinical studies. On the other hand, *Staphylococcus aureus* was resistant to histotripsy treatment. Efforts were made to obtain bactericidal activity by de-clumping *S. aureus* clusters into individual cells, treating smaller volumes, and combining histotripsy with heating, with negligible response. Finally, an investigation was conducted to determine the effect of bacterial shape and gram status on their resistance to histotripsy treatment.

TABLE OF CONTENTS

LIST OF FIGURES

LIST OF TABLES

ACKNOWLEDGEMENTS

My PhD would not have been completed without the support of many people. Indeed, I feel like I am standing on the shoulders of giants. I feel lucky to be a part of a research group defined by respect, passion, and dedication. First, I would like to express my sincere gratitude to my advisor Dr. Thomas Matula for his guidance, mentorship, and unwavering support throughout the journey. I am also immensely grateful to Dr. Tatiana Khokhlova for always taking time to talk whenever I stopped by, never making me feel like I was intruding. I would also like to thank the rest of my thesis committee Drs. Michael Bailey, Peter Dahl, and Alexander Meeske for their guidance and valuable insights.

A special thanks to Dr. Yak-Nam Wang for teaching me by example how to be organized, efficient, and approach problems with a scientific mindset. I am deeply grateful to CIMU members Stephanie Totten, Shelby Piersonn, Drs. Gilles Thomas, Pavel Rosnitskiy, Daniel Leotta, Wayne Kreider, Matthew Bruce, Adam Maxwell, and Mohamed Ghanem for their inputs, guidance, and collaboration. I would also like to thank the clinical collaborators in the abscess group, Drs. Conrad Liles, Keith Chan, Patchen Dellinger, Adeyinka Adedipe, and Wayne Monsky for their suggestions and encouragement. My research would not have been realized without the collaboration with enthusiastic, resourceful, and creative engineers at CIMU – Kaizer Contreras, David Giraud, and Ekaterina Kuznetsova. No words of gratitude are enough to do justice to their contributions to my research.

My PhD experience was enriched by the presence of my fellow graduate students, Gerald Lee, Drs. Minho Song, and Yashwanth Nanda Kumar. I enjoyed our discussions on a variety of topics ranging from science, culture, to random curiosities. Special thanks to Minho for answering my

countless questions on fundamental acoustics, and for repeatedly helping me troubleshoot technical issues. Additionally, I would like to thank Yash for introducing me to CIMU and always helping me professionally and personally during difficult times.

I would like to acknowledge my teachers who played an important role in my intellectual development and in igniting my interest in science, without whom I wouldn't be on this path today. These include Dr. Nitin Narappanawar, Gogate Madam, Ketan Dandare Sir, Prof. Mike Averkiou, and Prof. Peter Dahl.

Last but not the least, I would like to thank my family and friends for making my life enjoyable, purposeful, and fulfilling. Their constant encouragement helped me stay balanced and motivated.

DEDICATION

To my parents Amita and Anirudha Ambekar, whose hard work, sacrifices, and unwavering support made it possible for me to follow my dreams

Chapter 1. INTRODUCTION

This dissertation is part of a research project aimed at treating abscesses by a focused ultrasound-based ablation technique called histotripsy. Abscesses are infected, walled-off collections of pus and bacteria, that present a significant healthcare challenge. Current abscess treatment methods are invasive in nature which carry significant risks and have limited efficacy in certain cases. Histotripsy is a non-invasive therapeutic technique that induces a cluster of micron-sized, strongly expanding and collapsing gas bubbles at a localized target region in the body. These bubbles impart high stresses on adjacent structures like tissues and bacteria, thus can potentially reduce the viable bacterial load inside the abscess. Proof-of-concept studies were conducted with *in vivo* abscess models, but bacterial inactivation showed a high variability because of uncontrolled experimental parameters like abscess volumes, gas content, treatment times, and initial bacterial concentrations. Hence, it was necessary to take a step back and investigate the bactericidal effects of histotripsy in controlled experimental conditions.

1.1. CLINICAL PROBLEM – ABSCESS

Abscesses are localized, infected collections of pus and bacteria that are walled off by highly vascular capsules and can appear anywhere in the body. Abscesses are formed as a defense mechanism by the host's immune system to encapsulate an infection when the immune cells are unsuccessful in eliminating invading pathogens. Common abscess formation sites include skin [1], brain [2], dental [3], but they can form at any internal and external locations in the body. The size ranges from 1–5 cm in diameter. Some abscesses may be multiloculated i.e. having multiple internal compartments or pockets separated by internal walls.

Abscesses represent a significant healthcare challenge in the United States, with a substantial

economic burden. Infection rates increased from 1.2 million emergency department visits in 1993 to 3.4 million visits in 2005 [4]. In an urban pediatric hospital, 2090 abscess cases were treated in one year [5]. The Agency for Healthcare Research and Quality reported that >262,000 U.S. patients were hospitalized for abscess treatment, which resulted in approximately $6.2 billion aggregate U.S. hospital charges in 2011. Abdominal abscesses rank among the top 10 diseases for the highest 30-d re-hospitalization rate [6].

Several therapeutic approaches are undertaken to treat and resolve abscesses depending on their location, size, and complexity. Abscesses that occur deep in the body are generally treated by image-guided percutaneous catheter drainage, using CT or MRI. The most common approach for treating cutaneous abscesses is incision and drainage. Abscesses that are difficult to drain due to loculation, viscosity, and close proximity to vital structures may require surgical washout procedures. In case there is a concern for bacterial spread after treatments, antibiotics are prescribed.

With the current approaches of treating abscesses, several concerns arise for patients as well as physicians. The quality of life of patients significantly reduces even if drainage is being successful, because of inconvenience in daily activities like sitting or walking, along with constant follow-up visits to the hospital for CT and drainage. Physician concerns include the potential for antibiotic resistance, radiation exposure to the patient and themselves during CT. Additionally, CT-guided percutaneous drainage has only 50% success rate as reported in a study [7]. Moreover, all therapeutic approaches listed above are invasive, which carries risks of complications like secondary infections from drainage tubes, bleeding, and injury to adjacent healthy tissues and organs.

A non-invasive procedure to sterilize and resolve abscesses would have widespread clinical

applications. Histotripsy non-invasively liquefies target tissue by mechanical means making it a strong choice for abscess treatment. The next sub-section introduces relevant concepts and highlights a hypothesized non-invasive abscess treatment procedure using histotripsy.

1.2. SOLUTION – HISTOTRIPSY TREATMENT OF ABSCESSES

Histotripsy is fundamentally an ultrasound-based technique. Ultrasound refers to the propagation of sound waves above the frequency of 20,000 Hz. Ultrasound technology works on the principle of piezoelectric effect which was discovered by Pierre and Jacques Curie in 1880. Since then, it has been used for many applications including underwater visualization, material defect identification, and industrial cleaning. In medical settings, low intensity (<1 W/cm^2) ultrasound is commonly used as a non-invasive diagnostic tool for visualizing different regions in the body, whereas high-intensity ultrasound (nominally 100–10,000 W/cm^2) is used for therapeutic purposes. Specifically, high-intensity focused ultrasound (HIFU) is a therapeutic technique that causes localized thermal ablation of abnormal, unwanted tissues.

HIFU is realized by focusing high-frequency (nominally 0.5–3 MHz) sound waves through a medium such as tissue or water to a localized region. In this region, high intensity is created due to the convergence of the sound waves. Due to the absorption of this energy by the medium, the temperature of the focal region increases which leads to coagulative necrosis i.e. thermal destruction of tissue. However, a key limitation of HIFU is that nearby blood vessels can act as heat sinks, dissipating the thermal energy and preventing the focal region from reaching sufficient temperatures for complete tissue destruction.

Histotripsy is a mechanical version of HIFU that operates at a low duty cycle to minimize thermal damage resulting from heat accumulation. It uses microsecond long pulses of high amplitude delivered at a low duty cycle (1–2%) to create cavitation bubbles at the focal region.

Acoustic cavitation is the formation of vapor and gas bubbles by rarefactional pressures created by the acoustic wave. These cavitation bubbles when created in tissue by histotripsy, impart stresses and strains on adjacent tissue structures to disintegrate them at a sub-cellular level. This results in homogenized fluid lesions with sharp boundaries.

There are different types of histotripsy based on pulse duration and the resulting bubble dynamics. Shock-scattering histotripsy (CH - also called cavitation histotripsy) was invented in 2004 [8]. It uses 3–20 cycles with high-amplitude shock fronts, and peak negative pressures amplitudes of 15–25 MPa, to create millimeter sized clusters of bubbles commonly referred to as cavitation clouds. These clouds evolve throughout a pulse by backscatter and inversion of the individual shock fronts incident on bubbles in the central region of the focus (Figure 1.1b). Subsequent shock inversions enlarge the cluster for a few cycles until saturation [9].

Boiling histotripsy (BH) is another regimen of histotripsy which was first reported in 2009 [10]. It uses 1–20 milliseconds duration pulses at lower peak pressures (10 MPa–18 MPa) compared to shock-scattering histotripsy. Enhanced heat deposition through absorption at the shocks leads to rapid elevation of temperature up to 100°C in a very localized volume at the focus within as short as a few milliseconds, which in turn leads to the generation of a vapor bubble as illustrated in Figure 1e. The interaction of this vapor bubble with the remaining cycles of the pulse leads to tissue fractionation through a number of physical mechanisms [11], [12], [13].

An important aspect of histotripsy treatment is image-guidance, which is necessary for treatment monitoring. B-mode (brightness mode) is an ultrasound imaging method that uses acoustic backscatter from echogenic targets to produce a grayscale representation. It is the most ubiquitous parameter for histotripsy image guidance. Cavitation cloud appears hyper-echoic on a B-mode ultrasound image, whereas liquefied tissue in the absence of bubbles appears hypo-echoic

[14].

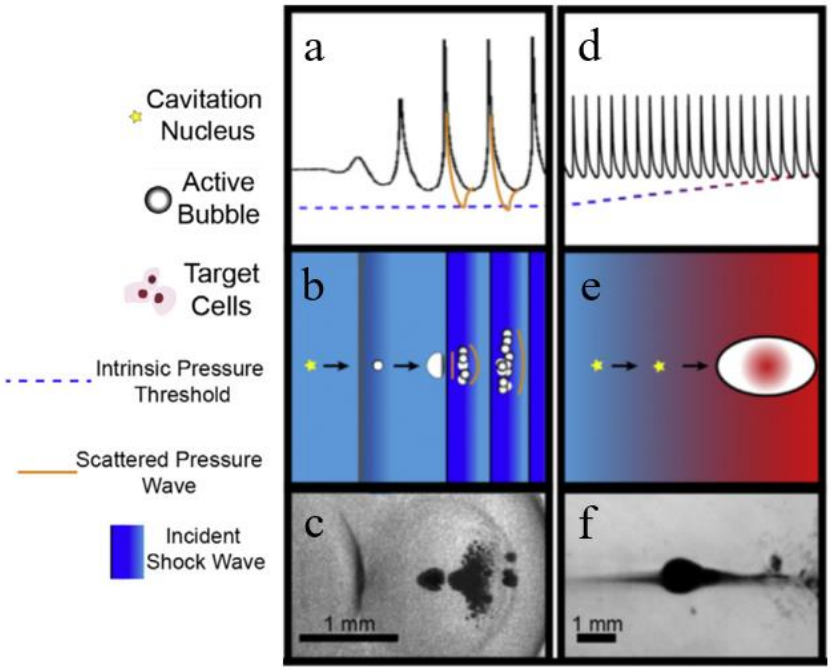

Figure 1.1. Histotripsy-induced cavitation dynamics [15]. Bubble sizes and nuclei are not to scale. a) Shock-scattering histotripsy pulse. The scattered pressure wave exceeds the intrinsic threshold. b) In shock-scattering histotripsy excitations, the activated nucleus grows slowly over the course of several cycles (left arrow) and deforms because of the incident shock waves (right arrow). Additional bubbles form spatially and temporally in regions of constructive interference between the incident wave and waves scattered by the deformed bubble. c) Representative high-speed photography images of shock-scattering histotripsy bubbles. d) Boiling histotripsy pulse. Intrinsic threshold is exceeded after cycles sufficient to lower during shock-enhanced heating. e) In boiling histotripsy, shock-enhanced heating alters the cavitation nucleus (left arrow) to reduce the requisite tension for bubble formation (right arrow). f) Representative high-speed photography images of boiling histotripsy bubbles.

Histotripsy has been used preclinically to treat tumors [16], biofilms [17], tendons [18], deep vein thrombosis [19], and clinically to treat benign prostate hyperplasia [20]. Similarly, histotripsy can be potentially used to treat abscesses in two ways, firstly by liquefying the abscess contents by the same mechanism mentioned for tissue. Secondly, histotripsy-induced cavitation can potentially inactivate bacteria inside abscesses, since acoustic cavitation has been successful in inactivating bacteria [21]. Figure 1.2 shows the hypothesized abscess treatment process. A histotripsy transducer will focus in the interior of the abscess to liquefy contents and inactivate

bacteria. Concern will be taken not to treat the capsule (marked by green outline in the image). The abscess content immediately adjacent to the capsule will be recirculated in the interior by cavitation-induced streaming.

If successful, histotripsy-based abscess treatment would have several advantages over current treatments. It is non-invasive and would involve less procedural pain and could treat abscesses too viscous for drainage. Additionally, since the interior environment of abscesses is acidic, antibiotics are generally ineffective. Moreover, bacteria like methicillin-resistant *Staphylococcus aureus* (MRSA) can develop antibiotic resistance. Histotripsy effects are mechanical in nature which can potentially overcome these challenges.

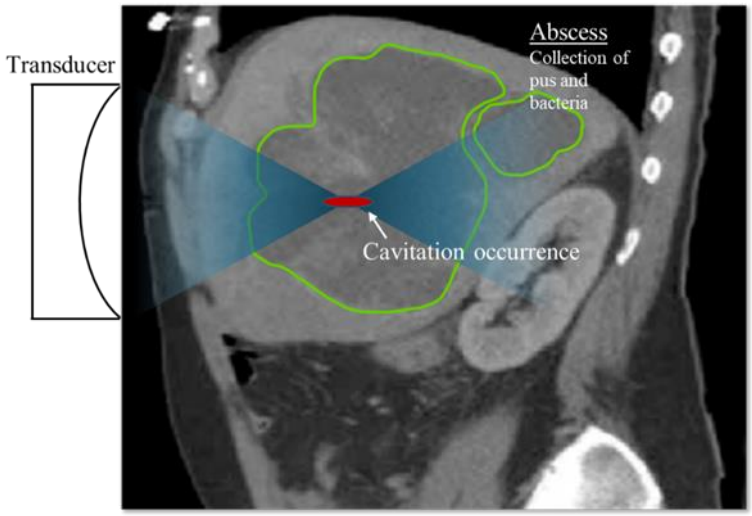

Figure 1.2. Hypothesized process of histotripsy-based abscess treatment. A CT scan of a deep abscess is shown. A transducer focuses the ultrasound beam in the abscess interior leading to formation of cavitation, which will liquefy the abscess contents and inactivate bacteria. Treating the whole abscess interior is possible by moving the focus under image-guidance and recirculation of contents close to the boundary into the focus by cavitation-induced streaming.

A pilot *in vivo* study was performed with both CH and BH on abscesses generated in a large animal (porcine) model, in which high variability was observed in both histotripsy regimens, especially for BH [22]. However, treatment durations and volumes were not controlled. Hence,

there was a need for a more controlled environment to study the dependence of bacterial inactivation on histotripsy parameters like treatment time, duty cycle, focal pressure amplitude, and pulse duration. Bacterial suspensions represent the simplest abscess model because of ease in accessibility, consistent gas content and viscosity, and increased control over temperatures and pre-treatment bacterial concentration across studies. Two bacteria were selected for treatments because of their common occurrence in abscesses, namely *Escherichia coli* (*E. coli*), and *Staphylococcus aureus* (*S. aureus*).

1.3. EFFECTS OF FOCUSED ULTRASOUND ON BACTERIAL VIABILITY

Acoustic fields have been known to inactivate bacteria for almost 100 years [23]. The fundamental mechanism of ultrasound-induced bacterial inactivation is mediated by cavitation and was explored in 1950s and 1990s [24], [25]. Bactericidal activity is suggested to be due to mechanical effects or sonochemical reactions produced by acoustic cavitation [26], [27], [28]. Mechanical effects are produced by pressure gradients during bubble collapse, shear forces induced by microstreaming during bubble oscillations, micro-jetting of bubbles during asymmetric collapse, and shock-waves generated by bubble collapse (Figure 1.3). Sonochemical effects are generated by the splitting of water molecules into free hydroxyl radicals (H* and OH*) because of the energy of cavitation collapse. These radicals attack the outer layers of a cell leading to chemical imbalance in the cell wall. Additionally, hydroxyl radicals can recombine into hydrogen peroxide which also has bactericidal effects and contributes to inactivation.

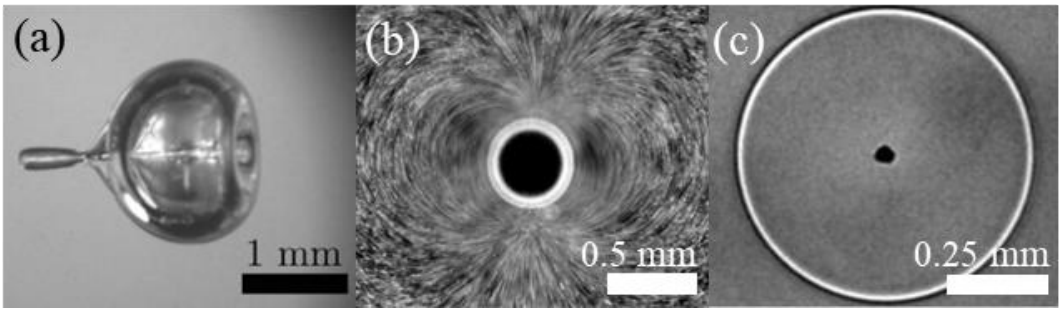

Figure 1.3. Mechanisms of ultrasonic cavitation damage to bacteria. a) Jetting of bubbles [29]. b) Microstreaming patterns during stable oscillation [30]. c) Shock wave emitted by a collapsing bubble [31].

A commonly used ultrasound-based setup to investigate bacterial inactivation is an ultrasonic horn, also known as ultrasonic probe. The setup consists of a tapering round metal rod with 5 mm–10 mm flat surface (horn tip) driven by a piezoelectric element. When the element is actuated at specific input electric powers and frequencies (20 KHz–500 KHz), the vibrations get transferred to the tip which translates as unfocused sound waves in the bacterial sample. This creates cavitation immediately below the tip inside the sample, if the rarefactional pressures are of enough amplitude to surpass threshold of cavitation formation. Horns have been used to study the dependence of bacterial inactivation on acoustic parameters like frequency [32], pulse duration [33], and intensity [34]. However, these setups cannot be used for abscess treatment related studies, since they cannot be inserted into the body.

In the last twenty years, HIFU and histotripsy have been used to treat biofilms, which are communities of bacteria encased in a self-produced matrix of extracellular polymeric substances (EPS) and attached to inert surfaces or living tissue. A research group conducted several investigations with different bacteria like *E. coli* [35], *S. aureus* [17], [36], and *Pseudomonas aeruginosa* (*P. aeruginosa*) [37], with the motivation of non-invasively treating biofilms attached to medical implants. The biofilms were grown *in vitro* on implant-mimicking surfaces like graphite disks and polypropylene meshes and were treated with shock-scattering histotripsy. Parametric

studies showed increased biofilm eradication at higher peak rarefactional focal pressure amplitudes, and negligible effect of the number of cycles in the pulse. Also, the scan speed was a critical parameter for efficient biofilm destruction. Overall, results showed significant biofilm eradication from surfaces, but it was unclear whether the bacteria dislodged from the biofilms were rendered non-viable.

Focused ultrasound has been used to treat bacteria in suspension. A study exposed *E. coli* suspensions enriched with cavitation nuclei with 1 MHz, 1000 cycle pulses at a spatial peak pulse average intensity of 500 W/cm^2, and used a 20 MHz transducer to passively detect noise emissions associated with symmetric bubble collapse [38]. A poor correlation of cavitation dose was observed with bacterial inactivation, potentially due to shielding of acoustic emissions by pre-focal bubbles. Two successive studies were conducted by a research group to gauge the performance of pulsed focused ultrasound with shocks on inactivating *E. coli* in suspension as a proof-of-concept study for histotripsy based abscess treatment [39], [40]. In the first study, 2-MHz focused ultrasound was used on 100 µL volumes to achieve >99% inactivation. Parametric studies showed an increasing dependence of inactivation on treatment time, whereas a peak rarefactional pressure threshold was observed. In the second study, a decreasing dependence of inactivation was observed with increasing volume. Importantly, transmission electron microscopy (TEM) images post-treatment showed broken cell walls, leaked cell contents and missing cytoplasm, which indicated mechanical inactivation mechanism. Another group used histotripsy on *P. aeruginosa* suspensions and obtained a 5 log kill (99.999% inactivation) in six minutes [41]. Overall, no study investigated the effects of histotripsy on abscess-causing bacteria like *E. coli* and *S. aureus* in suspension.

1.4. ORGANIZATION OF THE DISSERTATION

In the first chapter, background on abscesses, histotripsy, and effects of focused ultrasound on bacteria are explained. The second chapter is a comparative study between the two types of histotripsy – shock-scattering histotripsy and boiling histotripsy on inactivating the bacteria *E. coli* in suspension. For the rest of the dissertation, bactericidal effects of shock-scattering histotripsy are explored in detail. In the third chapter, the relationship between optically measured cavitation cloud size and *E. coli* inactivation was investigated. This relationship was further refined in the fourth chapter by normalizing the cavitation cloud size by bacterial suspension volume. In the fifth chapter, the potential of plane-wave B-mode imaging (a type of B-mode imaging) in tracking cavitation cloud size changes with increasing acoustic power is explored. The sixth chapter details the approaches to enhance *S. aureus* bactericidal activity following its observed resistance to histotripsy in preliminary treatments. In the seventh chapter, effects of bacterial shape and gram status on their resistance to histotripsy are investigated. Conclusions, implications of the dissertation to histotripsy-based abscess treatment, and recommended future work are stated in chapter 8.

Chapter 2. COMPARATIVE STUDY OF HISTOTRIPSY PULSE PARAMETERS USED TO INACTIVATE ESCHERICHIA COLI IN SUSPENSION

2.1. INTRODUCTION

An *in vivo* study applying shock-scattering histotripsy (CH) or boiling histotripsy (BH) to a porcine abscesses model suggested that, with respect to bactericidal effectiveness, BH was much more variable and less effective on average than CH [22]. Hence, in this chapter, similarities and differences between CH and BH for inactivating *E. coli* are quantified.

CH and BH have differences in bubble dynamics. Each CH pulse generates a smaller cavitation cloud than a BH pulse, but it is repeated at a higher PRF. Because of the difference in pulse duration, solid tissue displacement and/or liquid streaming induced by acoustic radiation force is more pronounced in BH treatments. The combination of the aforementioned effects results in BH lesions in tissue being larger than CH lesions within the same treatment time. In this chapter, typical parameters from both CH and BH regimens were selected. Exposures were performed with varying peak negative pressure amplitude and treatment time using the same fixed-focus, stationary 1 MHz transducer.

All studies used the same transducer and custom sample vial system. Instead of moving the transducer's focus through the sample volume, cavitation-induced streaming was relied on to circulate material through the focus. One advantage of histotripsy is that streaming induced at the focus brings new material into the focus via the acoustic radiation force (momentum imparted by

the wave on the liquid) and Kelvin impulse (momentum imparted by bubble oscillations on the liquid). Cavitation enhances streaming caused by the interaction between the sound wave and bubbles. Bubble oscillations themselves create microstreaming patterns that are also known to disrupt cells because of high transient shear forces [26]. Thus, the treatment volume is larger than the acoustic pressure focal volume. This was previously demonstrated in an *in vitro* study that used a fixed-focus system to treat a 10 mL sample by drawing bacteria into a comparatively small acoustic pressure focal volume [40].

The article is organized as follows. Variable peak negative pressure studies were performed to determine the threshold for *E. coli* inactivation. Treatment time studies were then performed at various pressure amplitudes above the threshold. For CH, different pulse parameters (pressure amplitude, pulse length, duty cycle) were compared. With BH, different pressure amplitudes were compared.

2.2. METHODS

2.2.1. Culture and Preparation

Escherichia coli FDA strain Seattle 1946 was purchased from the American Type Culture Collection (ATCC, Manassas, VA, USA) and maintained as streak cultures on 3% tryptic soy broth medium and 2% agar. Details of the methods used to prepare and use the bacteria have been described in detail earlier [39], except as noted. Bacterial growth was monitored by periodically measuring the optical density at 600 nm (OD600). The culture was used once the bacteria reached the stationary phase, as established from previous growth characteristic studies.

2.2.2. Histotripsy Exposure Apparatus and Treatment Protocols

A custom experimental apparatus (Figure 2.1) was used for these experiments. Vials containing the bacterial suspensions were immersed in a cylindrical degassed water bath (initially at ~20°C)

with an attached 1 MHz spherically focused transducer (F# = 1, aperture = 85 mm). The transducer was driven by a high-power driving electronics system (not shown, but detailed elsewhere [42]) and had a circular opening in the middle that harbored a coaxially aligned 64-element phased-array ultrasound imaging probe (ATL P4-2 probe, Phillips, Bothell, WA, USA). The imaging probe was attached to a Verasonics (Kirkland, WA, USA) V1 ultrasound system, and the position of the histotripsy transducer focus within the B-mode ultrasound image was pre-registered with the system. The cylindrical plastic exposure vials (48 mm tall, 19 mm inner diameter, 3 mm wall thickness) accommodated 10 mL samples. The bottom of the vials was fitted with a cling-film acoustically transparent "window" held in place by an O-ring, which nested in an annulus machined into the outer walls of the vials. After being filled with the desired sample, the vial was sealed with a friction-fitted cap containing two magnets that clamped against two magnets on the apparatus. This allowed reproducible alignment of replicate samples within the acoustic field. The bottom of the cap was machined into a cone with its point immersed in the sample to reduce acoustic reflections. When filled, a small air gap remained along the edge of the conical cap. The position of the vial corresponded to having the focus 15 mm from the bottom membrane, approximately at the center of the vial's 10 mL volume. Immediately prior to a new study, the water was degassed to $\leq$20% O_2 concentration. Over the treatment time, the water temperature and O_2 concentration were measured periodically with an O_2 meter (Oxi 3310, Xylem Analytics, Washington, DC, USA). Additionally, the proximal wall of the transparent acoustic window was wiped with a gauze sponge to remove pre-existing bubbles that could act as cavitation nuclei during treatments. During treatments, B-mode imaging and passive cavitation detection (described later) were used to look for pre-focal cavitation signals from the transparent acoustic window. None were observed.

Calibration of the acoustic focal pressure levels at a full range of system driving voltages was performed in degassed water with a fiberoptic probe hydrophone (FOPH 2000, RP Acoustics, Leutenbach, Germany; 100 μm active diameter, 100 MHz bandwidth). The sample holder was removed for characterization. The resulting peak positive and peak negative pressures and representative focal waveforms are illustrated in Figure 2.2. Both CH and BH regimens use the acoustic output corresponding to the formation of shocks at the focus; peak positive (p^+) and peak negative (p^-) focal pressures corresponding to fully developed shock formation (i.e., where p^+ is equal to shock amplitude [43]) were $p^+ = 76$ MPa and $p^- = 12$ MPa (red line in Figure 2.2a). Peak focal pressures corresponding to the maximum output level used in this work were $p^+ = 103$ MPa and $p^- = 23$ MPa. Most studies were performed at p^- ranging from 12 to 23 MPa.

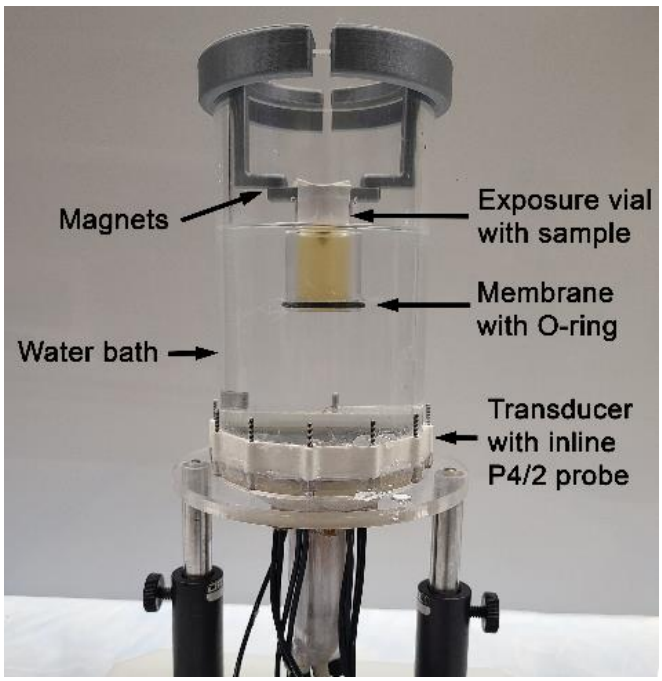

Figure 2.1. Custom experimental apparatus. A 1 MHz transducer with integrated inline P4/2 imaging probe was attached to the bottom of a degassed water bath. The apparatus was designed so that the transducer's focus was at the center of a sample vial containing 10 mL of *Escherichia coli* bacteria (~1×10^9 cells/mL). A thin acoustically transparent membrane was placed at the bottom of the vial for improved acoustic energy transmission. The vial was aligned to the transducer using two pairs of magnets to allow for fast, reproducible alignment of replicate samples.

Two different CH exposures (5 or 10 cycles at 2 or 1 kHz PRF, respectively) and one BH exposure (10,000 cycles at 1 Hz PRF) were used in most studies. Except where noted, a duty cycle of 1% was used for all exposures. In the first series of experiments, the focal pressure threshold for inactivation of *E. coli* was determined for each regimen. Each sample was treated for 10 minutes at different voltages corresponding to peak negative focal pressures ranging from 1 to 23 MPa. Once the amplitude dependence was established, the influence of treatment time, ranging from 5 to 40 minutes at a fixed pressure level, was investigated.

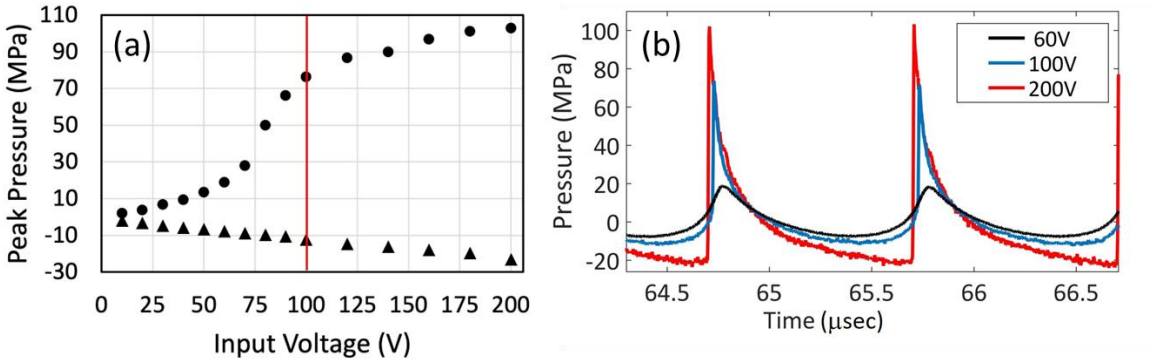

Figure 2.2. Transducer characterization. (a) Peak positive and negative amplitudes versus input voltage. Most studies were performed between peak negative pressure amplitudes of 12 and 23 MPa. The red line indicates the output level corresponding to fully developed shock formation. (b) Representative waveforms corresponding to the output levels below (black line) and above (blue and red lines) shock formation.

2.2.3. Viability Assessment

Samples withdrawn from the treated cell suspensions were subjected to serial dilutions with EPA dilution water (2 mM $MgCl_2$, 0.6 mM KH_2PO_4, pH 7.1) as a standard diluent for *E. coli* using aliquots no smaller than 25 µL, as described previously [39]. Compact Dry EC100 assay plates (Hardy Diagnostics, Santa Maria, CA, USA) were used for colony counting, on which *E. coli* specifically produces a blue colony while non-*E. coli* coliforms produce red colonies. Colonies were manually counted after incubation at 37°C for ~18 h, at which time the colonies were visible

macroscopically. Control samples were taken periodically (every 30–40 min) throughout the study.

2.2.4. Statistical Analysis

Where appropriate, regression lines were fitted to the data sets. In the two-group comparisons, the homoscedasticity of the groups was first evaluated using the Fisher-Snedecor test (F-test). Except where noted, the groups were homoscedastic, and the p values were calculated using Student's t-test. One group was heteroscedastic (noted in the figure caption). For that case, the p value was calculated using Welch's t-test. p values < 0.05 were considered to indicate significance.

2.2.5. Ultrasound Imaging and Passive Cavitation Detection

Plane wave B-mode imaging at the frequency of 3.5 MHz was used prior to all exposures to confirm the repeatable positioning of the sample vials. During both CH and BH treatments, the emission of each histotripsy pulse was followed by the acquisition of 1 (for CH) or 31 (for BH) plane wave B-mode images every 20 ms. In addition, emission of CH pulses was synchronized with a 200 μs passive radiofrequency (RF) data capture by the ultrasound probe. The data corresponding to backscattered histotripsy pulses and broadband noise emissions from bubble collapses were acquired at a 12 MHz sampling rate every 30 s (e.g., 20 acquisitions for a 10 min treatment).

The acquisitions were post-processed to quantify broadband noise emissions. Note that the processing was not successful for BH exposures because of high levels of clutter from the 10 ms pulse reflections and reverberations from air−liquid interfaces and rigid boundaries of the experimental assembly.

Broadband noise quantification was conducted as follows: each acquisition was filtered in the frequency domain by a combination of a bandpass 1000th-order Hamming filter within 1.5−4.7 MHz and a second-order IIR comb filter with a notch bandwidth of 400 kHz applied at the

fundamental frequency of 1 MHz and its harmonics [44]. The filtered signals were then analyzed in the time domain to determine whether a cavitation event occurred. The section of the signal arriving prior to the round-trip time of flight to the transducer focus was considered as background noise; the section corresponding to the arrival time from within the sample vial was considered as the region of interest (ROI). Cavitation was considered present if the peak signal value within the ROI exceeded that of the background noise by a factor $\sqrt{5}$, corresponding to the Rose criterion, which ensures that the signal is distinguishable from the background noise.

For each sample, cavitation persistence was defined as the percentage of the CH pulses that induced a cavitation event among all recorded pulses for the sample. If a cavitation event was identified, broadband noise amplitude was calculated as the root-mean-square (RMS) value of the filtered passive cavitation detection (PCD) signal within the ROI. The mean and standard deviation of cavitation persistence and broadband noise amplitude, integrated over all the exposures, were calculated over the replicate samples corresponding to the same CH pressure level.

2.3. RESULTS

2.3.1. Inactivation Threshold

Initial studies were performed to determine the relative rate of bacteria inactivation as a function of focal pressure amplitude. Ten-minute exposures were performed at different pressures up to $p^- = 23$ MPa. CH exposures (Figure 2.3a) resulted in a clear threshold phenomenon: no reduction in bacterial load was observed until p^- exceeded a threshold value that itself depended on the pulse parameters. The reduction in bacterial load increased exponentially above the threshold. The slope of the line (rate of inactivation) was higher for the longer pulse (higher duty cycle). For BH exposures (Figure 2.3b), no threshold was observed. Instead, the reduction in bacterial load followed an exponential curve as a function of peak negative pressure. On comparison of CH (5-

cycle pulses) with BH, the open black circles indicate where the two trendlines cross. That is, at that specific pressure (17.8 MPa), the log reduction for both CH and BH was the same (0.9).

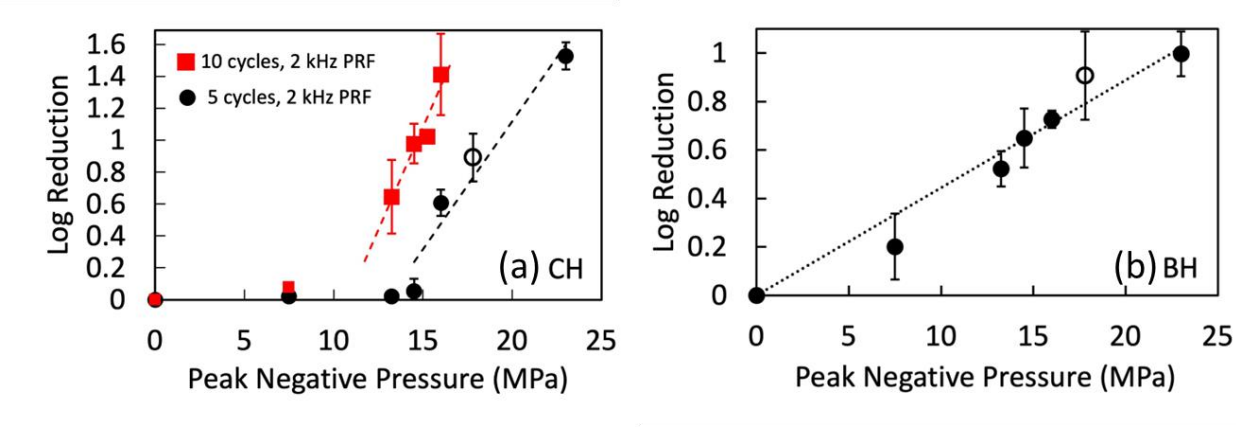

Figure 2.3. Mean log reduction (± standard deviation) in bacterial load with increasing peak negative pressure amplitude. (a) The CH threshold for inactivating *Escherichia coli* depended on pulse parameters. 5-cycle pulses at 2 kHz (1% duty cycle) had a higher threshold than 10-cycle pulses (2% duty cycle). Above the threshold, the bacterial log reduction increased linearly with amplitude (R^2 = 0.93 for both curves). (b) With BH (10,000 cycles at 1 Hz PRF), there was no measured threshold. However, the log reduction in bacteria also increased linearly with amplitude (R^2 = 0.90). The open circles in each figure have the same log reduction over 10 min (0.9) at the same pressure amplitude (17.8 MPa). BH: boiling histotripsy; CH: shock-scattering histotripsy; PRF: pulse repetition frequency.

2.3.2. Cavitation Detection

During CH, a hyperechoic cavitation cloud confined to the focal area could be seen in B-mode images (Figure 2.4), appearing intermittently from p^- = 14.5 MPa and without interruption from p^- = 16 MPa (at 1% duty cycle). The appearance of the cavitation cloud also correlated with distinct audible cavitation noise at the pitch of 2 kHz corresponding to the PRF. As the output level increased, the cavitation cloud shifted pre-focally and slightly elongated.

Conversely, during BH, the hyperechoic bubbles were seen to appear and circulate within the vial starting from p^- as low as 1 MPa. BH bubbles filled the entire sample volume after one to several pulses, starting from the pre-focal and focal areas and then spreading post-focally and sideways, consistent with a vortex-like streaming pattern induced by high-intensity ultrasound

(HIFU) radiation forces. A HIFU reverberation artifact was observed in the B-mode frames immediately following each BH pulse and highlights the difficulties encountered with the interpretation of PCD signals for BH exposures. Broadband noise processing of the PCD data for CH associated with Figure 2.3a was performed to evaluate cavitation analysis techniques that could be used *in vivo* for correlation with bacteria inactivation.

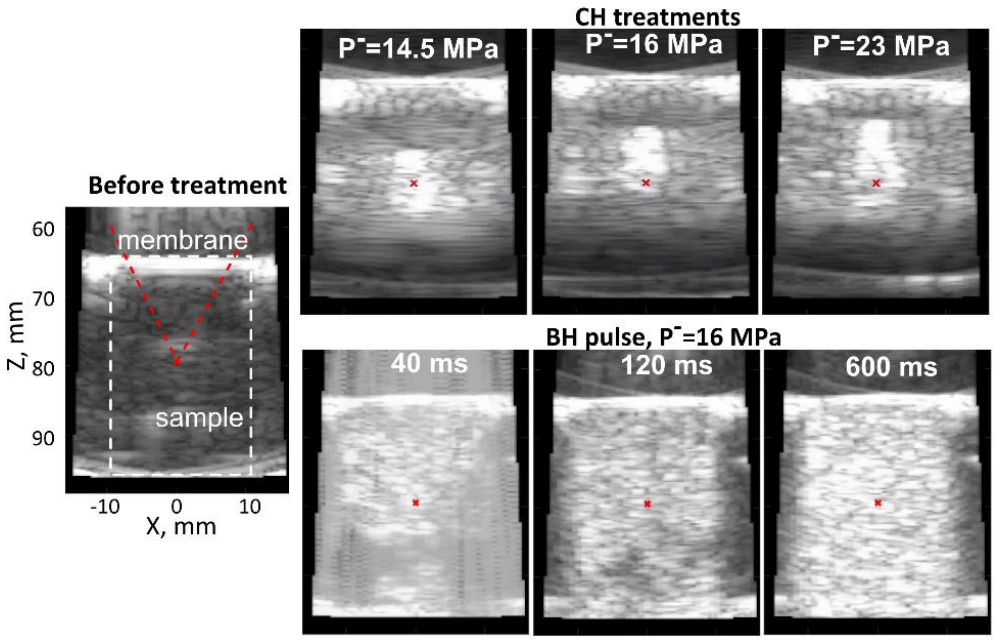

Figure 2.4. Representative B-mode ultrasound images observed during CH (top) and BH (bottom). The hyperechoic CH cavitation cloud was generally confined to the focal area; it slightly elongated and shifted pre-focally with the increase in p^- from 14.5 to 23 MPa. Conversely, following each BH pulse, hyperechoic bubbles filled the entire sample volume through visible streaming-induced mixing and persisted until the next pulse arrived. Note the high-intensity focused ultrasound reverberation artifact in the image immediately following the BH pulse (40 ms). BH: boiling histotripsy; CH: cavitation histotripsy.

As illustrated in Figure 2.5, the threshold between intermittent and continuous cavitation was evident in the output of passive cavitation detection. The analysis (Figure 2.5) revealed a step from low to high at the pressure levels corresponding to the transition between occasional and consistent generation of the cavitation cloud.

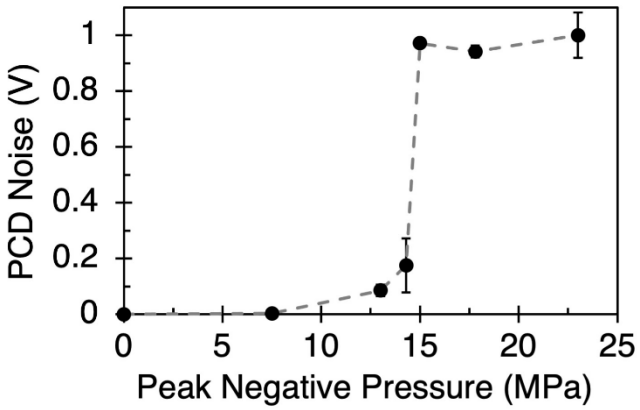

Figure 2.5. Passive cavitation detection metrics obtained from the 5-cycle cavitation histotripsy exposures in Figure 2.3a. Average amplitude of broadband noise emissions over the 10 min exposure. Both metrics exhibit a threshold-like behavior at the focal pressure of 16 MPa, which also corresponds to the threshold for inactivating *Escherichia coli* and indicates the onset of consistent cavitation. The error bars represent standard deviations. Trendlines are used to aid the eye. PCD: passive cavitation detection.

2.3.3. CH versus BH Treatment Time Studies

At a pressure of 17.8 MPa and a 1% duty cycle, both CH and BH result in similar log reductions (Figure 2.3, open circle data points). It was hypothesized that this equivalence should extend to other treatment times at this specific pressure level. Thus, comparative studies were performed at 17.8 MPa for up to 40 min to test this hypothesis. Both CH and BH have linear fits in the log linear plot (Figure 2.6). The difference between the slopes of regressions lines corresponding to CH and BH is statistically insignificant. Note that the abscissa in Figure 2.6 is given in terms of total treatment time, which is clinically relevant. For comparative purposes, treatment times can also be described in terms of "on-time" or number of pulses. Table 2.1 lists the numbers of pulses corresponding to the labeled treatment times for Figure 2.6.

Table 2.1. Number of pulses corresponding to treatment time for Figure 2.6.

Figure	Histotripsy	PRF (Hz)	Treatment Time (min)	No. of Pulses
6 Black	BH	1	5	300
6 Black	BH	1	10	600
6 Black	BH	1	20	1200
6 Black	BH	1	40	2400
6 Red	CH	2000	5	600,000
6 Red	CH	2000	10	1,200,000
6 Red	CH	2000	20	2,400,000
6 Red	CH	2000	40	4,800,000

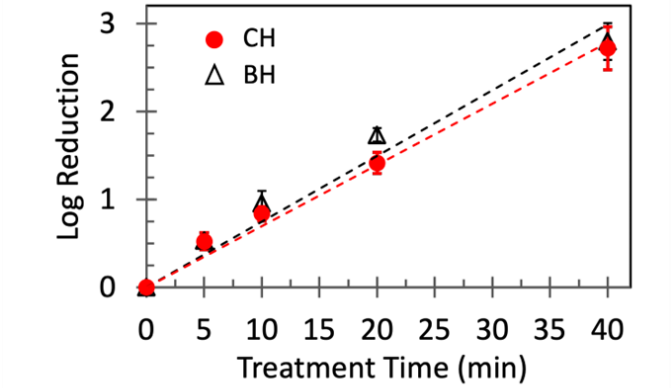

Figure 2.6. Comparison between CH (5-cycle pulses, 2000 Hz PRF, red circles) and BH (10,000-cycle pulses, 1 Hz PRF, open triangles) bacterial load reduction at a pressure of 17.8 MPa and 1% duty cycle. R^2 = 0.99 (CH) and 0.97 (BH). See Table 2.1 for converting treatment time to pulse number. BH: boiling histotripsy; CH: cavitation histotripsy; PRF: pulse repetition frequency.

2.3.4. Treatment Time Comparison at Different Peak Negative Pressures

In addition to comparing CH against BH at one pressure level, factors affecting each treatment modality were individually considered. Time-course studies were performed for both CH and BH at different pressure amplitudes, for up to 40 min (Figure 2.7). Bacterial load reductions are plotted in a log-linear format. Figure 2.7a illustrates CH treatments performed at two different peak negative pressure amplitudes: p^- = 23 and 17.8 MPa. Treatments at 23 MPa caused an increase in log reduction over 17.8 MPa treatments. A similar study with BH (Figure 2.7b) also yielded increased inactivation with higher applied pressures. In all cases, the number of inactivated bacteria increased exponentially over time (corresponding to straight lines in these log-linear

plots). All best-fit trendlines have a coefficient of determination (R^2) between 0.95 and 0.99. Note the data points at 10 min in Figure 2.7a were in close agreement with those at corresponding pressures in Figure 2.3. As with the previous figure, Table 2.2 lists the number of pulses corresponding to the treatment time in Figure 2.7.

Table 2.2. Number of pulses corresponding to treatment time for Figure 2.7.

Figure	Histotripsy	PRF (Hz)	Treatment Time (min)	No. of Pulses
7a	CH	2000	5	600,000
7a	CH	2000	10	1,200,000
7a	CH	2000	20	2,400,000
7a	CH	2000	40	4,800,000
7b	BH	1	5	300
7b	BH	1	10	600
7b	BH	1	20	1200
7b	BH	1	40	2400

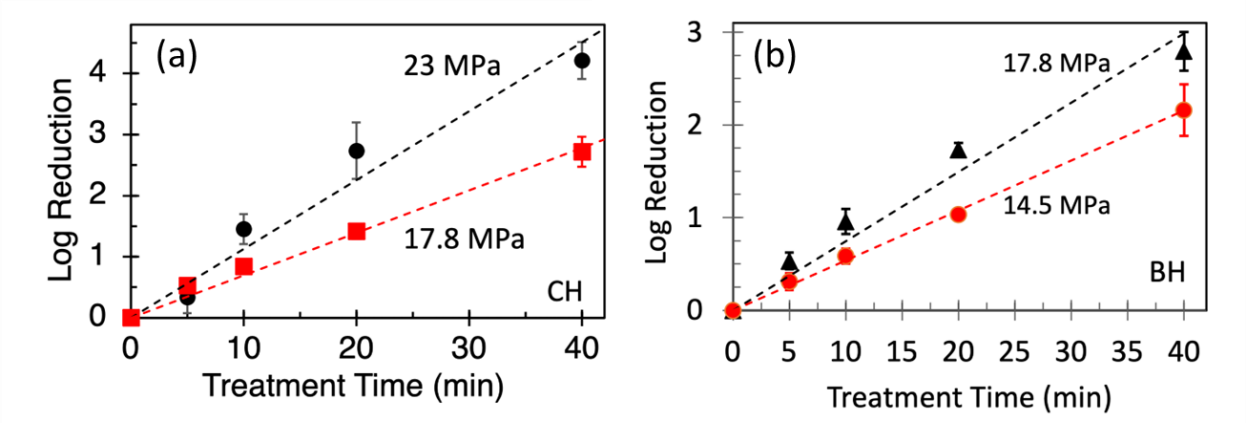

Figure 2.7. Mean log reduction (± standard deviation) in bacterial load over time at different peak negative pressures. Dashed lines represent best-fit linear trendlines. (a) CH treatments used 5-cycle bursts at 2000 Hz PRF. R^2 values for 23 and 17.8 MPa = 0.95 and 0.99, respectively. This group was heteroscedastic. The slopes of the trendlines for 23 and 17.8 MPa = 0.11 and 0.07, respectively. (b) BH treatments used 10,000-cycle bursts at 1 Hz PRF. R^2 values for 17.8 and 14.5 MPa = 0.98 and 0.99, respectively. The slopes of the trendlines for 17.8 and 14.5 MPa = 0.075 and 0.054, respectively. See Table 2.2 for converting treatment time to pulse number.

2.3.5. CH Parameter Comparisons

Finally, studies were performed to quantify bacterial load reduction for two different sets of CH pulse parameters. Our hypothesis is that bacterial load reduction depends on the total number of

pulses (or on-time). Thus, different sets of pulse parameters should produce the same outcome for the same duty cycle. In the following dose response study, CH treatments were performed at 16 MPa peak negative pressure with either 5-cycle pulses at 2000 Hz PRF or 10-cycle pulses at 1000 Hz PRF. The on-time is thus the same for both parameter sets. Figure 2.8 reveals that both sets of parameters led to the same log reduction at each time point. The difference between the slopes of regression lines corresponding to 5 and 10 cycles is statistically insignificant. Table 2.3 lists the numbers of pulses corresponding to the treatment times in Figure 2.8.

Table 2.3. Number of pulses corresponding to treatment time for Figure 2.8.

Figure	PRF (Hz)	Treatment Time (min)	No. of Pulses
8 Black	1000	5	300,000
8 Black	1000	10	600,000
8 Black	1000	20	1,200,000
8 Red	2000	5	600,000
8 Red	2000	10	1,200,000
8 Red	2000	20	2,400,000

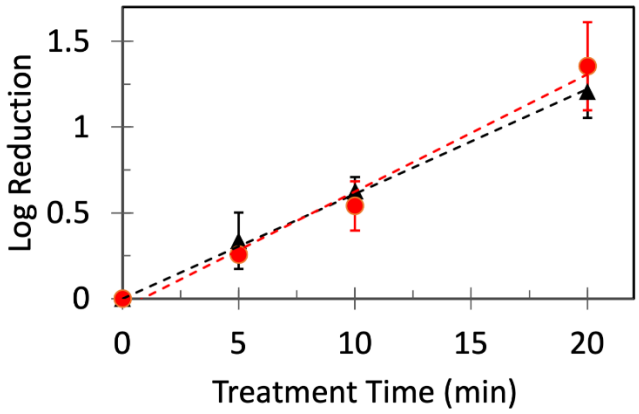

Figure 2.8. Mean log reduction (± standard deviation) in bacterial load over time. Dashed lines represent best-fit linear trendlines. CH pulse parameters: black triangles, 10 cycles at 1000 Hz PRF; red circles, 5 cycles at 2000 Hz PRF. p^- = 16 MPa for both. R^2 values for 5 and 10 cycles = 0.93 and 0.96, respectively. See Table 2.3 for converting treatment time to pulse number.

2.3.6. Statistical Analyses

Student's t-test was used in the case of equal variances between two regression models. Results

were statistically significant for Figure 2.7b ($p = 7.1*10^{-4}$) and statistically insignificant for Figures 2.6 and 2.8 ($p = 0.52$ and $p = 0.17$, respectively). In the case of unequal variances (Figure 2.7a), Welch's t-test was applied, and the results were statistically insignificant. This is likely due to the small number of replicates for the case of unequal variances.

2.4. DISCUSSIONS

Histotripsy includes multiple regimens, two of which are CH and BH. CH generates small lesions in rapid succession (~1 kHz), whereas BH generates a much larger lesion, but at a much lower rate (~1 Hz). The current work was initially motivated by the results of a prior uncontrolled *in vivo* study, suggesting greater variability in bacterial load reduction with BH treatments than with shock-scattering CH treatments [22]. Possible causes of variability in that study included unequal treatment durations and volumes. Here, a more controlled *in vitro* study determined that both CH and BH treatments reduce bacterial loads effectively for a 10 mL bacteria suspension. The studies evaluated the effects of peak negative pressure (from 14.5 to 23 MPa), treatment time (10, 20 or 40 min) and pulse parameters (BH: 10,000 cycles at 1 Hz PRF; CH: 5 or 10 cycles, at 2000 or 1000 Hz PRF, respectively). The duty cycles for these parameters were 1% for both BH and CH, except for the threshold data in Figure 2.3a that included a 2% duty cycle study. The pressure amplitude studies revealed that CH had a threshold for bacteria inactivation that depended on the pulse parameters, while BH did not exhibit any threshold behavior. For both modalities the rate of inactivation increased with pressure amplitude and treatment time.

The inactivation threshold observed for CH provides insight into the mechanism of histotripsy treatment. The CH threshold behavior was consistent with previous observations [39]. Figure 2.3a illustrates that the threshold is reduced with an increase in the duty cycle. The observed threshold level coincided with the pulse parameters that produced cavitation for each pulse. Below the

threshold, cavitation was inconsistent, and thus, the non-cavitating pulses did not contribute to bacteria inactivation. In addition, non-cavitating pulses do not contribute to sample mixing. Thus, below the continuous cavitation threshold, cavitation is intermittent and bacterial load reduction is more variable. On the basis of these results, a possible explanation for the absence of a threshold with BH treatments is that cavitation was generated by every pulse at all pressure amplitudes investigated.

Cavitation histotripsy-induced cavitation activity was quantified through PCD signal analysis to help identify a cavitation metric for bacterial inactivation in future *in vivo* studies. Because of reverberations of the long BH pulse from the walls of the small sample vial, the analysis was only successful for CH pulses. Specifically, the average amplitude of the broadband noise emissions was measured at a range of pressure levels corresponding to varying levels of inactivation for 10 min exposures. Broadband noise is commonly used as a measure of the intensity of inertial bubble collapses that are responsible for the observed bio-effect – inactivation in the present case. At lower treatment pressures (<16 MPa), cavitation was intermittent: broadband noise emissions were not detectable with every CH pulse, and the detectable emissions had low amplitude. At 16 MPa, the cavitation persistence reached 100% in a threshold-like manner: broadband emissions were detected following each pulse and their amplitude abruptly increased. This pressure threshold of consistent and violent cavitation corresponded to the threshold in bacterial inactivation.

At pressure levels above the threshold, broadband emission amplitude nearly plateaued (Figure 2.5). In contrast, the inactivation rate increased tenfold within the range 16–23 MPa (Figure 2.3a, black data points). It is speculated that the plateau is due to shielding of the cavitation cloud by its proximal front, which is shifted toward the transducer with the increase in pressure levels (Figure 2.4). This shielding may prevent emissions and scattering from the bubbles in the

central and distal parts of the cloud to reach the PCD transducer, thus reducing broadband emissions amplitude.

The treatment-time studies (Figures 2.6–2.8) highlight the noteworthy observation that both CH (above the threshold) and BH treatments resulted in an exponential bacterial load reduction over time, as evidenced by the linear fits to the log-linear plots. The inactivation rates, indicated by the slopes of the trendlines, were dependent on pressure amplitude for both CH and BH: higher pressure amplitudes led to higher inactivation rates (Figure 2.7).

In most cases, CH and BH did not exhibit equal effectiveness in bacterial inactivation. Below $p^- = 17.8$ MPa, BH exhibited greater bacterial inactivation rates. This was partially due to CH having a threshold below which significant inactivation did not occur, whereas BH did not exhibit such a threshold. At 17.8 MPa, CH and BH performed equally well at all time points examined (see, e.g., open circles in Figures 2.3 and 2.5). Above 17.8 MPa, CH outperformed BH in terms of bacterial inactivation. Figure 2.3 illustrates that over a 10 min period, the maximum inactivation rate for CH was a 1.5 log reduction in bacterial count, while over the same duration, the maximum BH treatment resulted in a 1 log reduction. Thus, in practice, the preferred treatment method may depend on the peak negative focal pressure attainable at the specific location of the targeted abscess within attenuative tissue and the available acoustic window.

These findings suggest that both CH and BH treated the entire 10 mL sample volume, as evidenced by the log-linear trends at all time points (bacteria inactivation is obeying a first-order exponential kinetic process; partial treatment should not lead to linear trendlines). This is somewhat counter-intuitive because BH created a larger cavitation cloud that filled a greater portion of the sample volume, thus resulting in a larger "treatment zone" each pulse. The cost for covering a larger volume was at a much reduced PRF (1 Hz), whereas CH treatments covered a

smaller volume, but at a much greater PRF (~1 kHz). In both regimens, circulation induced by streaming through the focal region ensured treatment of the entire 10 mL volume.

Although levels of disinfection up to 4.2 log reduction were reported, this occurred for a treatment time of 40 min. Faster treatments may be possible with higher average power (increased PRF) or peak power (increased input voltage). For the current studies, higher peak powers were impractical because of hardware limitations. Higher average powers would increase the duty cycle above 1%, which would enhance heating. Also, Tables 2.1–2.3 provide actual pulse numbers used in these studies and can be compared with other studies that use pulse number as a histotripsy parameter.

Finally, note that the gas concentration and sample temperature were not controlled. However, changes in gas concentration and temperature of the water bath surrounding the sample vial were monitored throughout. Over the course of a 40-min study, the gas concentration was observed to gradually increase by approximately 20% and the temperature increased from 20°C to 40°C. A study was performed to determine whether there was a difference in inactivation rate between the initial and final gas concentrations and between the initial and final temperatures. There were no statistically significant differences in bacterial load reduction in either case (data not shown). Nor were there changes in the rate of inactivation. Hence, changes in gas concentration or temperature of the coupling water did not affect the experiment.

2.5. CONCLUSIONS

Shock-scattering histotripsy and boiling histotripsy reduced bacterial loads in suspension in a consistent manner. In both cases, inactivation increased exponentially with pressure amplitude or treatment time. CH studies revealed an inactivation threshold phenomenon as a function of focal pressure amplitude related to the onset of consistent cavitation. In contrast, cavitation activity and

inactivation both increased gradually with pressure for BH studies. At or below the CH threshold, BH generated greater inactivation compared with CH; conversely, at pressure amplitudes substantially exceeding the threshold, CH generated a higher level of inactivation. In particular, at the highest pressure amplitude of 23 MPa and longest treatment time of 40 min, CH generated the largest bactericidal effect of 4.2 log compared with 2.8 log for BH under the same conditions.

Chapter 3. HISTOTRIPSY-INDUCED BACTERICIDAL ACTIVITY CORRELATES TO SIZE OF CAVITATION CLOUD IN VITRO

3.1. INTRODUCTION

In the last chapter, the similarities and differences in the two regimens of histotripsy were observed. Above a specific pressure, CH was more effective in inactivating *E. coli* than BH. Hence, CH is explored in the following chapters. The inactivation of *E. coli* by CH follows pseudo-first-order kinetics. Similar pseudo-first-order kinetics were also recently reported for *Pseudomonas aeruginosa* in suspension [41]. However, the pseudo-rate constants are sensitive to the acoustic variables, changing by up to a factor of 6 in some cases [45]. It thus becomes a formidable clinical challenge to predict the degree of treatment based on a specific set of parameters. Moreover, the impracticality of sample removal for characterization or treatment monitoring further compounds the clinical challenge of prognosticating outcomes based on a specific parameter set. The barrier for clinical implementation would be lowered if a simplifying predictive model for bactericidal rates were established.

Toward that end, the bubbles within cavitation clouds are responsible for soft tissue liquefaction, and the characteristics of a histotripsy cavitation cloud-its overall size, density, spatial distribution, and collapse time-are directly dependent on the acoustic exposure parameters [9], [46], [47], [48]. Importantly, for soft tissues, the size of the liquefied region is closely correlated with the dimensions of the histotripsy cloud [47], [49]. This observation leads us to hypothesize that for a given histotripsy target within a viscous liquid abscess, the effective treatment volume

will correspond to the size of the cavitation cloud.

An important distinction between soft tissues and abscesses is that abscesses are viscous liquids, not soft solids. Moreover, the current studies focus on bacterial suspensions, a low viscosity liquid. Therefore, a potential confounder is streaming associated with liquids that otherwise wouldn't occur in soft tissue. Nevertheless, it is hypothesized that the volume of bacteria eradicated within a single target region will approximate the size of the cavitation cloud.

A common way to characterize the cloud size *in vitro* is high–speed optical imaging [46]. It is with this technique that the potential for a single correlative factor-the cavitation cloud size is investigated to predict bactericidal activity over a range of acoustic parameters, including frequency, pressure amplitude, and pulse length. This is a continuation of work using the shock-scattering regime of histotripsy.

3.2. METHODS

The process of culture, preparation, and viability assessment of *E. coli* is described in detail in chapter 2.

3.2.1. Histotripsy Exposure Apparatus

This study utilized two histotripsy transducers operated across three frequencies (0.81, 1.20, and 3.25 MHz). One transducer (H-161, Sonic Concepts, Bothell, WA, USA) was electrically matched and operated at either 0.81 or 1.20 MHz. At the 0.81 MHz frequency, the transducer was driven by a function generator (33250A, Agilent, Santa Clara, CA, USA) and amplifier (AG 1012, T&C Power Conversion, Inc., Rochester, NY, USA), while at 1.2 MHz it was driven by a dedicated controller (TPO-401, Sonic Concepts, Bothell, WA, USA). A custom-made transducer fabricated in-house [50], operating at 3.25 MHz, was driven by the same function generator and amplifier. The transducer specifications and pulse parameters for these studies are listed in Table 3.4.

Two custom experimental apparatuses were used for the studies, as shown in Figure 3.1. At 0.81 or 1.20 MHz (Figure 3.1a), the H-161 transducer was mounted to the bottom of a cylindrical tube (15.2 cm diameter, 0.8 cm wall thickness, and 18 cm in height) filled with degassed water for coupling between the transducer and the sample vial. At 3.25 MHz, (Figure 3.1b) the transducer was positioned in a large, degassed water bath (not shown in the figure).

Table 3.4. Transducer specifications and pulse protocol for cavitation cloud imaging experiments.

Transducer	Sonic Concepts H-161	Sonic Concepts H-161	Custom
Frequency	0.81 MHz	1.20 MHz	3.25 MHz
Central opening diameter	47 mm	47 mm	None
Aperture	134.9 mm	134.9 mm	41 mm
Focal distance	124.5 mm	124.5 mm	45 mm
F-number	0.92	0.92	1.09
Pulse duration	24.6 µs	10 µs or 20 µs	20.3 µs
Pulse repetition frequency	406 Hz	1000 Hz or 500 Hz	492 Hz
Number of pulses	975,609	1,200,000	1,182,266
Acoustic power(s)	926 W	248 W to 1090 W	87 W
Camera exposure time	25 µs	13 µs or 25 µs	25 µs

For either apparatus, the sample vial contained 10 mL of bacteria culture (~10^8 cfu/mL). The bottom of each vial (2.5 cm outer diameter, 0.3 cm wall thickness, and 4.6 cm height) was replaced with an acoustically transparent polyethylene membrane held with an O-ring nested in an annulus machined into the bottom outer surface. The proximal wall of the membrane was wiped with a gauze sponge to eliminate pre-existing bubbles that could interfere with the ultrasound pulse. Alignment was verified by inducing cavitation within the vial and carefully positioning it so that cavitation was induced 15 mm above the bottom membrane.

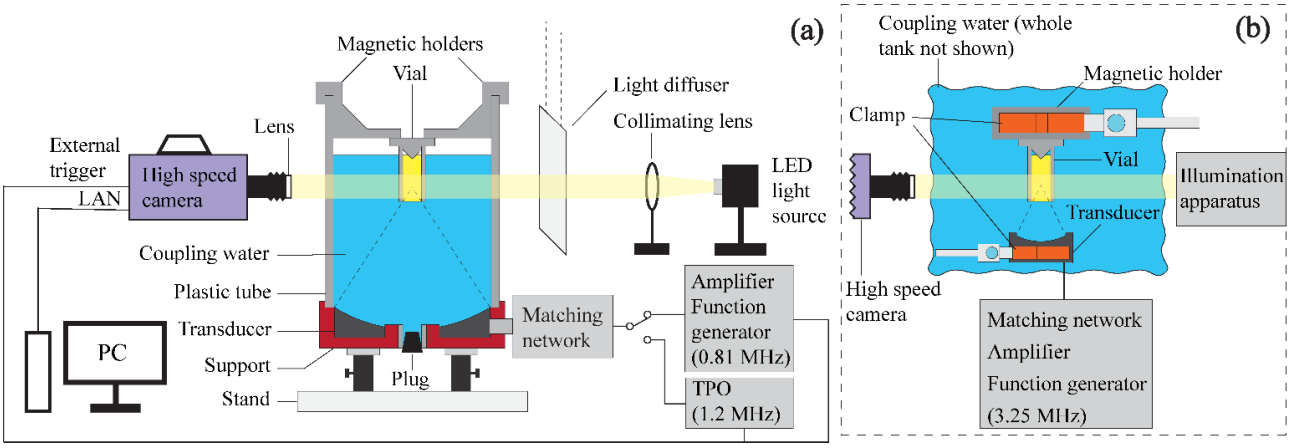

Figure 3.1. Experimental setups for cavitation cloud imaging at three different frequencies. (a) Studies at 0.81 and 1.2 MHz were conducted with a Sonic concepts transducer (model H-161) mounted to a cylindrical water bath degassed to <20% saturation. The sample vial was held with magnets that kept the vial aligned with the transducer. (b) Studies at 3.25 MHz were performed with a custom-built transducer immersed in a large degassed (<20%) water bath. Alignment of the transducer and sample vial were performed manually, as described in the text. For either setup, cavitation was generated at the focus, 15 mm above the vial's bottom, approximately at the center of the vial. The same LED light source back-illuminated the cavitation cloud. Additional details are described in the text.

In all studies, the system was operated above the consistent cavitation threshold in the sample vial. The position of the geometric focus was determined during the calibration procedure (see below). After finding the focus with the hydrophone, the distance from the hydrophone tip to the transducer was measured and used to register the focus position with the high-speed photography frame.

Calibration of the transducer focal pressure levels at the full range of driving voltages was performed in degassed water (<20% of saturation) with a fiber-optic probe hydrophone (FOPH 2000; RP Acoustics, Lautenbach, Germany; 100-μm active diameter, 100-MHz bandwidth). The sample vial was removed for characterization. Separate measurements showed the effect of the vial and membrane led to a reduction in peak positive (negative) pressure of approximately 4% (1%), respectively. At 3.25 MHz, hydrophone characterization could not be performed at the treatment settings due to the occurrence of cavitation at the fiber tip in degassed water.

To obtain focal pressure waveforms at those levels, axially symmetric nonlinear field simulations were performed using a freely available open-source high intensity focused ultrasound (HIFU)-beam software (https://limu.msu.ru/) based on solving the one-way propagation radially symmetric Westervelt equation [51]. The input voltage to the transducer was assumed to be proportional to the characteristic pressure at the transducer surface. The focal pressures from the simulations were matched to the experimentally calibrated points and extrapolated to higher voltages. Figure 3.2c shows the simulated waveform at 3.25 MHz. HIFU-beam simulations were also conducted at 0.81 and 1.20 MHz and the simulated waveforms were aligned with those observed experimentally, as illustrated in Figure 3.2a and (b). All waveforms in Figure 3.2 correspond to the output level at which the consistent cavitation threshold was achieved in bacterial suspensions. This corresponds to the lowest power levels used, as lowering levels further led to intermittent cavitation and a significant drop-off in bacterial reduction rates. Total acoustic power was noted at each simulation waveform corresponding to the experimental waveform at all

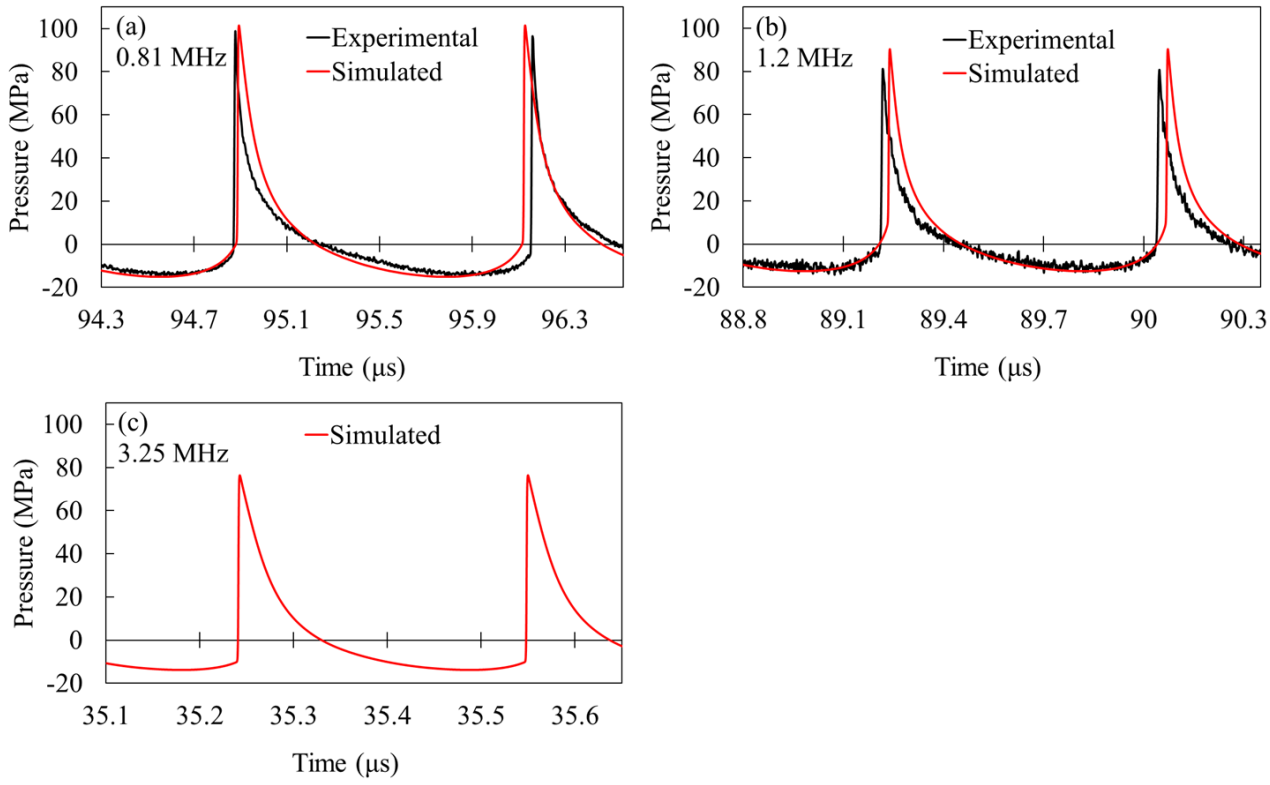

Figure 3.2. Focal pressure waveforms at the three frequencies were obtained from hydrophone measurements in degassed water (excluding the sample vial) and compared with numerical simulations. (a) Frequency = 0.81 MHz, acoustic power = 926 W. (b) Frequency = 1.20 MHz, acoustic power = 268 W. (c) Frequency = 3.25 MHz, acoustic power = 87 W. At 3.25 MHz, hydrophone measurements could not be performed due to the cavitation occurring at the hydrophone tip. These waveforms correspond to the lowest output acoustic power levels (just above the consistent cavitation threshold) at that frequency.

frequencies.

The consistent cavitation threshold was identified for each frequency in the bacterial suspensions. All experiments were conducted above these thresholds – a prerequisite for bacterial inactivation [45].

3.2.2. Cavitation Cloud Visualization Experiments

A high-speed camera (Photron Fastrax APS-RX, Photron, San Diego, CA, USA) was utilized to visualize cavitation clouds and quantify their characteristic size and shape. Because *E. coli* cultures used in the inactivation studies were too turbid for obtaining clear images of the cavitation clouds,

transparent growth medium (3% TSB) was used instead. For this reason, the cavitation cloud visualization experiments were conducted separately from the *E. coli* inactivation treatments. The growth medium was preheated in the incubator at 37°C for the same duration as the *E. coli* cultures to replicate their pretreatment conditions. As shown in Figure 3.1, the high-speed camera was focused on the transducer's focal region using an 80–200 mm zoom lens to capture grayscale images of the cavitation clouds at a resolution of 1024 × 1024 pixels. Proper lateral alignment was ensured by adjusting the camera until the diametrically opposite sides of the sample vial looked equally sharp. The vial was backlit by an LED and passed through a collimator lens and diffuser to provide uniform background light intensity. The camera shutter was triggered by the electronics driving the transducer, ensuring that an acquisition occurred at each histotripsy pulse. The acquisition was delayed by the time of flight from the transducer to the focus, and the frame rate corresponded to the PRF of the transducer. The shutter speed was set to be slightly longer than the pulse duration (Table 3.4) across all frequencies; thus each frame was a single grayscale image averaged over the entire pulse.

At each frequency, 1000 frames corresponding to 1000 pulses were recorded per acoustic power setting. The final image was thus an average of 1000 pulses. A few frames were recorded before starting the transducer and were later used for background noise subtraction. The pixel-to-mm ratio was determined in Image-J by taking the reference of known vial diameter and was 43–48 microns/pixel.

Figure 3.3a shows a representative grayscale image of a cavitation cloud. To calculate the area of the cloud, the image was processed in MATLAB (Natick, MA, USA) as follows. First, the background image noted above was subtracted from all frames. Cavitation clouds were identified using binary gray level thresholding segmentation, as a group of dark pixels (Figure 3.3b). The

exterior boundary of each cavitation cloud was traced using the Moore–Neighbor algorithm, and the cross-sectional area was determined by counting the number of black pixels within these boundaries. The pixel area was converted to square millimeters Figure 3.3c. The cavitation cloud area was averaged, and the standard deviation was calculated for all 1000 frames.

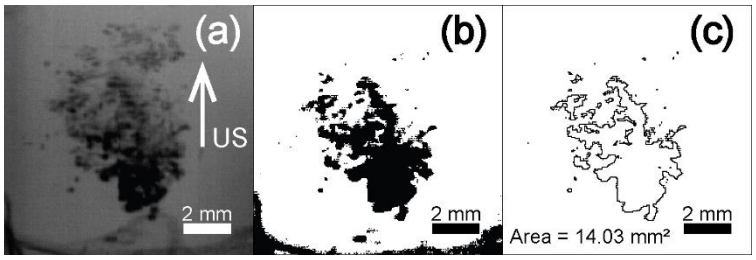

Figure 3.3. Image processing of grayscale images to obtain cavitation cloud area. (a) Representative grayscale image at 0.81 MHz, 24.6 µs pulse duration, 926 W acoustic power. The arrow is in the direction of the histotripsy pulse. (b) Conversion to binary image based on a binary threshold. (c) Outline of the cavitation clouds (black) in the binary images was highlighted and area was calculated based on the number of pixels. Note that the dark region at the bottom of (b), which corresponds to the vial membrane, is not included in the area calculation.

3.2.3. Exposure Protocol

The treatment parameters used with each apparatus are shown in Table 3.4. All treatments were performed for 40 min at 1% duty cycle making the total on-time 24 s for each treatment. Four pulse protocols were applied: 20.3-µs pulse duration (66 cycles) at 3.25 MHz; 10 or 20-µs pulse duration (12 or 24 cycles) at 1.20 MHz; and 24.6-µs pulse duration (20 cycles) at 0.81 MHz. At frequencies 0.81 and 3.25 MHz, only a single acoustic power setting was sufficient to exceed the consistent cavitation threshold, whereas for 1.20 MHz, multiple acoustic power settings exceeded the consistent cavitation threshold. Overall, inactivation experiments were conducted at seven distinct pulse protocols and each treatment was repeated four times. The seven protocols were selected to facilitate coverage of inactivation range between 0 and 4 log reduction, with cavitation cloud area values spread over this range.

Table 3.5. Treatment parameters for *E. coli* inactivation experiments.

Data point	Frequency (MHz)	Pulse (μs)	Cycles	Acoustic Power (W)	Cavitation cloud area (mm^2)
1	3.25	20.3	66	87	1.11
2	1.2	20	24	268	2.98
3	1.2	20	24	425	6.06
4	1.2	10	12	425	6.89
5	1.2	20	24	633	10.21
6	0.81	24.6	20	926	12.89
7	1.2	10	12	1090	16.71

3.2.4. Statistical Analysis

The relationship between *E. coli* log reduction and the cavitation cloud area was investigated using linear regression. The log reduction and optical imaging studies were performed separately. For each acoustic parameter set, the cloud size was determined by averaging the 1000 frames recorded in TSB. Separately, four replicate experiments determined the corresponding log reduction in bacteria. There is no way to associate a specific frame of cloud size with a specific treatment outcome. Hence, mean values were utilized for statistical analysis. The coefficient of determination and Pearson correlation coefficient of correlation were calculated in MATLAB.

3.3. RESULTS

3.3.1. Cavitation Cloud Images

Figure 3.4 shows representative cavitation cloud grayscale images at the three frequencies just above the consistent cavitation threshold; ultrasound is incident from the bottom of the images. In each image, a black region is visible pre-focally, corresponding to a dense cavitation cloud, which transitions to lighter shades of gray post-focally, indicating smaller and/or sparser bubbles. As expected, cavitation cloud size decreases with an increase in frequency. The area of the cavitation clouds in the frames is 14.03, 3.54, and 1.53 mm^2 for 0.81, 1.20, and 3.25 MHz, respectively. In addition, the cavitation cloud is wider at 0.81 MHz, while at higher frequencies of 1.20 and 3.25

MHz, the clouds assume an increasingly narrower shape.

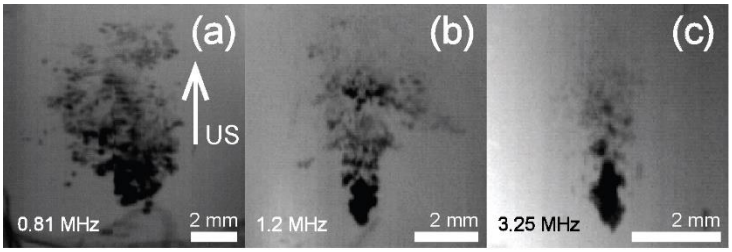

Figure 3.4. Cavitation cloud grayscale images in the growth medium (3% TSB) at the three frequencies just above the consistent cavitation threshold. The asterisk indicates geometric focus. (a) Frequency = 0.81 MHz, acoustic power = 926 W. (b) Frequency = 1.20 MHz, pulse duration 20 μs, acoustic power = 268 W. (c) Frequency = 3.25 MHz, acoustic power = 87 W. A decrease in dimensions with increasing frequency is observed.

Figure 3.5 illustrates representative cavitation clouds visualized at 1.20-MHz, 20-μs pulse length, at increasing acoustic powers ranging from 268 to 1090 W. The white star in each image indicates the geometric focus. With increasing acoustic power, an increase in the cavitation cloud length and width is observed. The proximal border of the cloud expands toward the transducer as the acoustic power increases, consistent with other reports [9]. At higher acoustic powers the bubbles in the post-focal regions were entrapped in vortical flow patterns (Figure 3.5d–i). Those flow patterns were previously reported for histotripsy clouds within confined spaces in the context of intravascular thrombolysis [52].

For all experiments, the exposure time was slightly longer than the pulse duration, which captures the cloud near its maximum size. That is, bubbles scatter more light when they are large and also spend more time near their maximum size. Thus, when averaged over the pulse duration, the images correspond to bubbles near their maximum size. The variation in intensity across the cloud is most probably due to differences in bubble density and maximum size. Lighter regions above the darker regions may represent residual bubbles from previous pulses entrained in the vortical streaming pattern. Binary thresholding focused on resolving the shape of the dark region of the cloud. Therefore, some bubble regions with grayscale values above the binary threshold,

particularly in the upper region of the cloud, were not included in the analysis. An example is seen in Figure 3.3a and (b).

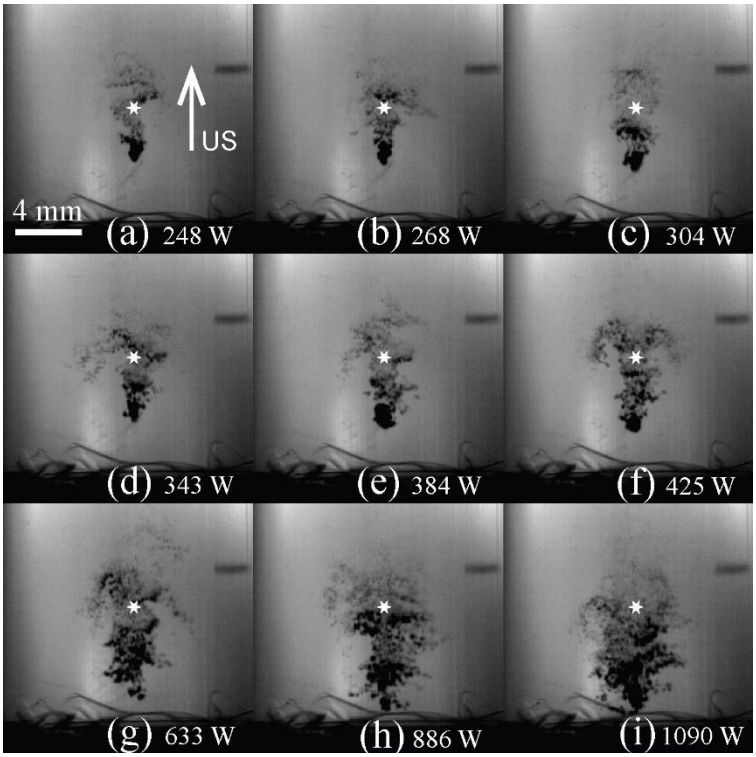

Figure 3.5. Cavitation cloud grayscale images in the growth medium (3% TSB) at 1.20 MHz, 20 μs with increasing acoustic powers from (a)–(i). Geometric focus is marked with an asterisk for reference. With increasing power, the cavitation cloud expands pre-focally.

3.3.2. Cavitation Cloud Area Dependence on Acoustic Power

Figure 3.6 shows the measured size of the cavitation cloud area (in mm^2) as a function of acoustic power at the different frequencies and pulse lengths; points marked with a star represent protocols used for both cavitation imaging and bacterial inactivation experiments. Error bars represent standard deviation of cavitation cloud area across histotripsy pulses. At 1.20 MHz, the cloud sizes for the two pulse lengths were similar within the measurement uncertainty. As mentioned previously, at frequencies 0.81 and 3.25 MHz, only a single acoustic power level was used.

Looking at Figure 3.6 and the area values from Table 3.5, the cavitation cloud area increases

linearly ($R^2 = 0.98$) with acoustic power over a range of frequencies and pulse lengths. That is, over the parameters that were studied, the cavitation cloud area dependence on the acoustic power is linear regardless of the other parameters. The variability in cavitation cloud size from pulse to pulse also increases with acoustic power, as evidenced by larger standard deviation bars.

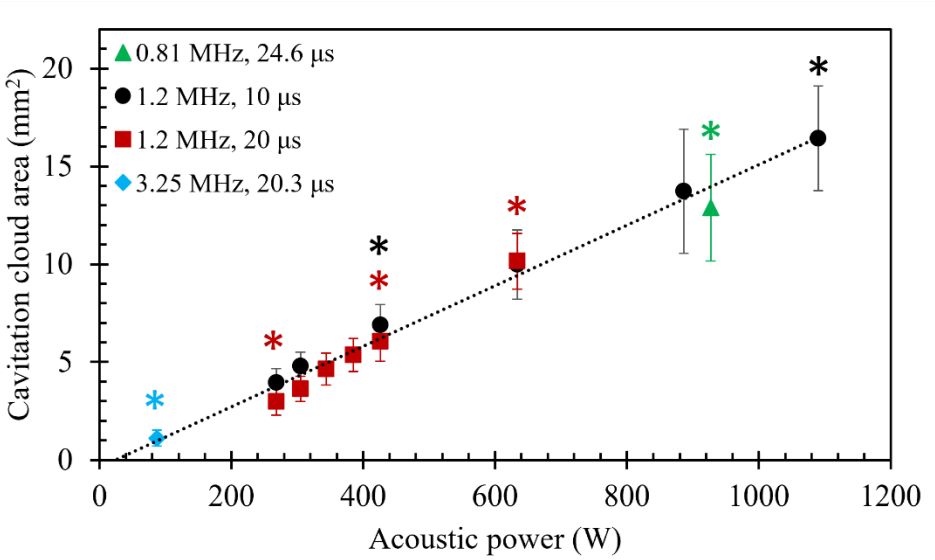

Figure 3.6. Cavitation cloud area dependence on peak acoustic power for the three frequencies and two pulse durations. Error bars correspond to standard deviation of the cavitation cloud area across histotripsy pulses. The increase in the cavitation cloud size is due to an increase in acoustic power and independent of the transducer frequency or pulse length. Points marked with a star indicate the protocols used for inactivation experiments.

3.3.3. E. coli Inactivation Dependence on Cloud Area

Inactivation treatments were conducted at seven distinct pulse protocols which are listed in Table 3.5 and also marked with stars in Figure 3.6. A strong linear relationship ($R^2 = 0.98$, $R = 0.99$, and $p < 0.0001$) between *E. coli* log inactivation and the cavitation cloud area was observed (Figure 3.7). The highest log reduction was 3.85 and was achieved at the frequency of 1.20 MHz, pulse duration of 10 µs and an acoustic power of 1090 W.

The plot displays these data as average and standard deviation for each treatment. The regression equation is $y = 0.23 \times x$. The slope of 0.23 suggests that each 4.3 mm^2 increase in

cavitation cloud area leads to an additional log reduction of 1.

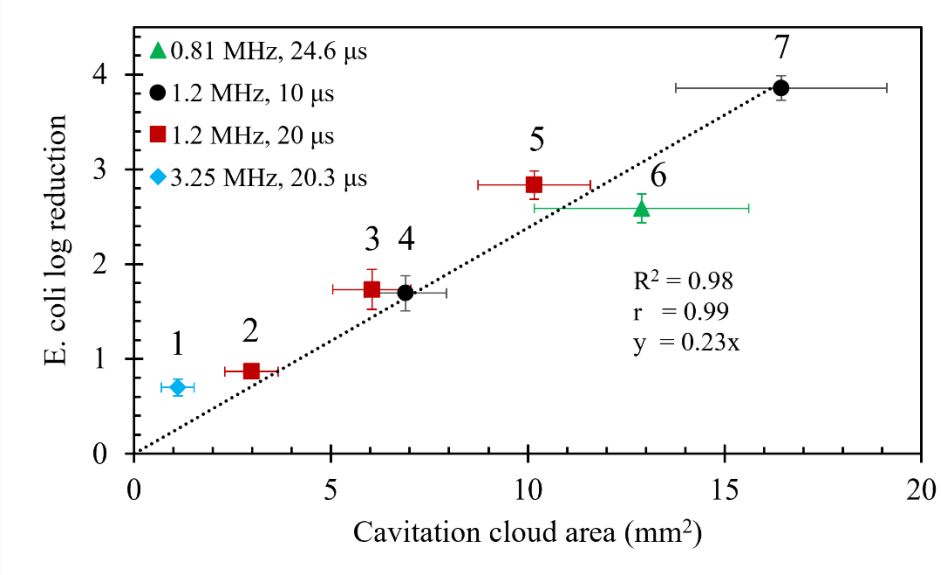

Figure 3.7. *E. coli* log reduction dependence on cavitation cloud area. Seven pulse protocols marked with a star in Figure. 3.6 and also listed in Table 3.5 were applied to 10-mL *E. coli* suspensions for 40 min. A strong linear dependence of log reduction on the cavitation cloud area was observed ($r = 0.99$, $p < 0.0001$, $n = 4$). Vertical error bars correspond to standard deviation of log reduction, while horizontal error bars correspond to the standard deviation of the cavitation cloud area from Figure 3.6.

3.4. DISCUSSIONS

The major findings of this study point to the cavitation cloud size as a single determinant for predicting *E. coli* inactivation because of the linear correlation between cloud area and inactivation (Figure 3.7). Seven disparate histotripsy pulse protocols consisting of three different frequencies, different pulse durations and a range of acoustic powers were used to create the cavitation clouds to induce *E. coli* inactivation. Yet across all those parameter combinations, the *E. coli* inactivation correlated well with the cavitation cloud area. This suggests that cavitation cloud area can be used as a predictive indicator of bacterial inactivation.

The opacity of *E. coli* in suspension precluded simultaneous measurements of the cloud dimensions and *E. coli* inactivation. Instead, separate experiments using identical parameters were performed, one to measure cavitation cloud dimensions in optically transparent TSB without

bacteria, and the other to evaluate *E. coli* inactivation in suspension. The cavitation cloud area was measured via high-speed photography under different pulse protocols with varying frequency, pulse duration, and acoustic power. Then a subset of those protocols was used to inactivate *E. coli* suspensions and evaluate the reduction in colonies.

In this chapter, peak acoustic power was chosen as the independent variable instead of peak negative pressure amplitude (p^-) commonly used in cavitation-based studies. This is due to the utilization of the shock-scattering histotripsy regime. In this regime, reflection, inversion, and scattering of the compressive shock from a single bubble lead to the formation of cavitation clouds. Peak positive pressure (p^+) and high-amplitude shock formation are thus requirements for the formation of cavitation clouds, and p^- alone does not fully describe the corresponding cloud size [9].

The parameter space was chosen to span a range of frequencies, powers, and pulse lengths. These are all known to have large influences on cloud size. Histotripsy frequencies are usually in the sub-to-low MHz range, hence frequencies within that range were chosen (0.8–3.25 MHz). The cloud size varied greatly from low to high frequency, as shown in Figure 3.4. Power is another important parameter that governs cloud size (see Figure 3.6). The lowest power level was just above the consistent cavitation threshold, while the upper values were limited by the driving electronics and practical considerations. Pulse lengths were selected based on standard histotripsy protocols for the shock-scattering regime. These parameters yielded a range of log reduction from 0 to 4.

One important finding in this chapter is that the cavitation cloud area depended linearly on the acoustic power for all frequencies and was independent of pulse length (Figure 3.6). The pulse length independence could be attributed to the relatively long 10 and 20 μs pulse durations. The

axial size of the cavitation cloud is known to grow with pulse duration, but saturate beyond a certain value, and the lateral size is independent of it [9].

For any set frequency, the linear dependence of the cavitation cloud area on acoustic power can be explained as follows. The shape and dimensions of the cavitation cloud are determined by those of the area within which the high-amplitude shocks are formed [51], [43]. At the output levels beyond shock formation regime, p^+ grows nearly linearly with pressure at the transducer surface p_0, and so do both lateral and axial dimensions of the area around the focus where shocks are formed. Because the area is proportional to the product of the two axial dimensions, and thus to p^2, it is, in turn, linearly proportional to acoustic power.

Interestingly, the cavitation cloud areas corresponding to consistent cavitation threshold at three different frequencies were close to the same linear relationship on acoustic power. This similarity can be explained as follows. The acoustic power that is necessary to achieve a certain focal pressure level in the linear regime has an inverse quadratic dependence on frequency for spherically-focused transducers [53]. In the nonlinear regime, the focal pressure levels p^+ and p^- at which the shocks form are known to be similar, regardless of the frequency, provided similar F-numbers of the transducers in our case 0.92 and 1.1. The dependence of acoustic power at which the shocks (and hence the cavitation clouds) form on frequency is also close to inverse quadratic [43]. Therefore, the acoustic power at which the shocks (and hence the cavitation clouds) form can be expected to also follow the inverse quadratic dependence on frequency. The axial and lateral dimensions of the cavitation cloud are determined by those of the transducer's focal area, which are both inversely proportional to the ultrasound frequency [53], thus its area is inversely proportional to the square thereof. Since both the acoustic power and the 2-D axial cross-sectional area of the cavitation cloud at the threshold of its formation depend on frequency in the same way

(inverse quadratic), it was reasonable to expect a close to linear proportionality between them for different frequencies. This expectation was experimentally confirmed Figure 3.6. However, it is important to note that this linear proportionality should not be expected to be universally applicable and is limited to the F-numbers and aperture-to-wavelength ratios considered here.

The effects of acoustic parameters on shock-scattering histotripsy cavitation clouds have been studied via high-speed photography in phantoms and water [9], [48]. In this work, the clouds were produced in a confined volume (10 mL) of TSB solution with dissolved gas concentration relevant to cultured bacterial suspensions. Higher gas concentrations affect cavitation bubble and cloud dynamics, and the confined volume (relevant to treating abscesses) affects the structure of vortical streaming patterns [52]. Furthermore, a range of acoustic parameters previously shown to result in clinically relevant inactivation [45], [22] and applicable to abscesses of variable sizes located at varying depths had to be considered. This necessitated the optical observation of the cavitation clouds performed here. Histotripsy cavitation activity in bacterial suspension was characterized via coaxial ultrasound B-mode imaging and passive cavitation detection (PCD) that quantified broadband noise emissions from inertially collapsing bubbles [45]. However, no predictive relationship between PCD-based metrics and log reduction was identified in those studies, which was hypothetically attributed to shielding of the emissions by the proximal layers of the bubbles in the cloud. In light of the high-speed photography observations of the cavitation clouds here (Figure 3.5) a different explanation appears more plausible: bacterial inactivation depends not only on the presence of inertial bubble collapses, but also on the number of those bubbles, i.e., the cavitation cloud dimensions, which cannot be captured by single-channel PCD, as it is not spatially resolved.

Different histotripsy regimes are likely to exhibit comparable outcomes, as they all rely on the

formation and collapse of a cavitation cloud at the focal area, resulting in the mechanical fractionation of cells. The primary distinction among these histotripsy techniques lies in the pulse duration and peak focal pressures [54]. This study utilized shock-scattering histotripsy, with pulse lengths ranging from 10 to 25 μs. In contrast, boiling histotripsy uses pulses of 1–10 ms in duration, producing substantially larger cavitation clouds due to the increased number of cycles. Similar to shock-scattering histotripsy, boiling histotripsy demonstrated comparable trends in bacterial reduction [45]. Conversely, intrinsic threshold histotripsy utilizes nearly monopolar rarefactional pulses shorter than 2 μs to generate smaller cavitation clouds. While this regime may also promote bactericidal activity, the limited cavitation cloud size renders it impractical for treating larger abscesses; however, it could be beneficial for managing smaller superficial abscesses caused by skin and soft tissue infections.

A limitation of this study is that optical imaging of the cavitation cloud size and inactivation studies had to be performed in separate experiments due to the high turbidity of bacterial suspensions. However, the cavitation thresholds in TSB and bacterial suspension (quantified for all frequencies) were similar, as was the gas content. Thus, the differences in the cavitation cloud size should not be significantly different with or without bacterial suspensions.

3.5. CONCLUSIONS

Shock-scattering histotripsy was used to treat a constrained volume of *E. coli* in suspension. Separately, the induced cavitation cloud was optically imaged in the same volume, without bacteria. Acoustic parameters included three different frequencies, as well as several pulse lengths and power levels. It was found that the size of the cavitation cloud depended linearly on the acoustic power level for all frequencies and was independent of the pulse length. Similarly, *E. coli* inactivation linearly correlated to the size of the cavitation cloud, despite diverse parameters.

Chapter 4. DEPENDENCE OF HISTOTRIPSY-INDUCED BACTERICIDAL ACTIVITY ON THE SAMPLE VOLUME IN VITRO

4.1. INTRODUCTION

Histotripsy has been successfully applied to inactivate bacteria in suspensions *in vitro* [45]. Over a diverse range of pulse parameters, histotripsy induced bactericidal activity correlated strongly with the cavitation cloud size [55]. However, using the cloud size alone as an inactivation predictor may become problematic in systems with varying sample volumes like abscesses. A cavitation cloud of the same size may produce lower inactivation in a larger sample volume because of lower probability of bacterial exposure to cavitation. Additionally, the sample streaming dynamics may get altered at higher volumes affecting bacterial mixing. Therefore, a metric that normalizes the cloud size by the total sample volume may account for volume variations and serve as a more consistent predictor of bacterial inactivation.

In this chapter, the metric – normalized cloud volume is introduced, which is the ratio of cavitation cloud volume to sample volume. Theoretically, the value of normalized cloud volume ranges from 0–1: 0 when the cloud is not present, and 1 when cloud volume is equal to the sample volume. Practically, this metric is defined only at and above the input acoustic power levels sufficient to create a cavitation cloud on every pulse i.e. consistent cavitation threshold [45]. This is because a significant bacterial kill is obtained only above the consistent cavitation threshold.

It is hypothesized that the *E. coli* inactivation (log reduction) will strongly correlate with normalized cloud volume, across a range of sample volumes and cavitation cloud sizes. Three sample volumes were used – 10 mL, 18 mL, 28 mL, and were contained by cylindrical sample vials of same height but increasing diameter to account for higher sample volumes. The sample

vials were axially aligned with a transducer with the entire focal volume within the sample. The three samples were treated with three cavitation cloud sizes, creating nine unique values of normalized cloud volume, and the *E. coli* log reduction was calculated at each value.

4.2. METHODS

The process of culture, preparation, and viability assessment of *E. coli* is described in detail in chapter 2.

4.2.1. Treatment Setup, Characterization, and Pulse Protocol

A single-element transducer (H-161, Sonic Concepts, Bothell, WA, USA), driven by a controller (TPO-401, Sonic Concepts, Bothell, WA, USA) was used for treatments. The transducer was attached using a 3-D printed fixture to a water bath (Figure 4.1) consisting of a cylindrical polycarbonate tube (15.2 cm diameter, 0.8 cm wall thickness, and 18 cm in height). The water bath contained degassed water at room temperature for coupling between transducer and sample vials. Three cylindrical sample vials of the same height (4.6 cm), same wall thickness (0.3 cm), and different inner diameters (1.9 cm, 2.5 cm, 3.1 cm) were used to contain three sample volumes (10 mL, 18 mL, 28 mL) respectively. The bottom of each vial was replaced with an acoustically transparent polyethylene membrane held with an O-ring nested in an annulus machined into the bottom outer surface. The proximal wall of the membrane was wiped with a gauze sponge to eliminate pre-existing bubbles that could interfere with the ultrasound pulse. The alignment was verified by inducing cavitation within the vial and carefully positioning it so that cavitation was induced 15 mm above the bottom membrane. Distance between cavitation and bottom membrane was measured from B-mode image.

The acoustic characterization data was used from chapter 3. The system was operated at 1.2 MHz center frequency, 20 μs pulse duration, and at 1% duty cycle for 40 minutes at three acoustic

powers of 268 W (consistent cavitation threshold), 425 W (1.58x threshold), 633 W (2.31x threshold).

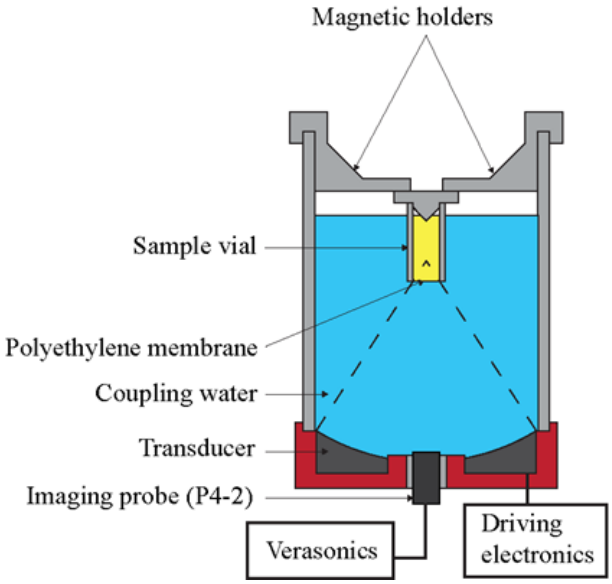

Figure 4.1. Illustration of the experimental setup. A 1.2 MHz transducer (Sonic concepts model H-161) was attached to the bottom of a degassed water bath. The apparatus was designed so that the transducer's focus was 15 mm upward from the bottom of sample vials containing 10 mL, 18 mL or 28 mL of *Escherichia coli* bacteria (~1×10^9 cells/mL). A thin acoustically transparent membrane was placed at the bottom of each vial for improved acoustic energy transmission. The vials were aligned to the transducer using two pairs of magnets to allow for fast reproducible alignment of replicate samples.

4.2.2. Cavitation Cloud Volume Estimation

A high-speed camera (Photron Fastrax APS-RX, Photron, San Diego, CA, USA) was utilized to visualize cavitation clouds and quantify their volume. The cavitation cloud image data used in this study was taken from chapter 3 which used the same system and pulse protocol. The resolution was 1024 x 1024 pixels and images were obtained in grayscale. The following processing steps were conducted to estimate cavitation cloud volume from each 2D grayscale image (Figure 4.2).

The first step was area (A) calculation. The image was converted to binary format based on a pre-determined normalized brightness threshold of 0.1 which was used for all images considered

in this analysis. In the binary images, the black region represented the cavitation cloud. The number of black pixels was counted and multiplied by the square of the mm-to-pixel ratio (0.04672 mm/pixel) to calculate cavitation cloud area in square millimeters.

The volume calculation process was conducted as follows. First, the cloud height (h) was obtained by using a MATLAB algorithm to locate pixels indicating the top and the bottom of the black region (representing the cloud) as shown in Figure 4.2b. To avoid erroneously considering stray bubbles in the analysis, the top pixel was defined as the first black pixel that has at least 15 consecutive black pixels below it when searched from the top. Similar logic was used to obtain the bottom pixel, and the cloud height was considered to be the difference between the two pixels row numbers. Since cavitation cloud is represented by a continuous black region, there is a high probability that the bottom most pixel and topmost pixels would have at least 15 black pixels above and below them respectively. The choice of 15 pixels was determined through trial and error by evaluating different values between 1 and 20. Based on visual inspection, 15 pixels most consistently identified the appropriate top and bottom points of the cloud. The volume was calculated by assuming that the cloud is an axially symmetric ellipsoid, with cross-sectional area A and the height h, using the formula mentioned in Figure 4.2c. The derivation of the formula is given in appendix A. At each treatment setting, the cavitation cloud volume value was averaged over 450 images.

4.2.3. Statistical Analysis

Treatments at each normalized cloud volume value were repeated five times, with replicates distributed across two separate days. A linear regression analysis was conducted between the normalized cloud volume values and corresponding mean *E. coli* log reduction values.

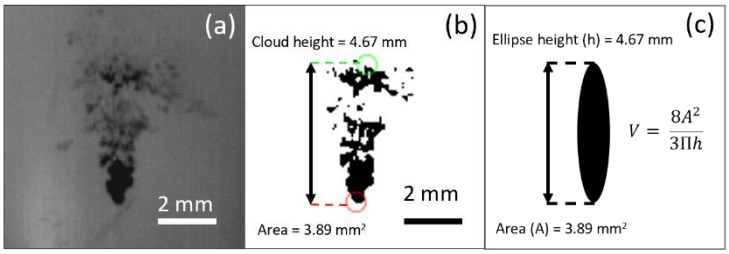

Figure 4.2. Cavitation cloud volume estimation. a) Representative grayscale frame, with the shadowgraph corresponding to the cavitation cloud. The pulse parameters were 1.2 MHz frequency, 20 µs pulse duration, 268 W acoustic power. b) Binary thresholding and calculation of height and area of the cavitation cloud. c) Cross-sectional view of an axially symmetric ellipsoid of equal height and cross-sectional area as the cavitation cloud. The derivation of the volume equation is given in appendix A.

4.3. RESULTS

4.3.1. Normalized Cloud Volume Values

Three cavitation cloud volumes were used to treat three sample volumes, generating nine unique values of normalized cloud volume, which are mentioned in Table 4.6. The data points are ordered by increasing normalized cloud volume values.

Table 4.6. Normalized cloud volume values (ratio of cavitation cloud volume to sample volume) considered for treatments. Three sample volumes – 10, 18 and 28 mL were each treated at three cavitation cloud volumes generating nine unique values. The cavitation cloud volume was calculated by the process shown in Figure 4.2. The data points are ordered by increasing normalized cloud volume values. The mean cloud volume for each acoustic power was calculated separately in bacterial growth medium as described in chapter 3.

Data point	Sample volume (mL)	Acoustic power (W)	Mean cloud volume (mm^3)	Normalized cloud volume
1	28	268	2.68	9.56E-05
2	18	268	2.68	1.49E-04
3	28	425	6.52	2.33E-04
4	10	268	2.68	2.68E-04
5	18	425	6.52	3.62E-04
6	28	633	16.13	5.76E-04
7	10	425	6.52	6.52E-04
8	18	633	16.13	8.96E-04
9	10	633	16.13	1.61E-03

4.3.2. Dependence of E. coli Log Reduction on Sample Volume

Figure 4.3 shows the variation of *E. coli* log reduction with sample volume at the three cavitation

cloud volumes. *E. coli* log reduction decreases with increasing sample volumes at a specific cavitation cloud volume. This dependence can be quantified closely with $R^2 = 0.89, 0.99, 0.97$ for 10 mL, 18 mL, and 28 mL respectively by using a power curve (Figure 4.3). The decrease is higher for higher cavitation cloud volumes as shown from increasing exponent amplitude of the power curve.

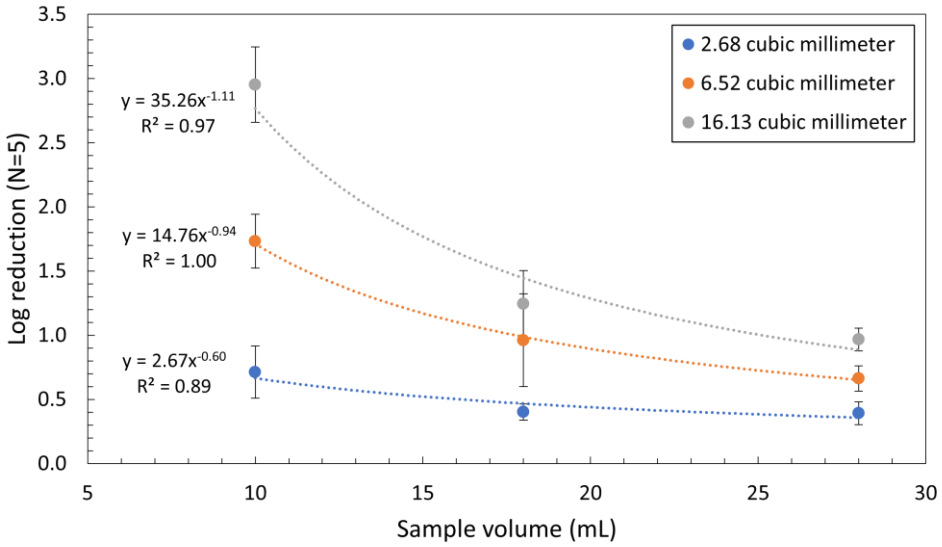

Figure 4.3. Effect of sample volume on *E. coli* inactivation (log reduction) at three cavitation cloud volumes at 1.2 MHz frequency, 20 µs pulse duration, 1% duty cycle, and 40 minutes treatment time. At each cavitation cloud volume, the data can be fitted with power trendlines with high coefficient of regressions ($R^2 = 0.89,1.00,0.97$).

4.3.3. Correlation of E. coli Log Reduction and Normalized Cloud Volume

Figure 4.4 shows the dependence of *E. coli* log reduction on normalized cloud value. A strong linear correlation was observed ($R^2 = 0.9$, $R = 0.94$) and the regression equation was $y = 1605.2x + 0.2508$.

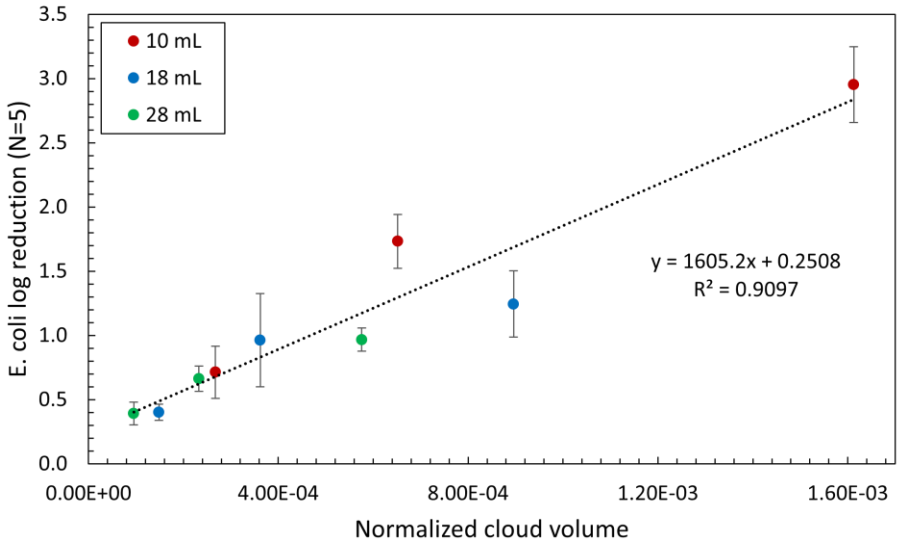

Figure 4.4. Correlation between *E. coli* inactivation (log reduction) and normalized cloud volume. The cavitation cloud volume and the sample volume for each data point can be found in Table 4.6.

4.4. DISCUSSIONS

This work aimed at establishing the metric normalized cloud volume to serve as a more consistent predictor of bacterial inactivation as compared to the cavitation cloud size. The hypothesis that normalized cloud volume will correlate strongly with *E. coli* log reduction was validated (R = 0.94), supporting the predictive capability of this metric.

At the same cavitation cloud volume, the inactivation decreased with increasing sample volume in a power dependence manner. This dependence has been observed previously for yeast with breakage decreasing from 90% at 1 mL to 20% at 19 mL when irradiated at 500 W for 2 minutes [24]. This also indicates that the log reduction will tend to zero for a much larger sample volume compared to the cavitation cloud size.

The main result of this chapter is that *E. coli* log reduction correlates strongly with normalized cloud volume. The regression equation is y = 1605.2x + 0.2508. Given a sample volume, the increase in cavitation cloud volume needed to increase the log kill by the desired value can be calculated. For example, for 10 mL sample volume, the cavitation cloud volume need to be

increased by 6.33 mm^3 to increase the log kill by 1 in 40 minutes at 1% duty cycle.

Along with normalized cloud volume, another variable to be considered for understanding the system is the sample streaming. It is caused by the acoustic radiation force and the Kelvin impulse from bubble collapses [52], [56], [57]. Macroscopically, vortical streaming patterns were observed in the sample. Increased streaming results in better mixing of the bacterial sample, leading to a more uniform energy distribution across all bacteria throughout the sample. For lower normalized cloud volume values, i.e. larger sample volumes compared to the cavitation cloud volume, streaming may not efficiently mix the sample leading to redundant collapses i.e. affecting already killed bacteria. Also, some bacteria may not be exposed to cavitation altogether. At higher normalized cloud volumes, where the cloud occupies a significant portion of the sample volume, higher streaming may occur leading to better mixing. As the cloud volume approaches the sample volume, all bacteria may get exposed to cavitation due to excellent mixing. Hence, it is expected that this curve may saturate as the normalized cloud volume approaches 1. It would be interesting to know the number of bubble collapses needed to inactivate a single *E. coli* bacterium, to optimize the treatment time.

The cavitation cloud volume estimation process in this study has several limitations. Firstly, the cloud was assumed to be an axially symmetric ellipsoid which is not true considering the stochastic nature of bubbles. Secondly, the binary threshold was selected manually based on visual similarity between the binarized black region and the dark region corresponding to cavitation clouds. Using automatic image thresholding techniques like Otsu's method would reduce potential bias in cloud segmentation. Thirdly, defining the cloud height is not straightforward, since considerable spatial variation is observed post-focally. This is indicated by high standard errors in cavitation cloud volume.

4.5. CONCLUSIONS

The dependence of *E. coli* inactivation with sample volume was well described by a power trendline, indicating a more rapid decay with increasing acoustic power. The ratio of histotripsy cavitation cloud volume and total bacterial sample volume (normalized cloud volume) was established as a predictor of *E. coli* inactivation in a system with variable sample volumes.

Chapter 5. COMPARISON OF HIGH-SPEED PHOTOGRAPHY AND CO-AXIAL PLANE WAVE B-MODE IMAGING IN MEASURING HISTOTRIPSY CAVITATION CLOUD SIZE

5.1. INTRODUCTION

High-speed photography (HSP) has been instrumental in advancing the understanding of cavitation dynamics through optical means. In the context of histotripsy, HSP has been used to visualize individual bubble-cell interactions [58] and elucidate the cavitation cloud formation mechanism [9]. However, it is not suitable for observing cavitation in tissues in the human body since they are not optically transparent. For example, a study with the long-range goal of histotripsy-induced abscess disinfection used HSP to visualize cavitation clouds and establish the cloud size as a predictor of bacterial inactivation rates *in vitro* [55]. However, clinical application of this concept is challenging since abscesses are optically opaque. Alternative imaging modalities need to be explored to overcome this challenge.

One such modality is B-mode ultrasound imaging, which shows cavitation clouds as hyperechoic regions in tissues. A conventional B-mode image consists of tens to hundreds of scan lines over the course of several milliseconds, but a cavitation cloud can undergo significant changes within that time. A modification of this modality is plane wave B-mode that transmits and receives with all elements in parallel, showing the image at one instant in time at the cost of lower contrast between bubbles and tissues, and lower spatial resolution.

Plane-wave B-mode imaging has been used to visualize histotripsy cavitation clouds, and quantify their size [59]. Some groups have used chirp-coded excitation and non-linear filtering techniques to enhance contrast to more accurately measure the cavitation cloud size [60]. However, in these studies a large-aperture imaging probe was positioned orthogonally and close to the therapy transducer axis to minimize imaging distance. This positioning is not clinically relevant

since in all practical configurations the imaging probe is fixed in-line with the therapy transducer as shown in Figure 4.1 (or refer Figure 2.1 for better representation).

To enable ultimate clinical implementation of cavitation cloud area measurement, it is essential to validate plane wave B-mode imaging against HSP in the same arrangement with an in-line imaging probe. This study aimed to evaluate the capability of plane wave B-mode imaging to detect changes in cavitation cloud dimensions with changes in acoustic power. This was achieved by comparing the cavitation cloud size (cross-sectional area) within the imaging plane of both HSP and B-mode at the same instant in time, for a series of system input powers. To the author's knowledge, this type of study is not found in literature, although comparisons of HSP with Passive Acoustic Mapping (PAM) have been conducted in the same setup [61], [62]. PAM provides spatiotemporal information, including cavitation cloud size, and enables spectral analysis for more detailed characterization, although at a high computational cost. However, our interest is limited to cavitation cloud size, which directly predicts bacterial inactivation [55]. Hence, the computationally inexpensive and clinically accessible plane-wave B-mode imaging was used in this study instead of PAM.

5.2. METHODS

5.2.1. Experimental Setup

A spherically focused transducer (PETAL SURGICAL, F# 0.75, aperture 92.64 mm, circular opening diameter 37.21 mm) was operated at a frequency of 1.25 MHz with 12 cycles at 1000 Hz Pulse Repetition Frequency (PRF) in a tank filled with deionized, degassed water (<20% O_2) (Figure 5.1). The transducer was driven by high-powered electronics system, as described here [42]. This transducer was selected due to its use in clinical studies, and its focal length (69.48 mm), which is shorter than that of the *in vitro* system used in previous chapters, resulted in improved B-

mode image quality. A 64-element phased array (3PC, HUMANSCAN) was inserted in the transducer central opening, and operated at 3 MHz. The imaging probe was attached to Verasonics (Kirkland, WA, USA) V1 ultrasound system and single wave plane wave B-mode imaging was employed.

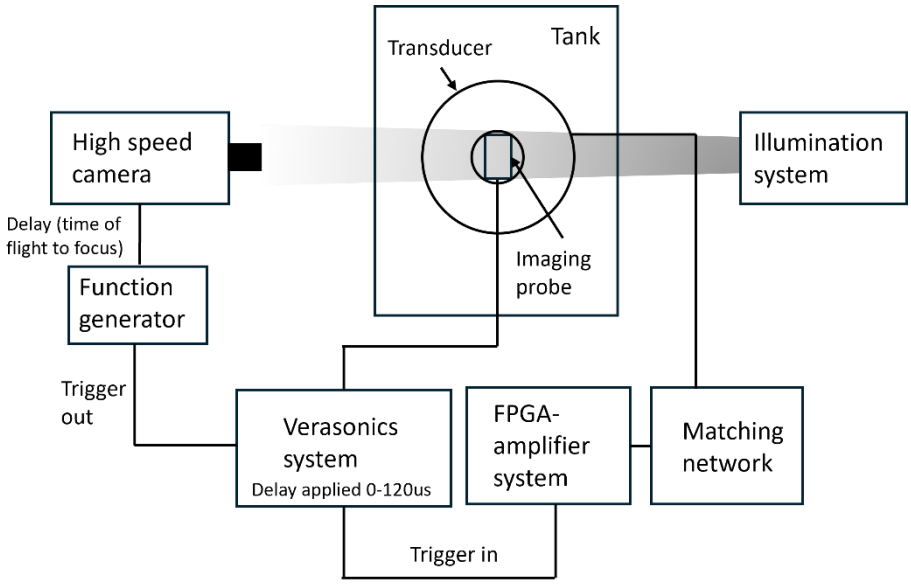

Figure 5.1. Experimental setup for visualizing a histotripsy cavitation cloud simultaneously by high-speed photography and plane wave B-mode imaging. The illumination system consists of an LED, lens, and a diffuser to obtain uniform light intensity in the optical image. A delay was applied between therapy and imaging transmission to avoid initial acoustic emissions from inertial cavitation. Additionally, another delay was applied after B-mode transmission to ensure high-speed photography images acquisition occurs simultaneously with B-mode.

Calibration of the focal pressure levels was conducted over a range of system driving voltages in degassed water by a fiber optic hydrophone (FOPH, RP acoustics, Leutenbach, Germany, 100 μm active diameter, 100 MHz bandwidth). Measurement could not be done beyond 85 V because of the occurrence of cavitation under the fiber tip at those voltage levels. To obtain focal pressure waveforms at those levels, axially symmetric nonlinear field simulations were performed using a freely available open-source high intensity focused ultrasound (HIFU)-beam software (https://limu.msu.ru/) based on solving the one-way propagation radially symmetric Westervelt equation. The input voltage to the transducer was assumed to be proportional to the characteristic

pressure at the transducer surface. The focal pressures from the simulations were matched to the experimentally calibrated points and extrapolated to higher voltages. Figure 5.2a and Table 5.7 show the focal pressures (peak positive and peak negative), and Figure 5.2b shows the representative focal waveform from simulations. The system was operated at five input voltages in total. Table 5.7 also shows the voltages and corresponding acoustic powers derived from acoustic field simulations. Consistent cavitation at every pulse occurred after 85 V.

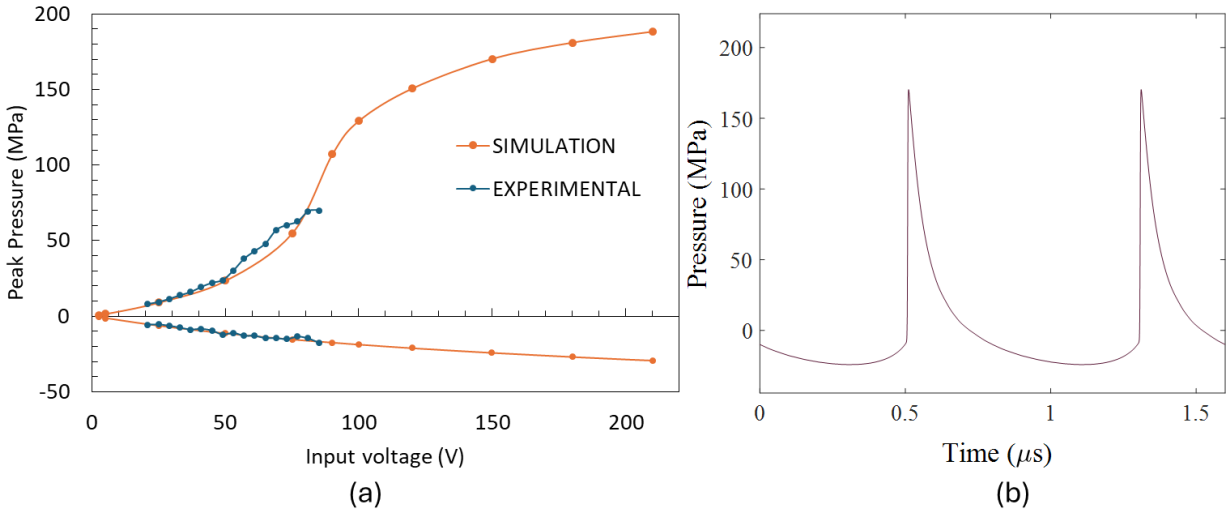

Figure 5.2. Transducer characterization. a) Focal pressures measured by experiments and obtained from simulations at increasing system input voltages, for a single element transducer (F#0.75, aperture 92.64 mm) at a center frequency of 1.2 MHz. Simulations were conducted in the software HIFUBEAM. b) Simulated focal waveform at a system input voltage of 150 V.

Table 5.7. Acoustic powers and peak focal pressures at the system input voltages derived from simulations. Consistent cavitation formation on every pulse was observed from 85 V.

Voltage (V)	Peak positive pressure (MPa)	Peak negative pressure (MPa)	Acoustic power (W)
90	107.13	-17.50	282
120	150.71	-21.14	501
150	170.35	-24.21	783
180	181.04	-26.89	1128
210	188.28	-29.29	1535

A high-speed camera (Photron Fastrax APS-RX, Photron, San Diego, CA, USA) was aligned orthogonally to the transducer's axial direction as shown in Figure 5.1. The camera was focused on the transducer's focal region using an 80–200 mm zoom lens to capture grayscale images of cavitation clouds at a resolution of 1024 x 1024 pixels with the shutter exposure time of 12.68 μs. The imaging probe was oriented to align the imaging planes of HSP and B-mode.

With the goal of capturing the same cavitation cloud by HSP and B-mode, different parts of the system were triggered in a specific manner as shown in Figure 5.3. The US imaging transmission was delayed (by 0, 20, 25, or 120 us) relative to the HIFU transducer transmission. The delays were applied to avoid interference of the strong acoustic signal from bubble emissions during cloud formation. The HSP system was triggered to capture a frame at the same instant of time that the B-mode imaging pulse reached the therapy focus. This was facilitated delaying the input to HSP system after B-mode imaging transmission by the time of flight from the transducer to therapy focus, which was realized by a function generator.

5.2.2. Cloud Size Estimation

Figure 5.4a,d show representative grayscale images of a cavitation cloud imaged by HSP and B-mode respectively. To calculate the area of the cloud, the images were processed in MATLAB (Natick, MA, USA) as follows. For HSP acquired images, first, background subtraction was conducted (Figure 5.4b). Cavitation clouds were identified using binary gray level thresholding segmentation as a group of white pixels (Figure 5.4c,e). The binary threshold was obtained by calculating the mean of Otsu threshold applied to all images (mean Otsu threshold = 0.1418). Otsu thresholding is an automatic method that determines an optimal threshold by maximizing the separation between foreground and background pixel intensities. The number of white pixels were counted, and pixel area was converted to square millimeters

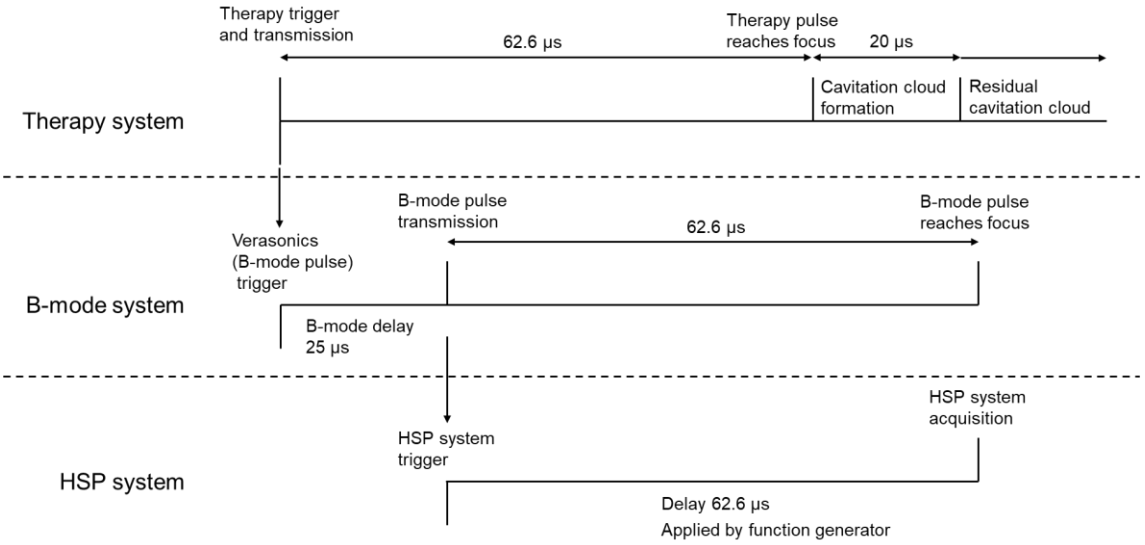

Figure 5.3. Triggering protocol for 25 µs B-mode delay. Therapy system is triggered, and the therapy pulse is transmitted instantaneously, taking 62.6 µs to reach the focus, after which the cavitation cloud forms for the duration of the pulse (20 µs). The B-mode system is triggered at the same instant as the therapy system, and a B-mode delay (in this case – 25 µs) was applied through verasonics. B-mode pulse transmission triggers the HSP system, which is delayed by the time B-mode pulse takes to reach the focus (62.6 µs), ensuring that the B-mode and HSP acquisitions are at the same instant.

(pixel length = 0.0227 mm). For the B-mode image, the same steps were followed without conducting background subtraction to obtain the area (A) in square millimeters (pixel length = 0.231 mm, mean Otsu threshold = 0.2577). At each combination of input voltage and imaging delay, eight acquisitions were conducted, and the mean and standard deviation of the cross-sectional area of the cavitation cloud were calculated for both modalities.

5.2.3. Statistical Analysis

Regression lines were fitted to the data sets wherever appropriate. T-test was used to determine the significance of the slopes of individual regression lines.

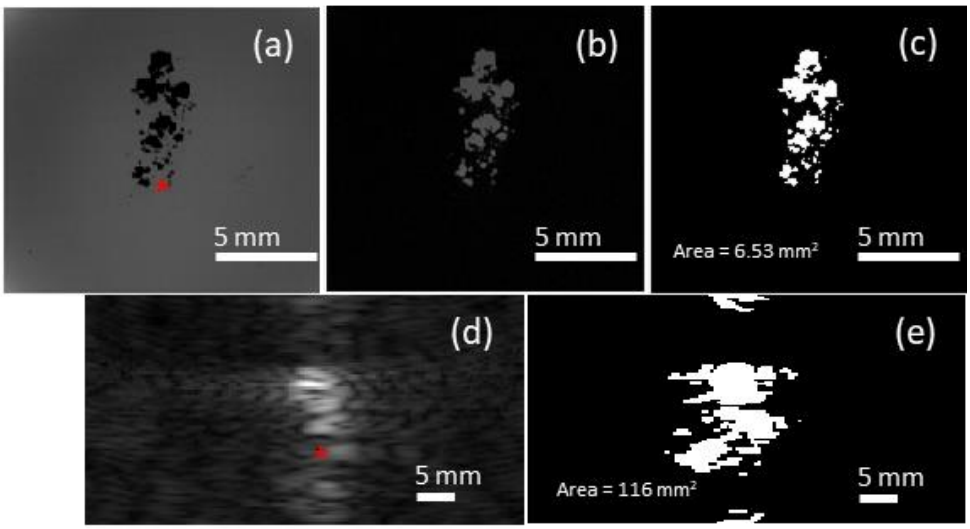

Figure 5.4. Cavitation cloud area estimation process. a) Grayscale image obtained by high-speed photography acquisitions (shutter exposure time = 12.68 μs). b) Background subtraction c) Grayscale to binary conversion, and area estimation for high-speed photography acquired image. d) Grayscale image obtained by plane wave B-mode imaging. e) Grayscale to binary conversion, and area estimation for plane wave B-mode image. Position of the geometric focus is indicated by a red asterisk.

5.3. RESULTS

5.3.1. B-mode Imaging Delay Optimization

Representative frames acquired by plane wave B-mode imaging at 150 V (783 W) at increasing delays are shown in Figure 5.5 a–d. Substantial brightness in the focal area is observed when B-mode imaging is not delayed after transducer transmission (Figure 5.5a). This is due to strong acoustic signals from violent bubble expansions and collapses as the HIFU pulse passes through focal region. Delaying B-mode acquisitions ensures receiving mostly backscattered US imaging signal from residual bubbles in the cloud. With increasing delay, bubble emissions from the clouds are seen as artifacts that are shifted to pre-focal region (Figure 5.5b,c), which, by 120 μs move out of the imaging window (Figure 5.5d). At 25 μs, the separation is sufficient to distinguish the artifact and the cloud represented by the backscattered signal.

The corresponding HSP acquired images are also shown at increasing delays in Figure 5.5 e–

h. At 0 us delay, a black region is visible pre-focally, corresponding to a dense cavitation cloud, which transitions to lighter shades of gray post-focally, indicating smaller and/or sparser bubbles. At 20 µs and 25 µs delays, only the black pre-focal regions are seen with no lighter shades. By 120 µs, a negligible cavitation activity is observed.

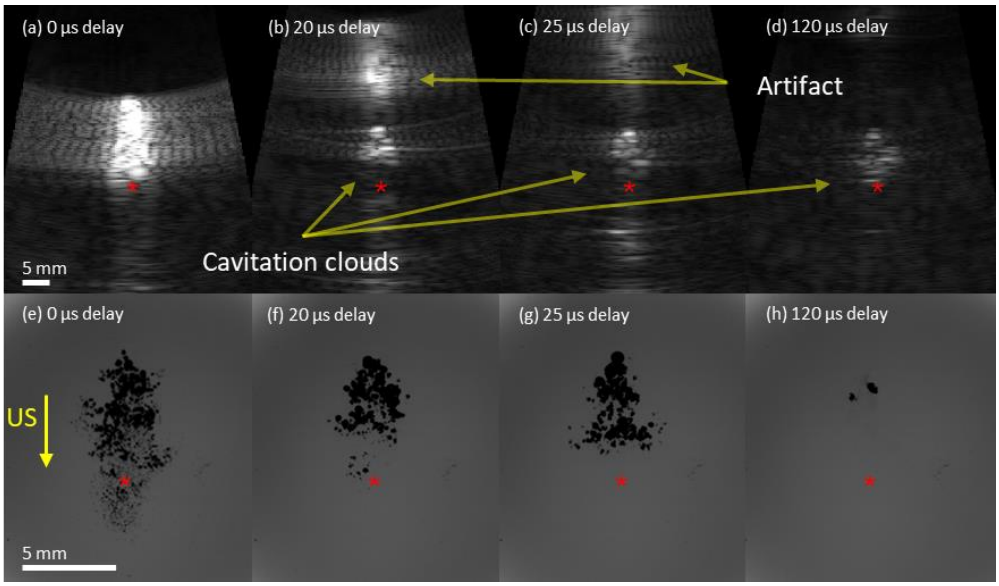

Figure 5.5. Plane wave B-mode and high-speed photography acquired images at different B-mode transmission delays after transducer transmission at acoustic power 783 W. At a particular delay, both images are of the same cavitation cloud. The arrow beside 'US' denotes the direction of ultrasound beam. Position of the geometric focus is indicated by a red asterisk.

5.3.2. Comparison of Cavitation Cloud Size Imaged by HSP and B-mode

Figure 5.6a shows the average cross-sectional area over a range of acoustic powers, imaged by HSP and B-mode. The regression lines fitted to both datasets are linear (HSP: $R^2 = 0.9604$, B-mode: $R^2 = 0.8798$), and show statistically significant linear increase with acoustic power (HSP: $p = 0.003$, B-mode: $p = 0.018$). Individual values of the average cross-sectional area imaged by B-mode are substantially higher than those imaged by HSP at each acoustic power level. Additionally, B-mode imaging shows higher variability as evidenced by larger error bars. Datasets were normalized with the minimum value (Figure 5.6b) to enable straightforward comparison. We observe cavitation cloud area imaged by HSP increases at a higher rate as shown by the slope.

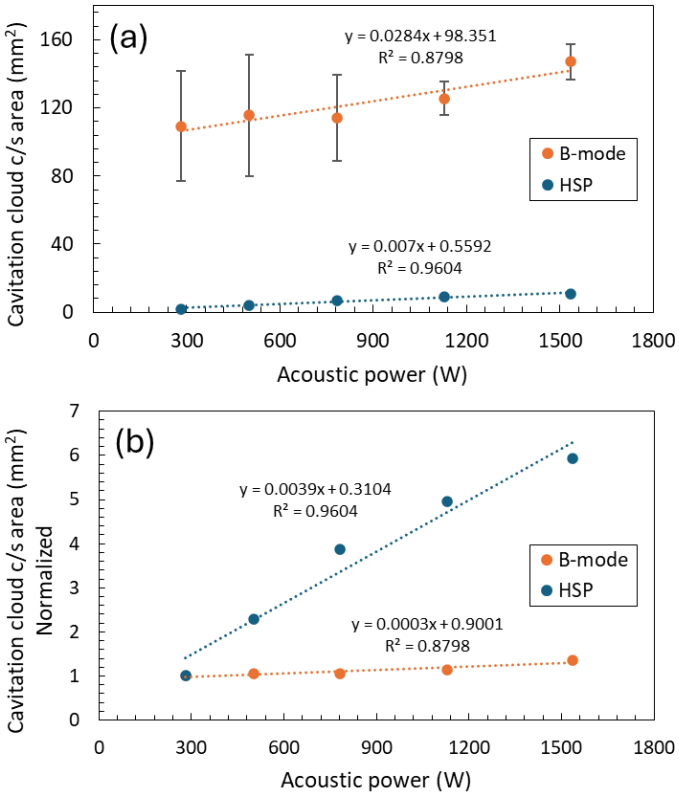

Figure 5.6. a) Dependence of cavitation cloud area estimated by plane wave B-mode imaging (B-mode) and high-speed photography (HSP) on acoustic power at 25 µs B-mode transmission delay. Eight replicates per data point. Linear regression lines are fitted to both data sets and the line equation as well as coefficient of regression are mentioned. b) The same datasets normalized with the minimum cloud c/s area value.

5.3.3. Comparison of Cavitation Cloud Shape Imaged by HSP and B-mode

Images of the same cavitation cloud imaged by HSP and B-mode are presented adjacent to each other at four different acoustic powers at a B-mode delay of 25 µs (Figure 5.7). All images have the same scale. Overall, B-mode images show higher axial and lateral dimensions of the cloud compared to HSP.

In Figure 5.7a, an independent round upper region of the cloud in the HSP image is visible, and corresponding independent hyperechoic region in B-mode image is also visible. At the lower end of the HSP image, small separated black regions are seen which possibly indicate post-focal bubbles, and corresponding post-focal hyperechoic regions in the B-mode image. Both are marked

by red circles. Figure 5.7b shows both images slightly skewed to the right. In Figure 5.7c, no distinct similarities between both images are found. In Figure 5.7d, two branches and a central region in the upper part of both images are visible.

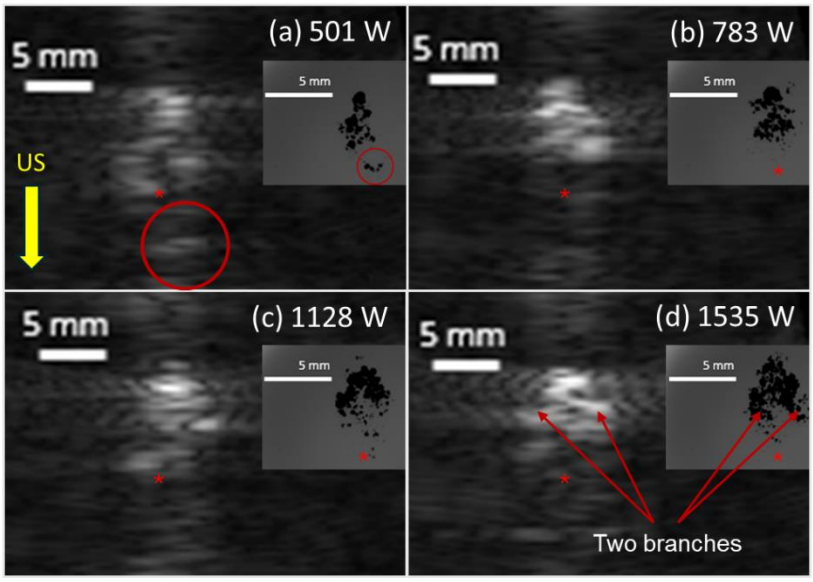

Figure 5.7. Representative frames of four cavitation cloud events imaged simultaneously by plane wave B-mode imaging and high-speed photography. The scale is equal for all images. (a) A cluster of bubbles separated from the continuous region of the cloud are marked by a red circle in the HSP image. In the corresponding B-mode image, the same cluster of bubbles may be indicated by post focal localized bright areas (marked by a red circle). Position of the geometric focus is indicated by a red asterisk.

5.4. DISCUSSIONS

The main aim of this study was to evaluate the capability of plane wave B-mode imaging in detecting changes in cavitation cloud size with increasing input acoustic power. Comparison was done with the HSP, because of its high spatial resolution due to direct optical observation, along with its established ability to detect cavitation cloud size changes [55]. The key result of this study is that the cloud size estimated from B-mode imaging linearly increases with the input acoustic power, which is also shown by HSP.

Delaying the B-mode transmission was necessary to avoid bright image artifacts caused by strong acoustic signals from violent bubble dynamics as the therapy pulse passed through the focal

region. At 25 μs B-mode delay, sufficient separation was seen in the B-mode image to distinguish between the emission artifacts and the echogenicity of the residual cavitation cloud. Ideally, a longer B-mode delay could provide a better representation of the cavitation cloud, because HIFU reverb (artifacts from multiple reflections of the therapy pulse) and point spread function artifacts (spatial blurring due to imaging system's finite resolution) were minimal at a B-mode delay of 120 μs (Figure 5.5d). However, the corresponding HSP image shows negligible cavitation presence at 120 μs delay, making it unsuitable for size comparison. This also suggests that HSP is less sensitive to smaller residual bubbles compared to B-mode. Therefore, a B-mode delay of 25 μs was considered optimal for size comparison studies, as it allowed clear visualization of the residual cloud while cavitation was still detectable in the corresponding HSP frame.

B-mode overestimates the cloud area as compared to HSP at the same acoustic power. This is expected and can be attributed to much lower lateral resolution in plane-wave B-mode images. Also, B-mode axial resolution (0.5 mm–one cycle at 3 MHz) is substantial considering the length of the cloud along axial dimension (4–5 mm).

Comparison of the cavitation cloud shape imaged by both modalities was conducted to validate whether B-mode images reflect the positions of bubbles and not random artifacts. Certain aspects of the experimental setup facilitated this comparison. The imaging probe was oriented such that the B-mode and HSP imaging planes are coplanar, ensuring that the cross-sections of the cloud were taken from the same plane. Additionally, the aperture size of the high-speed camera was adjusted to achieve a depth of focus (approx. 12 mm) comparable to the B-mode elevational plane thickness (approx. 10 mm). Both the depth of focus and B-mode plane thickness were experimentally determined, by laterally moving solid objects like rulers and paperclips from the imaging focus until the corresponding images lost sharpness.

Out of the representative images shown in Figure 5.7, a few similarities in the shape of the cloud between HSP and B-mode were identified, but the evidence is not overwhelming. One reason for the disagreement in shape can be higher sensitivity of B-mode in detecting smaller bubbles (Figure 5.5d,h), where focal brightness in B-mode image can be seen, while HSP shows negligible cavitation. Another possible reason could be overlapping of the signals (B-mode image) from the bubble expansions after the therapy pulse passes through the focus.

5.5. CONCLUSIONS

Histotripsy cavitation clouds were visualized simultaneously by two imaging modalities – plane wave B-mode imaging and high-speed photography in degassed water *in vitro*. Delaying the B-mode transmission after HIFU transmission was necessary to avoid interference from acoustic emissions. A delay of 25 μs was found to effectively separate echogenic residual bubbles from hyperechoic regions indicated by bubble emissions. It was found that B-mode overestimated the cavitation cloud size because of higher resolution, but still followed the same linear relationship with acoustic power as shown by high-speed photography. At 25 μs delay, plane-wave B-mode imaging showed some similarities in cavitation cloud shape imaged by HSP, although a comparison with HSP at zero delay would be more appropriate, considering HSP's inability to detect smaller residual bubbles.

Chapter 6. IN VITRO APPROACHES TO INACTIVATE S. AUREUS IN SUSPENSION BY HISTOTRIPSY

6.1. INTRODUCTION

In the previous chapters, *in vitro* investigations of the effects of histotripsy on *E. coli* were conducted. *E. coli* is a common inhabitant of abscesses. We now turn our attention to *Staphylococcus aureus* (*S. aureus*), which is also a frequent cause of abscesses, especially in soft tissues [63]. Notably, 91% of skin and soft tissue infections (SSTIs) in military personnel are caused by *S. aureus* [64]. A particular strain USA300 was the most frequently recovered bacterial isolate from SSTIs in 2004 [65]. Additionally, the emergence of antibiotic-resistant strains like Methicillin Resistant *Staphylococcus aureus* (MRSA) highlights the need for alternative approaches, like mechanical inactivation through histotripsy. This chapter reports initial steps toward that goal using monomicrobial cell suspensions in a bench-top setup.

The name *Staphylococcus aureus* has both Greek and Latin roots. Staphylococcus comes from the Greek words 'Staphyle' meaning 'bunch of grapes', and 'kokkos' meaning 'berry' or 'grain', referring to the characteristic grape-like structure when observed under microscope. The 'aureus' part is Latin for golden, describing the yellow-golden color of colonies when grown on blood agar plates. It is a gram-positive spherical bacterium that typically appears in aggregates or clumps. It readily forms biofilms, especially on medical devices and abscess capsules making infections persistent and hard to treat. *S. aureus* cells are typically 0.5–1.5 μm in diameter.

Focused ultrasound (FUS) has been used to inactivate *S. aureus* in various biological settings. For example, a significant FUS-induced thermal inactivation of *S. aureus* was observed in murine abscess models at 64°C [66]. Moreover, histotripsy has been used to disrupt biofilms from surfaces using cavitation, but not particularly to inactivate or kill bacteria within the biofilm matrix. Overall, no studies use focused ultrasound or histotripsy to treat *S. aureus* in suspensions in a bench-top

environment.

The effects of histotripsy on bi-microbial suspensions of *S. aureus* and *E. coli* were investigated *in vitro*, and an increase in *S. aureus* count post treatment was observed. Conversely, a significant decrease in *E. coli* counts was observed. Similar trends of higher resistance of *S. aureus* compared to *E. coli* was observed by other studies as well [67]. This result suggests a need for formulating alternative approaches to obtain significant *S. aureus* inactivation by histotripsy.

A hypothesis is that the initial increase in *S. aureus* counts is due to 'de-clumping' of bacterial aggregates into single cells, which are represented as one colony in colony-forming unit (CFU) assays, versus in the control, one colony likely represents a clump. Prior studies on cavitation-based ultrasound treatments report similar transient increases followed by bacterial reduction [68], [69], [70]. Histotripsy may follow the same trend, but within our time frames, the increase from de-clumping masks the inactivation. Therefore, in this study, an additional experimental control was taken after a few minutes of de-clumping, prior to treatment, to better isolate the effect of histotripsy.

A potential approach to increase the probability of histotripsy-induced bacterial damage is reducing the sample volume. Treating smaller volumes implies greater energy per unit volume and hence a greater possibility of kill. A two-fold increase was observed from 10 mL to 5 mL of *E. coli* when treated with focused ultrasound, and another two-fold increase in kill was observed for very small sample volumes (1 mL) although treated at a different frequency [39], [40]. In another study, a similar decreasing inactivation dependence was observed with increasing *E. coli* volumes from 100 mL to 200 mL [71]. A more detailed study was conducted on yeast using ultrasonic horns which showed an inverse relationship between percent kill and volume [24]. No studies treating smaller *S. aureus* volumes to increase kill probability are found in literature.

Another approach commonly applied to *S. aureus* in suspensions is thermosonication, primarily motivated by the food industry's desire to reduce temperatures required to kill microorganisms. Heat was shown to sensitize bacteria, while cavitation was primarily responsible for bacterial death [72]. Many studies using ultrasonic horns report a synergistic effect of thermosonication [69], [70]. In this chapter, the potential of histotripsy to damage *S. aureus* at higher, but sub-lethal temperatures is evaluated. Control experiments were also conducted by heating the samples to the same temperatures without histotripsy, to gauge the contribution of cavitation in *S. aureus* inactivation.

In thermosonication studies in the literature, the thermal effects were quantified by using temperature as an experimental variable, assuming a constant value over the treatment time. However, in practice, fluctuations might increase experimental errors especially when using highly temperature sensitive bacterial strains. Additionally, for setups that do not allow mid-treatment sampling, having a 'ring up' from the initial temperature (e.g. 37°C) to the target temperature (e.g. 55°C) is unavoidable. It is also very challenging to replicate the time-temperate exposures across treatments in these setups. Hence, to standardize the variability in thermal exposures, the concept of cumulative equivalent minutes at a specific reference temperature was applied. A variable named 'F-value' is used which indicates the equivalent time of a thermal process at a reference temperature that produces the same percent bacterial kill. This concept was initially introduced by C. Olin Ball in 1928 for more accurately quantifying sterilization processes of canned goods [73].

Overall, this chapter explores three strategies for enhancing histotripsy-induced *S. aureus* inactivation, as described in Table 6.8. De-clumping was applied as an initial step for all approaches. The first approach aimed at evaluating the potential of histotripsy to damage de-clumped, single cells. The second approach is the impact of histotripsy on 1 mL volumes. The

third approach investigated a combination of heat and histotripsy treatments using 'F-value' to quantify the thermal process.

Table 6.8. Hypothesis and rationale for histotripsy approaches to enhance *S. aureus* inactivation.

Approach	Hypothesis	Rationale
1	Histotripsy will inactivate de-clumped, single *S. aureus* cells	Bacteria in the interior of clumps are shielded, hence it is necessary to de-clump
2	Histotripsy will inactivate *S. aureus* cells in small (1 mL) volumes	Increased energy per bacterium with decreasing volume
3	Heat + histotripsy will have a synergistic bactericidal effect	Heat will compromise the integrity of bacterial cell walls leading to higher susceptibility to cavitation-induced damage

6.2. METHODS

6.2.1. Culture and Preparation

Clinical isolates of *S. aureus* USA300 were obtained from the Biodefense and Emerging Infections Research Resources Repository (BEI Resources, Manassas, VA, USA). The bacteria were maintained as liquid cultures in 3% tryptic soy broth (TSB) medium. Growth was monitored by periodically measuring the optical density at 600 nm (OD_{600}). The culture was used for treatments after reaching the stationary phase (OD_{600} = 1.4, ~10^8 CFU/mL) as predetermined from growth characteristics.

6.2.2. General Experimental Setup

A common experimental setup was used across all treatments, with some modifications undertaken in treatments on smaller volumes, as well as heat and histotripsy. A single-element transducer (H-161, Sonic Concepts, Bothell, WA, USA) with an aperture of 135 mm and a central opening of 47 mm diameter was driven by a controller (TPO-401, Sonic Concepts, Bothell, WA, USA) at a center frequency of 1.2 MHz and a pulse duration of 20 μs (24 cycles). The transducer was mounted to the bottom of a cylindrical polycarbonate tube (15.2 cm diameter, 0.8 cm wall thickness, and 18 cm in height) filled with degassed water (20°C–22°C) for coupling between the transducer and the

sample vial (Figure 6.1a). A polycarbonate sample vial (2.5 cm outer diameter, 0.3 cm wall thickness, and 4.6 cm height) containing 10 mL of bacterial culture (~10^8 cfu/mL) was attached to the water bath magnetically for precise alignment and repeatable positioning. The bottom of the cap was machined into a cone with its point immersed in the sample to reduce acoustic reflections. The bottom of each vial was replaced with an acoustically transparent polyethylene membrane held with an O-ring nested in an annulus machined into the bottom outer surface. The proximal wall of the membrane was wiped with a gauze sponge to eliminate pre-existing bubbles that could interfere with the ultrasound pulse. Two milliliters of 70% ethyl alcohol were introduced into the degassed water bath to reduce surface tension, thereby increasing the wettability of the membrane.

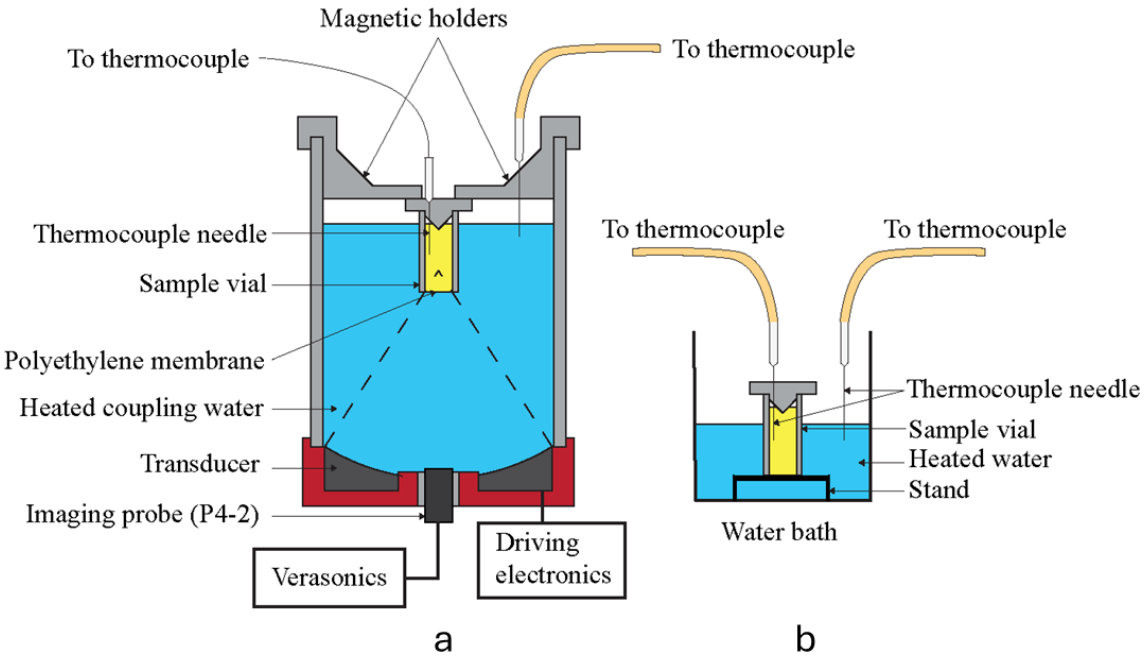

Figure 6.1. Experimental setup for heat + histotripsy and heat control treatments. A) A water bath containing degassed water at 37°C for heat + histotripsy treatments with a sonic concepts (H-161) transducer with the beam directed upward. The beam focus is in the acoustically transparent bottom sample vial. Sample and coupling water temperatures were monitored periodically by thermocouples. B) Heat control treatments. Sample vials were dipped in Fischer scientific water bath and temperature was monitored periodically.

The transducer focal pressure levels and acoustic powers at a range of system driving electric power levels were obtained by using a fiber optic hydrophone (FOPH 2000, RP Acoustics, Leutenbach, Germany; 100-μm active diameter, 100-MHz bandwidth) and conducting non-linear acoustic field simulations. This process is detailed in chapter 3.

6.2.3. Protocol for Approach 1 – De-clumping Step Followed by Histotripsy

Suspensions were treated at 494 W acoustic power for 1 minute at 1% duty cycle as a de-clumping step, followed by histotripsy treatment at 1836 W acoustic power for 40 minutes at 1% duty cycle. Samples were taken after 1-minute treatment (the 'control' after de-clumping) as well as 40-minute treatment. Viability assessment procedure will be explained in detail in a latter section.

6.2.4. Setup Modifications and Protocol for Approach 2 – Histotripsy on Small (1 mL) Sample Volumes

Ballistic gels with an axially symmetric 1 mL cylindrical cavity (10 mm diameter, 13 mm height) were fixed in the vials and positioned to have the focal volume within the cylindrical cavity. Prior to the treatments, the de-clumping step was conducted with 10 mL sample volumes from which 1 mL sample was transferred to the cylindrical cavity in the ballistic gel fitted vial. The detailed gel formation process is described in appendix C. Treatments were conducted at 633 W for 40 minutes.

6.2.5. Setup Modifications and Protocol for Approach 3 – Heat + Histotripsy

Some modifications were made for heat and histotripsy treatments. The coupling water was initially heated slightly above 37°C (38°C–38.5°C) using a heating immersion circulator (VWR 1112A) and poured carefully in the bath. Treatments were started when the bath temperature reached 37.5°C. The coupling water temperature steadily reduced to 36 ± 0.5°C over 40-minute treatments. The coupling water and sample temperatures were measured periodically by a thermocouple (Omega HH806AU , MT-23/5HT Needle Microprobe) with an accuracy of 0.1°C.

The thermocouple needle was permanently fixed at approximately one-quarter of the vial height from the top and positioned near the vial wall to prevent interference with the ultrasound beam path. The ultrasound input power was manually adjusted based on the thermocouple readings to maintain the sample at the target temperatures listed in Table 6.9.

Heat control experiments (Figure 6.1b) were conducted by using a heat bath (Fisher Scientific Isotemp 2332) and the same vials used in heat + histotripsy treatments. Bath water temperature was tracked by another thermocouple needle and was adjusted manually in response to temperature changes observed in the thermocouple to maintain the sample at target temperature. Calibration experiments were conducted beforehand to determine bath water volume, sample vial position in the bath (placed such that bath water was the same level as the sample vial) and bath temperature, for maintaining sample at target temperature.

Table 6.9. Pulse parameters for all studies. 1.2 MHz frequency and 20 μs pulse duration was applied for all treatments. The acoustic power data were used from our previous study [55]. Final temperatures for the heat + histotripsy treatment correspond to the intended target temperatures. 16 treatments were conducted for heat + histotripsy, whereas 48 data points were used for heat control treatments.

Strategy	Acoustic power (W)	Sample volume (mL)	Duty cycle %	Final Temperature (°C)	Treatment time (min)	Replicates
Histotripsy	1836	10	1	38.7 ± 0.8	40	3
Histotripsy (small volumes)	633	1	1	33.4 ± 1.3	40	3
Heat + histotripsy	384 to 930	10	2	45,50,52.5,55	10 to 40	16

6.2.6. Thermal Dose Calculation Process

The F-value was calculated by using equation 6.1 [73]. It represents the time at a specific temperature that results in the reduction of the bacterial population to a specified level. In our experiment, the reference temperature was considered as 50°C, because it was the lowest temperature at which significant kill was observed. Z-value is the temperature increase in degrees Celsius over which the thermal destruction (TD) curve traverses one log cycle, which was 8.33°C.

Formation of the TD curve for our biological system is provided in appendix B. For each treatment, i.e. time-temperature exposures for heat control as well as heat and histotripsy, F-value was calculated between two temperature measurements and summed to generate a cumulative F-value.

$$\text{F\_value} = 10^{\left(\frac{\text{T}-\text{T}_{REF}}{\text{z}}\right)} * \Delta\text{T}$$

Equation 6.1. Equation for calculating F-value, equivalent minutes at reference temperature (T_{REF}) of 50°C. Z-value is the inverse slope of thermal destruction curve (8.33°C in this case). Details of the thermal destruction curve are mentioned in appendix B. ΔT is the sampling time interval and T is the average temperature between sampling interval.

6.2.7. Viability Assessment

To assess the viability, samples withdrawn from the treated and untreated bacterial suspensions were subjected to serial dilutions with Environmental Protection Agency (EPA), Washington, DC, USA, dilution water (2 mM $MgCl_2$, 0.6 mM KH_2PO_4, pH 7.1) as a standard diluent using aliquots no smaller than 25 µL, as described previously. The diluted samples (1 mL) were deposited onto Compact Dry *S. aureus* XSA plates (Hardy Diagnostics, Santa Maria, CA, USA). Colonies were manually counted after incubation at 37°C for ~18 h, when the colonies were visible macroscopically. For the initial de-clumping 1-minute step and the following histotripsy treatment (approach 1), samples were heat fixed on slides and gram-stained and observed under light microscopy.

6.2.8. Statistical Analysis

The Wilcoxon rank sum test (non-parametric statistical test) was applied for approach 1 (histotripsy) and approach 2 (histotripsy on small sample volumes), to determine the significance of inactivation since normality and homoscedasticity cannot be assumed for our sample size (N = 3). For approach 3 (heat + histotripsy) regression lines were fitted to the data sets and t-test was used to determine the significance of the difference between the slopes of regression lines.

6.3. RESULTS

6.3.1. De-clumping Step

To evaluate the potential of histotripsy to de-clump bacterial cells, viability assay as well as light microscopy were employed. Figure 6.2a shows control and 1-minute treatment images. Significant clumping is observed in the control ranging from small clumps to larger sizes toward the right side. Some single cells are also visible. In the 1-minute, i.e. de-clumping treatment, single cells are seen to a large extent, with a few small sized clumps. Figure 6.2b shows insignificant log reduction for the de-clumping treatments (N = 3) obtained from viability assay comparisons.

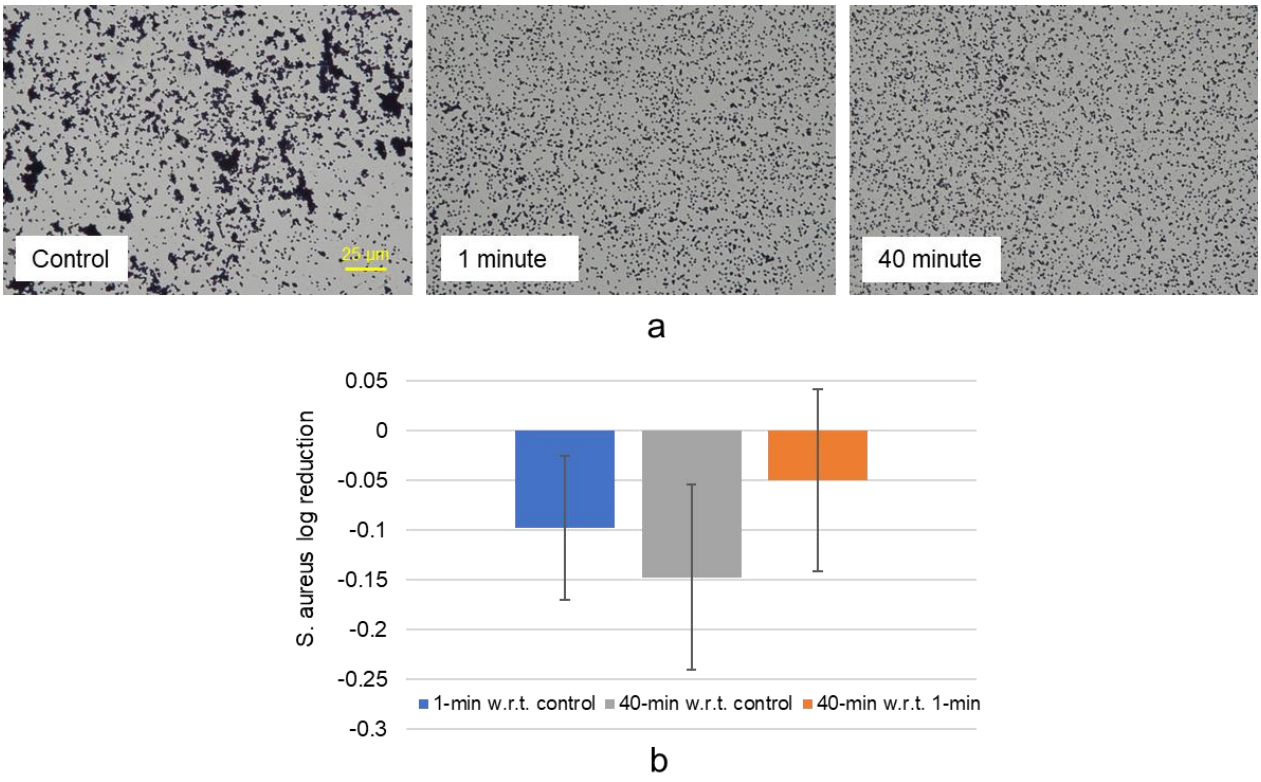

Figure 6.2. a) Light microscopy images (40x magnification) of *S. aureus* samples pre-treatment, post-de-clumping step (1-minute), and post histotripsy treatment. b) Mean *S. aureus* log reduction (N = 3).

6.3.2. Approach 1 – Histotripsy

Following the 1-minute de-clumping step, histotripsy was applied for 40 minutes using the

protocol shown in Table 6.9. Light microscopy image (Figure 6.2c) shows mostly single cells. Visually the cell density looks similar to de-clumped cells, but light microscopy results do not indicate viability [40]. The CFU counts insignificantly increase ($p = 0.11$) after 40-minute histotripsy treatment when compared to control, and also when compared to de-clumped counts ($p = 0.44$).

6.3.3. Approach 2 – Histotripsy for Small (1 mL) Sample Volumes

1 mL sample volumes were treated post-de-clumping with the protocol mentioned in Table 6.9. An insignificant change in the log kill (0.16 ± 0.44) was observed post-treatment ($p = 0.6$).

6.3.4. Approach 3 – Heat + Histotripsy

Sample temperatures recorded at specific time intervals during heat + histotripsy and heat control treatments are shown in Figure 6.3. Except at 55°C, the target temperature was reached within 10 minutes and maintained for the remainder of the treatment. Higher variability was observed during the initial heating phase, before the target temperature was achieved.

Figure 6.4 shows the dependence of *S. aureus* kill on the cumulative F-value (equivalent minutes at 50°C) on a log scale for heat control and heat + histotripsy experiments. The pulse protocol as well as the target temperatures are mentioned in Table 6.9. This covers the temperature range from 45°C to 55°C and 10-minute to 40-minute treatments. The regression followed a linear fit for both heat control ($R^2 = 0.69$) and heat + histotripsy ($R^2 = 0.94$) treatments. The x-intercept of both slopes is similar, 0.84 for heat control and 0.93 for heat + histotripsy. The difference between the slopes of the two regression lines is statistically insignificant ($p = 0.93$).

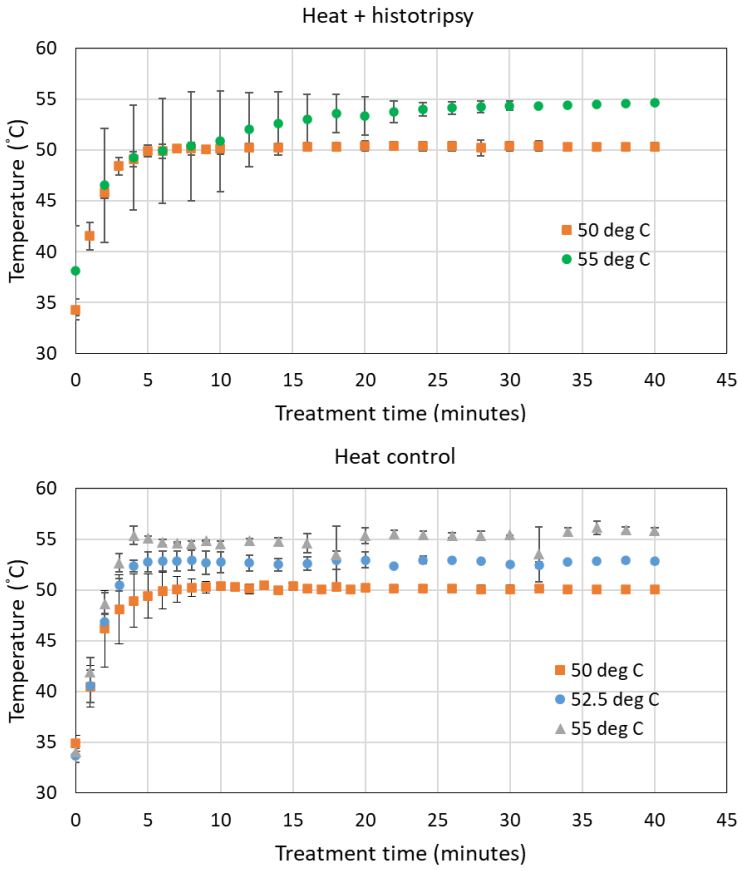

Figure 6.3. Time-temperature profiles of a) heat + histotripsy and b) heat control treatments.

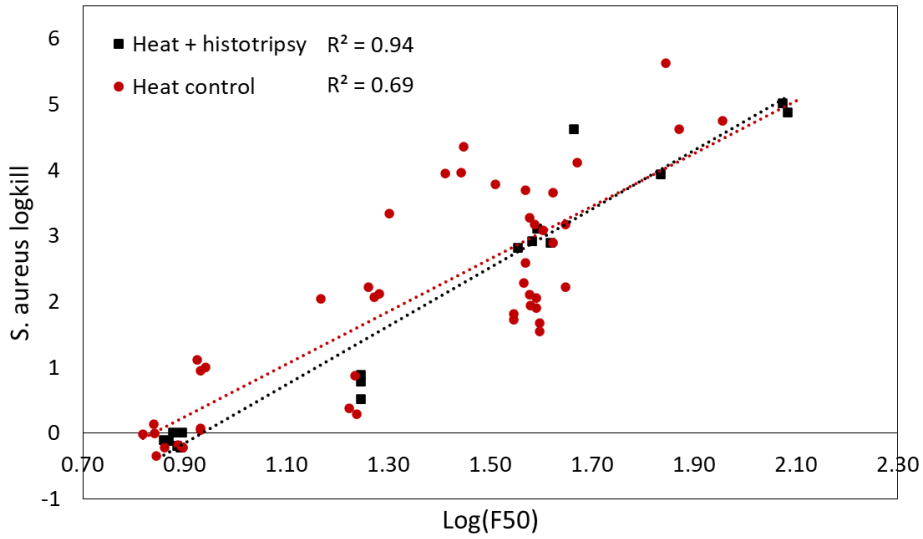

Figure 6.4. Log-log plot of *S. aureus* inactivation versus F-value at the reference temperature of 50°C for heat control and heat + histotripsy experiments. Both distributions are fitted with regressions and the difference in slopes are statistically insignificant.

6.4. DISCUSSIONS

The effects of histotripsy on *S. aureus* in suspension were investigated in this study. An increase in the bacterial count was observed in the first minute, which was attributed to de-clumping or separation of aggregates into individual cells. Hence, the de-clumped sample was considered as a control. Histotripsy was applied on 10 mL and 1 mL sample volumes, but an insignificant inactivation was observed. Since bacteria are susceptible to multiple inactivation mechanisms applied simultaneously, histotripsy treatment was combined with temperatures in the range of 45°C to 55°C. Significant inactivation was obtained at temperatures higher than 50°C, indicating the influence of thermal effects.

Light microscopy images show substantial clumps pre-treatment, and negligible clumps after 1-min treatment, which suggests that histotripsy causes bacterial de-clumping. However, this result is not supported by the viability assay, as it shows an insignificant change in the bacterial counts post 1-min treatment. Post de-clumping, histotripsy treatment was applied at the highest input power level achievable within the constraints of the electrical system. An insignificant change is observed compared to the de-clumped control as shown in Figure 6.2b This suggests that histotripsy is unsuccessful in inactivating partially de-clumped *S. aureus* cells.

An insignificant inactivation was also obtained after treating suspensions of smaller volumes (1 mL). This suggests that an increased exposure to cavitation-induced stresses was not enough to cause bacterial death. The hypothesis was formulated since volume dependence has been observed for other microorganisms like *E. coli* [40], B. cereus [68], yeast [24]. Although, as opposed to the current results, they obtained modest inactivation even at larger volumes. The current results indicate that decreasing the volume may not be an effective approach to inactivate *S. aureus* in suspensions at room temperature.

The third approach was named as ‘heat + histotripsy’. Traditionally, histotripsy is a non-thermal technique, but in this case, the parameters were deliberately chosen to generate substantial temperature increase (~55°C) in the target i.e. bacterial sample. Several factors are responsible for this temperature increase. Firstly, the duty cycle was increased from 1% to 2% to increase the total on-time to 48 seconds leading to more energy input within the same treatment time of 40 minutes. Secondly, the coupling-water was heated to 37°C, due to which it did not act as heat sync as it does when it is at room temperature. Hence, due to not allowing the heat to dissipate as easily and dumping more energy, increased temperatures were obtained even at histotripsy parameters like 20 µs, -13.7 MPa peak negative pressure, 93.2 MPa peak positive pressure. Interestingly, a group observed temperature increase up to 60°C with histotripsy parameters in *in vitro* kidney [74].

The time-temperature curves show a ramp-up in the first 10 minutes, and some fluctuations at the target temperature, justifying the use of F-value for temperature quantification. The concept of F-value was used to normalize our time-temperature data to equivalent minutes at a reference temperature. Specifically, in Figure 6.3a, the temperature reaches 55°C only toward the end of treatment and has high variability in the beginning. This can occur in our setup, where the operator manually adjusts the system input electrical power to bring the sample to the target temperature and maintain it there. Even so, the use of F-value compensates for such operator-induced variability.

A critical parameter in F-value calculation is the z-value, which was 8.33°C for our biological system. A great variation (from 3.37°C to 12.36°C) in z-value has been observed in the literature in different food matrices and bacterial strains [75]. However, only two temperatures were used to create the thermal destruction curve which is a limitation of this study. Higher number of temperatures will increase the accuracy of z-value.

Heat + histotripsy results show insignificant differences in slopes of the heat + histotripsy and heat control regression lines, indicating that the observed bacterial inactivation was primarily due to thermal effects. The thermal sensitivity of *S. aureus* is well established [76], [77]. A study using ultrasonic probes at a low frequency also showed that thermal effects dominated and cavitation played a negligible role in *S. aureus* inactivation [78]. Although cavitation did not contribute meaningfully in the current study, this result still has important clinical implications for the long-term goal of abscess disinfection. Since a clinically relevant inactivation (log kill>3) was obtained through thermal mechanism alone, MR-guided HIFU can be used to heat the abscess and monitor the time-temperature profile to deliver the required thermal dose in clinically relevant treatment times. To enable this protocol, *in vivo* studies are required to assess whether the thermal treatment causes coagulation of abscess contents, or prohibits potential liquefaction when needed, and whether heat can be confined to the target region without affecting adjacent tissues.

6.5. CONCLUSIONS

Histotripsy has an insignificant effect on *S. aureus* viability in 1 mL and 10 mL suspensions at room temperatures. However, histotripsy inactivates *S. aureus* at higher temperatures in the range of 50°C to 55°C, but the inactivation is mediated by thermal effects, not mechanical effects.

Chapter 7. INFLUENCE OF BACTERIAL SHAPE AND GRAM STATUS IN RESISTANCE TO HISTOTRIPSY

7.1. INTRODUCTION

In previous chapters, the effects of histotripsy on two bacteria – *E. coli* and *S. aureus* were investigated. Histotripsy was effective against *E. coli*, but had little to no impact on *S. aureus*. This chapter aims to explore the reason behind this contradictory result.

Bacteria are classified based on cell wall structure as gram-positive and gram-negative bacteria (Figure 7.1). Gram-positive bacterial cell envelope consists of cytoplasmic membrane and cell wall, whereas gram-negative bacterial cell envelope consists of cytoplasmic membrane, cell wall, outer membrane. Each layer contributes to resisting environmental stress. The outer membrane for gram-negative bacteria helps in resisting turgor pressure fluctuations [79]. In terms of structural support, resistance to turgor pressure, the cell wall consisting of the peptidoglycan layer is the most important element [80], [81]. Disruption of peptidoglycan layer causes osmotic pressure fluctuations leading to cell death [82]. It is 2–3 nm thick in gram-negative bacteria, and 20–80 nm thick in gram-positive bacteria. It consists of glycan strands which are cross-linked by peptide stems which create a mesh-like structure. The cytoplasmic membrane is a phospholipid bilayer, which is the innermost layer of the cell envelope. Its function is to regulate the movement of substances in and out of the cell. A bacterium dies when the cytoplasmic membrane is ruptured.

Bacteria can be classified based on their shape as spherical (coccus), rod-shaped (bacillus), and spiral-shaped. Shape is governed by the architecture of the peptidoglycan layer and cytoskeletal elements, which influence cell wall growth patterns. These morphological differences also affect cell arrangement, with cocci often forming clusters and rods forming chains or remaining isolated.

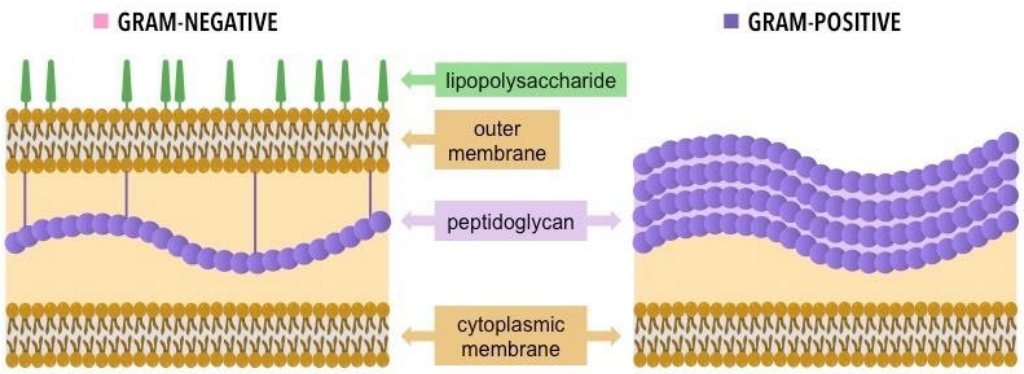

Figure 7.1. A simplified illustration of the cell envelopes of gram-negative bacteria (left) and gram-positive bacteria (right) [83].

Bacterial characteristics can influence their resistance to ultrasound-induced cavitation. Gram-positive bacteria are more resistant to mechanical stresses induced by cavitation [78], [84], [85]. Moreover, spherical bacteria are reported to be more resistant than rod-shaped bacteria [86], potentially because they have lesser surface area exposed to cavitation-induced forces as compared to rods, resulting in reduced shear stress effects. However, some studies do not observe any dependence on bacterial characteristics and attribute the damage solely to bacterial species [34], [87].

The hypothesis is that *S. aureus* is more resistant to histotripsy treatment than *E. coli* by the virtue of its gram-status (gram-positive), and shape (sphere). However, it is unclear whether to attribute the higher resistance to its shape, gram status, or a combination of both. To address this, additional bacterial species of different combinations of shape and gram status were treated: *Bacillus cereus* (gram-positive rod), and *Neisseria subflava* (gram-negative sphere).

7.2. METHODS

Description of the treatment setup is provided in chapter 4. Histotripsy protocol of 1.2 MHz frequency, 20 µs pulse duration, 1473 W acoustic power, duty cycle of 1%, and treatment time of 40 minutes was applied. The de-clumping step was applied using the same pulse protocol for 1

minute at 494 W for all bacteria.

7.2.1. Culture and Preparation

Four bacteria were used, *E. coli* FDA strain Seattle 1946, *Staphylococcus aureus* USA300, *Bacillus cereus* NCTC 11145, and *Neisseria subflava* CDN-17. All bacteria except *N. subflava* were maintained as liquid cultures in 3% tryptic soy broth (TSB) medium. *N. subflava* was cultured in 3% TSB supplemented with 6g/L yeast extract and 8g/L glucose, and maintained in an atmosphere of 5% CO_2. Bacterial growth was monitored by periodically measuring the optical density at 600 nm (OD_{600}). The culture (10 mL sample volume) was used after reaching the stationary phase, as predetermined from previous growth characteristics studies. Table 7.10 shows OD_{600} and CFU/mL at the stationary phase.

Table 7.10. Information on bacterial strains used in the study.

Bacteria	Strain	Shape	Gram stain	Size	Plate type	OD600, CFU/mL @ stationary phase
E. coli	FDA strain Seattle 1946	Rod	Gram negative	1–3 µm long × 0.5–1 µm wide	EC	1.2, ~10^9
B. cereus	NCTC 11145	Rod	Gram positive	3–5 µm long × 1–1.5 µm wide	TC	0.6, ~10^7
S. aureus	USA300	Sphere	Gram positive	0.5–1.5 µm diameter	XSA	1.4, ~10^8
N. subflava	CDN-17	Sphere	Gram negative	0.6–1.0 µm diameter	TC	1.4 ,~10^9

7.2.2. Viability Assessment

Viability assessment protocol from chapter 2 was applied for all bacteria. Table 7.10 specifies the bacterial strains, and the type of plates used for CFU evaluation.

7.2.3. Statistics

Single-factor ANOVA test was applied to determine the statistical significance of log reduction across bacterial groups, followed by a post hoc Tukey's HSD test to determine pairwise differences

between species.

7.3. RESULTS

Figure 7.2 shows the mean log reduction values (N = 6) for the four bacteria under the same treatment parameters. Table 7.11 shows statistical comparisons across all bacteria. *E. coli* log reduction is significantly greater than all other species, whereas the log reduction of *B. cereus* is significantly greater than *S. aureus* and *N. subflava*, which are insignificantly different from each other.

Table 7.11. Tukey HSD test results. Statistical comparison of mean log reductions between all bacteria.

Bacteria pair	Shape and gram status description	Tukey HSD statistic	Tukey HSD p-value	Tukey HSD inference
E. coli vs B. cereus	G-ve rod vs G+ve rod	4.56	0.020	Significant
E. coli vs S. aureus	G-ve rod vs G+ve sphere	22.94	0.001	Significant
E. coli vs N. subflava	G-ve rod vs G-ve sphere	22.10	0.001	Significant
B. cereus vs S. aureus	G+ve rod vs G+ve sphere	18.38	0.001	Significant
B. cereus vs N. subflava	G+ve rod vs G-ve sphere	17.54	0.001	Significant
S. aureus vs N. subflava	G+ve sphere vs G-ve sphere	0.84	0.899	Insignificant

Figure 7.2 shows the mean log reductions (N = 6) for all bacteria used in the study under equivalent treatment conditions. *E. coli* (gram-negative rod) was inactivated the most, at a mean log reduction of 2.95, followed by *B. cereus* (gram-positive rod) at 2.37. The mean log reductions of *S. aureus* and *N. subflava* were very low, 0.01, and 0.11 respectively.

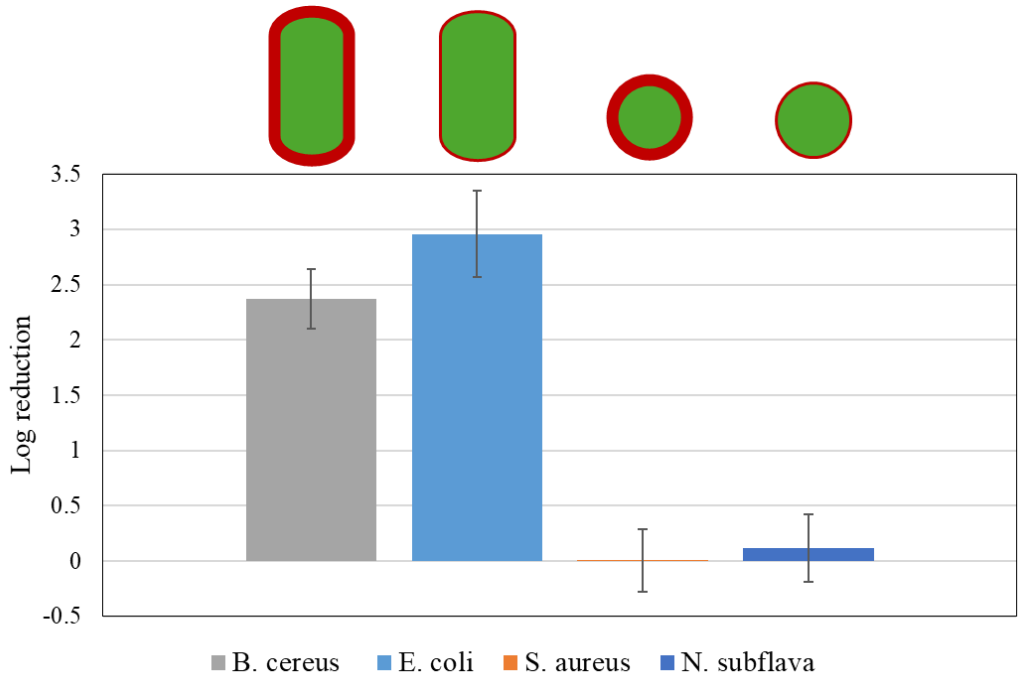

Figure 7.2. Log reduction (N = 6) of 10 mL suspensions of four bacteria by histotripsy treatment with 1.2 MHz, 20 µs, 1473 W acoustic power, 1% duty cycle for 40 minutes. illustrations describing shape and gram status are shown above the bars. Gram positive bacteria having thicker cell wall are indicated by a thicker red outline.

7.4. DISCUSSIONS

This study investigated the influence of bacterial shape and gram status on their resistance to histotripsy-induced cavitation. Results show significant inactivation of rod-shaped bacteria as opposed to insignificant inactivation of spherical bacteria. These findings are the first instance of using bacteria of all four combinations of gram status and shape under the same conditions of ultrasound treatment.

The effect of gram status was apparent only in rod-shaped bacteria, with gram-positive bacteria (*B. cereus*) being more resistant than gram-negative bacteria (*E. coli*). Physically, this makes sense, because a thicker cell wall (peptidoglycan layer) would present more resistance to cavitation-induced mechanical forces. A paper numerically studying the effects of a single cavitation bubble collapse near a bacterium observed higher peak local stress and peak local

elongation for gram-negative bacteria compared to gram-positive bacteria [88]. However, the effect of gram status was not observed in spherical bacteria, indicating that the shape had a greater influence on bacterial resistance to ultrasonic cavitation.

Bacterial shape had a significant contribution to the resistance against cavitation, as indicated by the negligible inactivation of the spherical bacteria (*S. aureus*, *N. subflava*) regardless of gram status. A technical report has noted that rounder bacteria are more resistant to ultrasonic cavitation than rod-shaped counterparts [86]. However, beyond this mention, there are no discussions in the literature related to the influence of bacterial shape on cavitation susceptibility. The observed differences can be interpreted by examining the mechanical implications of spherical versus rod-like geometries. Firstly, rod-shaped bacteria generally possess greater size than spherical bacteria of similar diameter, owing to their additional length. This results in a larger surface area being exposed to external forces, and consequently a higher total shear load under uniform stress conditions. Secondly, spherical bacteria, owing to their isotropic geometry, are likely to experience more uniform stress distributions under external mechanical loading, thereby reducing the likelihood of localized stress concentrations. Thirdly, rods are mechanically susceptible to bending under non-uniform force fields, whereas spheres are not, further contributing to the enhanced vulnerability of rod-shaped bacteria to cavitation-induced stresses [89].

Since complex biological systems like bacteria were considered, some intricacies were ignored to enable comparison. Firstly, *S. aureus* cell wall contains a comparatively higher degree of cross-linking in the form of pentaglycine bridges potentially leading to better viscoelastic properties, a factor that could have contributed to resistance against cavitation [90]. Secondly, B. cereus is slightly greater in size as compared to *E. coli* (see Table 7.10), which can potentially influence susceptibility, since larger cells are more susceptible to cavitation [81]. Additionally, the

longer axial dimension of *B. cereus* compared to *E. coli* might also enhance its susceptibility. This is because elongated geometries experience greater bending deformation since the bending stress is proportional to the square of length [89].

N. sublfava cultures were maintained at 5% CO_2 atmosphere unlike the other bacteria used in the study. This likely resulted in a modified dissolved gas composition with elevated CO_2 levels in the culture. Such conditions could influence bubble dynamics as CO_2 is observed to suppress cavitation by reducing the likelihood of cavitation nuclei formation [91].

In this study, only four representative bacteria were chosen for all combinations of gram-stain and shape i.e. only one bacterium per combination. However, the possibility of the same combination having different resistance to cavitation cannot be ignored. For example, in a study evaluating the bactericidal effects of ultrasonication in milk, *Chryseobacterium meningosepticum* (*C. meningosepticum*) was found to be more resistant than *E. coli*, both being gram-negative rods. Similarly, *Lactobacillus acidophilus* (*L. acidophilus*) was more resistant than *Listeria monocytogenes* (*L. monocytogenes*) (both gram-positive rods) [92]. This might be possible due to unique cell membrane adaptations, stress response pathways, and differences in the cell wall thickness (*E. coli* - 6 nm, *C. meningosepticum* - 7 nm, *L. acidophilus* - 65 nm, *L. monocytogenes* - 40 nm). Hence, additional bacteria need to be considered for an exhaustive analysis.

7.5. CONCLUSIONS

Gram-positive bacteria may be more resistant to histotripsy than gram-negative bacteria, but this trend appears to hold primarily for rod-shaped species. Bacterial shape is a significant contributor to their resistance to histotripsy, with sphere shaped bacteria inactivating insignificantly irrespective of gram status. Thus, both shape and gram status might have contributed to the increased resistance of *S. aureus* to histotripsy compared to *E. coli*, with shape (sphere) having a

greater contribution than its gram status (gram-positive).

Chapter 8. CONCLUDING REMARKS

The motivation of this dissertation was to understand the effects of histotripsy on bacterial viability in suspension to inform histotripsy-based abscess treatment. All studies were conducted *in vitro* with a HIFU transducer coupled to the bacterial sample via degassed water bath. Pre-treatment and post-treatment bacterial viability was estimated by plate counting assay method. The dependence of bacterial inactivation was studied on acoustic parameters like peak negative pressure amplitude, pulse duration, duty cycle, and cavitation parameters like cavitation cloud size. The following sub-section explains how the understanding gained through *in vitro* studies will inform clinical abscess treatment, which is followed by the broader implications of the dissertation, and recommended future work.

8.1. IMPLICATIONS FOR CLINICAL ABSCESS TREATMENT

Firstly, in chapter 2, the bactericidal capability (for *E. coli*) of shock-scattering histotripsy (CH) and boiling histotripsy (BH) was compared. CH was more effective at higher pressures, and BH was more effective at lower pressures. Thus, in conditions allowing for the use of high in situ pressure levels – superficial abscesses, relatively small volumes and favorable heat dissipation dynamics – CH would be the preferred treatment modality. For deeper abscesses, where excessively high-pressure levels may not be advisable because of the potential for heat buildup in the intervening tissues or in the abscess itself, the use of BH may be preferable.

Secondly, in chapters 3, 4, 5, cavitation cloud size in shock-scattering histotripsy was quantified by two imaging modalities and its capability to predict *E. coli* inactivation was explored. Chapter 3 was a proof-of-concept study in which *E. coli* inactivation strongly correlated with optically measured cavitation cloud area, over a diverse acoustic parameter space including three different frequencies, several pulse lengths and acoustic power levels. In chapter 4, cavitation

cloud size was normalized with bacterial sample volume, and *E. coli* inactivation strongly correlated with the normalized metric across three volumes and three acoustic power levels. In chapter 5, cavitation cloud imaged by plane-wave B-mode imaging (a clinically relevant imaging modality) was shown to follow linearly increasing size dependence on acoustic power, like optical imaging. These findings suggest that *E. coli* inactivation rates can be predicted in clinical abscess treatments by quantifying cloud size and abscess volume by plane-wave B-mode imaging.

Thirdly, in chapter 6, different approaches of histotripsy on *S. aureus* were explored following the observation of negligible *S. aureus* inactivation at treatment parameters sufficient to significantly inactivate *E. coli*. Approaches consisted of bacterial de-clumping followed by histotripsy, histotripsy on smaller sample volumes of 1 mL, and heat + histotripsy. Histotripsy-induced cavitation insignificantly inactivated *S. aureus* in all three approaches. On the other hand, histotripsy-induced heat was successful in inactivating up to log 5. Hence, thermal inactivation by HIFU like parameters can be explored for clinical *S. aureus* abscess treatments as an alternative to histotripsy. However, a potential disadvantage of this approach would be thermal coagulation of abscess contents due to high temperatures leading to difficulty in drainage.

8.2. BROADER IMPLICATIONS

This dissertation provides insights into the type of bacterial inactivation mechanism by histotripsy. There are currently two accepted mechanisms, namely mechanical effects associated with the shear forces during bubble collapse, and sonochemical effects associated with chemical reactions caused by breakage of bonds of the water molecule by the energy created during bubble collapse. Sonochemical effects create an acidic environment due to the formation of hydrogen peroxide. The pH of the bacterial growth medium was tested pre-treatment and post-treatment, and insignificant difference in pH was observed ($p = 0.9$). Additionally, since sonochemical

mechanism involves chemical attack on the cell walls, the effect of bacterial shape should be negligible [28]. However, a substantial effect of the shape in resistance to cavitation was observed in chapter 7. These results suggest that histotripsy is not inducing measurable sonochemical effects. On the other hand, ruptured *E. coli* membranes were found in TEM images in a study that used histotripsy parameters [40], which suggests that histotripsy predominantly induces mechanical effects.

Cavitation was quantified and successfully correlated to bacterial inactivation. This is an important finding in the context of taking a step toward uncovering the detailed physical mechanism (bubble jetting, bubble-induced shear forces, etc.) of bacterial inactivation by ultrasound-induced cavitation. A review article [21] highlights the importance of quantifying cavitation to consistently compare results across studies. Some works only quantified cavitation without correlating metrics to bacterial inactivation [93], whereas some quantified the cavitation dose, but a weak correlation was observed [38], [45]. More empirical studies connecting cavitation metrics to bacterial inactivation are needed to build a robust basis for investigating the underlying physical mechanism.

The concept of F-value, to obtain equivalent minutes at a reference temperature, was used in the context of thermosonication (heat + histotripsy) for the first time to the author's knowledge. F-value takes into consideration the initial temperature increase from room temperature to target temperature, as well as fluctuations due to experimental errors, thus quantifying the thermal process more effectively.

8.3. RECOMMENDED FUTURE WORK

Cavitation cloud size was quantified by averaging the area or volume across multiple frames, which resulted in high variability (Figure 3.6, Figure 3.7, Figure 5.6), which can be attributed to

the stochastic nature of cavitation. A better approach would be combining multiple grayscale image frames at a specific input power setting and representing cavitation clouds as cavitation probability distributions. Since the optical cloud images show dark regions at the focus and lighter regions post-focally (Figure 3.4, Figure 3.5), the distributions would show an elliptical region of high probability at the focus enveloped by regions indicating lower probability. Correlations can be made between the areas of different probability regions and *E. coli* inactivation to gain further insights into the bacterial inactivation mechanism.

The de-clumping step in chapter 6 was an important finding. However, it cannot be said with high confidence that a substantial number of *S. aureus* clusters were de-clumped, which is indicated by light microscopy and viability assay results. In the future, optimum de-clumping time needs to be determined by increasing the number of replicates and de-clumping times.

In chapter 7, the effect of bacterial shape and gram status on the resistance to inactivation were investigated by treating only four bacteria, each representing one combination of shape and gram status. However, *S. aureus* cell wall is unique (higher cross-linking), rod-shaped bacteria in the study are not of the same size, and because bacteria with same shape and gram status might still respond differently to cavitation-induced stresses, additional bacteria need to be considered in future studies. The author further recommends initially excluding Staphylococcus species in such comparative analyses because of their unique cell wall architecture, which might potentially contribute to its resistance and may confound the interpretation of results. Once the effects of the shape and gram status are better understood using more representative bacteria, *S. aureus* can then be explored separately.

All studies in this dissertation were experimental in nature. However, numerical modeling of the interactions between bubbles and bacteria can provide valuable insights into the fundamental

mechanisms of inactivation. Several studies have modeled the effects of a single cavitation bubble on nearby rigid [94] and compliant biological structures such as liposomes [95], red blood cells [96], and bacteria [88]. Such efforts have shown that even a single collapsing microbubble can produce substantial mechanical stress on nearby membranes. Future studies can explore similar modeling approaches for bacteria of different shapes and gram status and eventually extend to more complex scenarios involving multiple interacting bubbles (i.e. cavitation clouds) to better mimic the exposure conditions in therapeutic applications.

BIBLIOGRAPHY

[1] A. F. Cardona and S. E. Wilson, "Skin and Soft-Tissue Infections: A Critical Review and the Role of Telavancin in Their Treatment," *Clin Infect Dis.*, vol. 61, no. suppl 2, pp. S69–S78, Sep. 2015, doi: 10.1093/cid/civ528.

[2] D. Muzumdar, S. Jhawar, and A. Goel, "Brain abscess: An overview," *International Journal of Surgery*, vol. 9, no. 2, pp. 136–144, 2011, doi: 10.1016/j.ijsu.2010.11.005.

[3] D. Robertson and A. J. Smith, "The microbiology of the acute dental abscess," *Journal of Medical Microbiology*, vol. 58, no. 2, pp. 155–162, Feb. 2009, doi: 10.1099/jmm.0.003517-0.

[4] D. J. Pallin, D. J. Egan, A. J. Pelletier, J. A. Espinola, D. C. Hooper, and C. A. Camargo, "Increased US Emergency Department Visits for Skin and Soft Tissue Infections, and Changes in Antibiotic Choices, During the Emergence of Community-Associated Methicillin-Resistant Staphylococcus aureus," *Annals of Emergency Medicine*, vol. 51, no. 3, pp. 291–298, Mar. 2008, doi: 10.1016/j.annemergmed.2007.12.004.

[5] N. G. Uspal, J. R. Marin, E. R. Alpern, and J. J. Zorc, "Factors associated with the use of procedural sedation during incision and drainage procedures at a children's hospital," *The American Journal of Emergency Medicine*, vol. 31, no. 2, pp. 302–308, Feb. 2013, doi: 10.1016/j.ajem.2012.07.028.

[6] A. Elixhauser, "Readmissions to U.S. Hospitals by Diagnosis, 2010".

[7] K. J. Mortelé *et al.*, "CT-Guided Percutaneous Catheter Drainage of Acute Necrotizing Pancreatitis: Clinical Experience and Observations in Patients with Sterile and Infected Necrosis," *American Journal of Roentgenology*, vol. 192, no. 1, pp. 110–116, Jan. 2009, doi: 10.2214/AJR.08.1116.

[8] Zhen Xu *et al.*, "Controlled ultrasound tissue erosion," *IEEE Trans. Ultrason., Ferroelect., Freq. Contr.*, vol. 51, no. 6, pp. 726–736, Jun. 2004, doi: 10.1109/TUFFC.2004.1304271.

[9] A. D. Maxwell *et al.*, "Cavitation clouds created by shock scattering from bubbles during histotripsy," *The Journal of the Acoustical Society of America*, vol. 130, no. 4, pp. 1888–1898, Oct. 2011, doi: 10.1121/1.3625239.

[10] M. S. Canney, T. D. Khokhlova, V. A. Khokhlova, M. R. Bailey, J. Ha Hwang, and L. A. Crum, "Tissue Erosion Using Shock Wave Heating and Millisecond Boiling in HIFU Fields," in *9th International Symposium on Therapeutic Ultrasound: ISTU - 2009*, K. Hynynen and J. Souquet, Eds., in American Institute of Physics Conference Series, vol. 1215. AIP, Mar. 2010,

pp. 36–39. doi: 10.1063/1.3367183.

[11] T. D. Khokhlova, M. S. Canney, V. A. Khokhlova, O. A. Sapozhnikov, L. A. Crum, and M. R. Bailey, “Controlled tissue emulsification produced by high intensity focused ultrasound shock waves and millisecond boiling,” *The Journal of the Acoustical Society of America*, vol. 130, no. 5, pp. 3498–3510, Nov. 2011, doi: 10.1121/1.3626152.

[12] K. J. Pahk, P. Gélat, D. Sinden, D. K. Dhar, and N. Saffari, “Numerical and Experimental Study of Mechanisms Involved in Boiling Histotripsy,” *Ultrasound in Medicine & Biology*, vol. 43, no. 12, pp. 2848–2861, Dec. 2017, doi: 10.1016/j.ultrasmedbio.2017.08.938.

[13] J. C. Simon, O. A. Sapozhnikov, V. A. Khokhlova, Y.-N. Wang, L. A. Crum, and M. R. Bailey, “Ultrasonic atomization of tissue and its role in tissue fractionation by high intensity focused ultrasound,” *Phys. Med. Biol.*, vol. 57, no. 23, pp. 8061–8078, Dec. 2012, doi: 10.1088/0031-9155/57/23/8061.

[14] T. Hall, J. Fowlkes, and C. Cain, “A real-time measure of cavitation induced tissue disruption by ultrasound imaging backscatter reduction,” *IEEE Trans. Ultrason., Ferroelect., Freq. Contr.*, vol. 54, no. 3, pp. 569–575, Mar. 2007, doi: 10.1109/TUFFC.2007.279.

[15] K. B. Bader, E. Vlaisavljevich, and A. D. Maxwell, “For Whom the Bubble Grows: Physical Principles of Bubble Nucleation and Dynamics in Histotripsy Ultrasound Therapy,” *Ultrasound in Medicine & Biology*, vol. 45, no. 5, pp. 1056–1080, May 2019, doi: 10.1016/j.ultrasmedbio.2018.10.035.

[16] E. Vlaisavljevich *et al.*, “Non-Invasive Liver Ablation Using Histotripsy: Preclinical Safety Study in an In Vivo Porcine Model,” *Ultrasound in Medicine & Biology*, vol. 43, no. 6, pp. 1237–1251, 2017, doi: https://doi.org/10.1016/j.ultrasmedbio.2017.01.016.

[17] T. A. Bigelow, C. L. Thomas, H. Wu, and K. M. F. Itani, “Histotripsy Treatment of *S. Aureus* Biofilms on Surgical Mesh Samples Under Varying Pulse Durations,” *IEEE Trans. Ultrason., Ferroelect., Freq. Contr.*, vol. 64, no. 10, pp. 1420–1428, Oct. 2017, doi: 10.1109/TUFFC.2017.2718841.

[18] M. Smallcomb and J. C. Simon, “Dual-frequency boiling histotripsy in an ex vivo bovine tendinopathy model,” *The Journal of the Acoustical Society of America*, vol. 153, no. 6, pp. 3182–3182, Jun. 2023, doi: 10.1121/10.0019630.

[19] A. D. Maxwell, G. Owens, H. S. Gurm, K. Ives, D. D. Myers, and Z. Xu, “Noninvasive Treatment of Deep Venous Thrombosis Using Pulsed Ultrasound Cavitation Therapy

(Histotripsy) in a Porcine Model," *Journal of Vascular and Interventional Radiology*, vol. 22, no. 3, pp. 369–377, 2011, doi: https://doi.org/10.1016/j.jvir.2010.10.007.

[20] T. G. Schuster, J. T. Wei, K. Hendlin, R. Jahnke, and W. W. Roberts, "Histotripsy Treatment of Benign Prostatic Enlargement Using the Vortx Rx System: Initial Human Safety and Efficacy Outcomes," *Urology*, vol. 114, pp. 184–187, 2018, doi: https://doi.org/10.1016/j.urology.2017.12.033.

[21] M. Zupanc, Ž. Pandur, T. Stepišnik Perdih, D. Stopar, M. Petkovšek, and M. Dular, "Effects of cavitation on different microorganisms: The current understanding of the mechanisms taking place behind the phenomenon. A review and proposals for further research," *Ultrasonics Sonochemistry*, vol. 57, pp. 147–165, Oct. 2019, doi: 10.1016/j.ultsonch.2019.05.009.

[22] T. J. Matula *et al.*, "Treating Porcine Abscesses with Histotripsy: A Pilot Study," *Ultrasound in Medicine & Biology*, vol. 47, no. 3, pp. 603–619, Mar. 2021, doi: 10.1016/j.ultrasmedbio.2020.10.011.

[23] E. N. Harvey and A. L. Loomis, "THE DESTRUCTION OF LUMINOUS BACTERIA BY HIGH FREQUENCY SOUND WAVES," *J Bacteriol*, vol. 17, no. 5, pp. 373–376, May 1929, doi: 10.1128/jb.17.5.373-376.1929.

[24] R. Davies, "Observations on the use of ultrasound waves for the disruption of micro-organisms," *Biochimica et Biophysica Acta*, vol. 33, no. 2, pp. 481–493, Jun. 1959, doi: 10.1016/0006-3002(59)90138-6.

[25] R. G. Earnshaw, J. Appleyard, and R. M. Hurst, "Understanding physical inactivation processes: combined preservation opportunities using heat, ultrasound and pressure," *International Journal of Food Microbiology*, vol. 28, no. 2, pp. 197–219, Dec. 1995, doi: 10.1016/0168-1605(95)00057-7.

[26] J. Wu and W. L. Nyborg, "Ultrasound, cavitation bubbles and their interaction with cells," *Advanced Drug Delivery Reviews*, vol. 60, no. 10, pp. 1103–1116, Jun. 2008, doi: 10.1016/j.addr.2008.03.009.

[27] S. Gao, G. D. Lewis, M. Ashokkumar, and Y. Hemar, "Inactivation of microorganisms by low-frequency high-power ultrasound: 2. A simple model for the inactivation mechanism," *Ultrasonics Sonochemistry*, vol. 21, no. 1, pp. 454–460, Jan. 2014, doi: 10.1016/j.ultsonch.2013.06.007.

[28] S. Gao, Y. Hemar, M. Ashokkumar, S. Paturel, and G. D. Lewis, “Inactivation of bacteria and yeast using high-frequency ultrasound treatment,” *Water Research*, vol. 60, pp. 93–104, Sep. 2014, doi: 10.1016/j.watres.2014.04.038.

[29] G. T. Bokman, L. Biasiori-Poulanges, D. W. Meyer, and O. Supponen, “Scaling laws for bubble collapse driven by an impulsive shock wave,” *J. Fluid Mech.*, vol. 967, p. A33, Jul. 2023, doi: 10.1017/jfm.2023.514.

[30] P. Tho, R. Manasseh, and A. Ooi, “Cavitation microstreaming patterns in single and multiple bubble systems,” *J. Fluid Mech.*, vol. 576, pp. 191–233, Apr. 2007, doi: 10.1017/s0022112006004393.

[31] K. Johansen, J. H. Song, K. Johnston, and P. Prentice, “Deconvolution of acoustically detected bubble-collapse shock waves,” *Ultrasonics*, vol. 73, pp. 144–153, Jan. 2017, doi: 10.1016/j.ultras.2016.09.007.

[32] E. Joyce, A. Al-Hashimi, and T. J. Mason, “Assessing the effect of different ultrasonic frequencies on bacterial viability using flow cytometry: Effect of different ultrasonic frequencies on bacterial viability,” *Journal of Applied Microbiology*, vol. 110, no. 4, pp. 862–870, Apr. 2011, doi: 10.1111/j.1365-2672.2011.04923.x.

[33] R. A. Al-Juboori, V. Aravinthan, and T. Yusaf, “Impact of pulsed ultrasound on bacteria reduction of natural waters,” *Ultrasonics Sonochemistry*, vol. 27, pp. 137–147, Nov. 2015, doi: 10.1016/j.ultsonch.2015.05.007.

[34] G. Scherba, R. M. Weigel, and W. D. O’Brien, “Quantitative assessment of the germicidal efficacy of ultrasonic energy,” *Appl Environ Microbiol*, vol. 57, no. 7, pp. 2079–2084, Jul. 1991, doi: 10.1128/aem.57.7.2079-2084.1991.

[35] T. A. Bigelow, T. Northagen, T. M. Hill, and F. C. Sailer, “The Destruction of Escherichia Coli Biofilms Using High-Intensity Focused Ultrasound,” *Ultrasound in Medicine & Biology*, vol. 35, no. 6, pp. 1026–1031, Jun. 2009, doi: 10.1016/j.ultrasmedbio.2008.12.001.

[36] T. A. Bigelow, C. L. Thomas, and H. Wu, “Scan Parameter Optimization for Histotripsy Treatment of *S. Aureus* Biofilms on Surgical Mesh,” *IEEE Trans. Ultrason., Ferroelect., Freq. Contr.*, vol. 67, no. 2, pp. 341–349, Feb. 2020, doi: 10.1109/TUFFC.2019.2948305.

[37] J. Xu, T. A. Bigelow, L. J. Halverson, J. M. Middendorf, and B. Rusk, “Minimization of treatment time for in vitro 1.1MHz destruction of Pseudomonas aeruginosa biofilms by high-intensity focused ultrasound,” *Ultrasonics*, vol. 52, no. 5, pp. 668–675, Jul. 2012, doi:

10.1016/j.ultras.2012.01.013.

[38] A. C. Vollmer, S. Kwakye, M. Halpern, and E. C. Everbach, “Bacterial Stress Responses to 1-Megahertz Pulsed Ultrasound in the Presence of Microbubbles,” *Appl Environ Microbiol*, vol. 64, no. 10, pp. 3927–3931, Oct. 1998, doi: 10.1128/AEM.64.10.3927-3931.1998.

[39] A. A. Brayman *et al.*, “Inactivation of Planktonic Escherichia coli by Focused 2-MHz Ultrasound,” *Ultrasound in Medicine & Biology*, vol. 43, no. 7, pp. 1476–1485, Jul. 2017, doi: 10.1016/j.ultrasmedbio.2017.03.009.

[40] A. A. Brayman *et al.*, “Inactivation of Planktonic Escherichia coli by Focused 1-MHz Ultrasound Pulses with Shocks: Efficacy and Kinetics Upon Volume Scale-Up,” *Ultrasound in Medicine & Biology*, vol. 44, no. 9, pp. 1996–2008, Sep. 2018, doi: 10.1016/j.ultrasmedbio.2018.05.010.

[41] R. Morse, C. Childers, E. Nowak, J. Rao, and E. Vlaisavljevich, “Catheter-Based Medical Device Biofilm Ablation Using Histotripsy: A Parameter Study,” *Ultrasound in Medicine & Biology*, vol. 49, no. 9, pp. 2152–2159, Sep. 2023, doi: 10.1016/j.ultrasmedbio.2023.06.010.

[42] A. D. Maxwell *et al.*, “A Prototype Therapy System for Transcutaneous Application of Boiling Histotripsy,” *IEEE Trans. Ultrason., Ferroelect., Freq. Contr.*, vol. 64, no. 10, pp. 1542–1557, Oct. 2017, doi: 10.1109/TUFFC.2017.2739649.

[43] P. B. Rosnitskiy *et al.*, “Design of HIFU Transducers for Generating Specified Nonlinear Ultrasound Fields,” *IEEE Trans. Ultrason., Ferroelect., Freq. Contr.*, vol. 64, no. 2, pp. 374–390, Feb. 2017, doi: 10.1109/TUFFC.2016.2619913.

[44] T. Li *et al.*, “Passive Cavitation Detection during Pulsed HIFU Exposures of Ex Vivo Tissues and In Vivo Mouse Pancreatic Tumors,” *Ultrasound in Medicine & Biology*, vol. 40, no. 7, pp. 1523–1534, Jul. 2014, doi: 10.1016/j.ultrasmedbio.2014.01.007.

[45] P. A. Ambekar *et al.*, “Comparative Study of Histotripsy Pulse Parameters Used to Inactivate Escherichia coli in Suspension,” *Ultrasound in Medicine & Biology*, vol. 49, no. 12, pp. 2451–2458, Dec. 2023, doi: 10.1016/j.ultrasmedbio.2023.08.004.

[46] Y. Nanda Kumar *et al.*, “Development of Tough Hydrogel Phantoms to Mimic Fibrous Tissue for Focused Ultrasound Therapies,” *Ultrasound in Medicine & Biology*, vol. 48, no. 9, pp. 1762–1777, Sep. 2022, doi: 10.1016/j.ultrasmedbio.2022.05.002.

[47] C. Edsall, E. Ham, H. Holmes, T. L. Hall, and E. Vlaisavljevich, “Effects of frequency on bubble-cloud behavior and ablation efficiency in intrinsic threshold histotripsy,” *Phys. Med.*

Biol., vol. 66, no. 22, p. 225009, Nov. 2021, doi: 10.1088/1361-6560/ac33ed.

[48] Z. Xu, T. L. Hall, J. B. Fowlkes, and C. A. Cain, "Effects of acoustic parameters on bubble cloud dynamics in ultrasound tissue erosion (histotripsy)," *J. Acoust. Soc. Am.*, vol. 122, no. 1, pp. 229–236, Jul. 2007, doi: 10.1121/1.2735110.

[49] K.-W. Lin *et al.*, "Histotripsy beyond the intrinsic cavitation threshold using very short ultrasound pulses: microtripsy," *IEEE Trans. Ultrason., Ferroelect., Freq. Contr.*, vol. 61, no. 2, pp. 251–265, Feb. 2014, doi: 10.1109/TUFFC.2014.6722611.

[50] M. S. Canney, M. R. Bailey, L. A. Crum, V. A. Khokhlova, and O. A. Sapozhnikov, "Acoustic characterization of high intensity focused ultrasound fields: A combined measurement and modeling approach," *The Journal of the Acoustical Society of America*, vol. 124, no. 4, pp. 2406–2420, Oct. 2008, doi: 10.1121/1.2967836.

[51] P. V. Yuldashev, M. M. Karzova, W. Kreider, P. B. Rosnitskiy, O. A. Sapozhnikov, and V. A. Khokhlova, "'HIFU Beam:' A Simulator for Predicting Axially Symmetric Nonlinear Acoustic Fields Generated by Focused Transducers in a Layered Medium," *IEEE Trans. Ultrason., Ferroelect., Freq. Contr.*, vol. 68, no. 9, pp. 2837–2852, Sep. 2021, doi: 10.1109/TUFFC.2021.3074611.

[52] A. D. Maxwell, C. A. Cain, A. P. Duryea, L. Yuan, H. S. Gurm, and Z. Xu, "Noninvasive Thrombolysis Using Pulsed Ultrasound Cavitation Therapy – Histotripsy," *Ultrasound in Medicine & Biology*, vol. 35, no. 12, pp. 1982–1994, Dec. 2009, doi: 10.1016/j.ultrasmedbio.2009.07.001.

[53] H. T. O'Neil, "Theory of Focusing Radiators," *The Journal of the Acoustical Society of America*, vol. 21, no. 5, pp. 516–526, Sep. 1949, doi: 10.1121/1.1906542.

[54] R. P. Williams, J. C. Simon, V. A. Khokhlova, O. A. Sapozhnikov, and T. D. Khokhlova, "The histotripsy spectrum: differences and similarities in techniques and instrumentation," *International Journal of Hyperthermia*, vol. 40, no. 1, p. 2233720, Dec. 2023, doi: 10.1080/02656736.2023.2233720.

[55] P. A. Ambekar *et al.*, "Histotripsy-Induced Bactericidal Activity Correlates to Size of Cavitation Cloud In Vitro," *IEEE Transactions on Ultrasonics, Ferroelectrics, and Frequency Control*, vol. 71, no. 12: Breaking the Resolution Barrier in Ultrasound, pp. 1868–1878, Dec. 2024, doi: 10.1109/TUFFC.2024.3476438.

[56] J. R. Blake, D. M. Leppinen, and Q. Wang, "Cavitation and bubble dynamics: the Kelvin

impulse and its applications," *Interface Focus.*, vol. 5, no. 5, p. 20150017, Oct. 2015, doi: 10.1098/rsfs.2015.0017.

[57] M. Song *et al.*, "Quantitative Assessment of Boiling Histotripsy Progression Based on Color Doppler Measurements," *IEEE Trans. Ultrason., Ferroelect., Freq. Contr.*, vol. 69, no. 12, pp. 3255–3269, Dec. 2022, doi: 10.1109/TUFFC.2022.3212266.

[58] E. Vlaisavljevich, A. Maxwell, L. Mancia, E. Johnsen, C. Cain, and Z. Xu, "Visualizing the Histotripsy Process: Bubble Cloud–Cancer Cell Interactions in a Tissue-Mimicking Environment," *Ultrasound in Medicine & Biology*, vol. 42, no. 10, pp. 2466–2477, Oct. 2016, doi: 10.1016/j.ultrasmedbio.2016.05.018.

[59] K. B. Bader, S. A. Hendley, G. J. Anthony, and V. Bollen, "Observation and modulation of the dissolution of histotripsy-induced bubble clouds with high-frame rate plane wave imaging," *Phys. Med. Biol.*, vol. 64, no. 11, p. 115012, May 2019, doi: 10.1088/1361-6560/ab1a64.

[60] V. V. Trivedi, E. L. Wallach, K. B. Bader, and H. Shekhar, "Contrast-Enhanced Imaging of Histotripsy Bubble Clouds Using Chirp-Coded Excitation and Volterra Filtering," *IEEE Trans. Ultrason., Ferroelect., Freq. Contr.*, vol. 70, no. 9, pp. 989–998, Sep. 2023, doi: 10.1109/TUFFC.2023.3289918.

[61] P. Kim, S. Bae, J. H. Song, and T. Song, "Comparison study of passive acoustic mapping and high-speed photography for monitoring *in situ* cavitation bubbles," *The Journal of the Acoustical Society of America*, vol. 145, no. 6, pp. EL604–EL610, Jun. 2019, doi: 10.1121/1.5113961.

[62] Q. Wu *et al.*, "Challenges in classifying cavitation: correlating high-speed optical imaging and passive acoustic mapping of cavitation dynamics," *The Journal of the Acoustical Society of America*, 2024.

[63] F. D. Lowy, "Staphylococcus aureus Infections," *The New England Journal of Medicine*, 1998.

[64] M. L. Landrum *et al.*, "Epidemiology of Staphylococcus aureus Blood and Skin and Soft Tissue Infections in the US Military Health System, 2005-2010," *JAMA*, vol. 308, no. 1, pp. 50–59, Jul. 2012, doi: 10.1001/jama.2012.7139.

[65] Moran Gregory J. *et al.*, "Methicillin-Resistant S. aureus Infections among Patients in the Emergency Department," *New England Journal of Medicine*, vol. 355, no. 7, pp. 666–674,

doi: 10.1056/NEJMoa055356.

[66] B. Rieck *et al.*, “Focused ultrasound treatment of abscesses induced by methicillin resistant *Staphylococcus aureus* : Feasibility study in a mouse model: Feasibility of MRSA abscesses FUS treatment,” *Med. Phys.*, vol. 41, no. 6Part1, p. 063301, May 2014, doi: 10.1118/1.4875692.

[67] N. C. Sesal and O. Kekec, “Effects of pulsed ultrasound on Escherichia coli and Staphylococcus aureus,” *Transactions of the Royal Society of Tropical Medicine and Hygiene*, vol. 108, no. 6, pp. 348–353, Jun. 2014, doi: 10.1093/trstmh/tru052.

[68] E. Joyce, S. S. Phull, J. P. Lorimer, and T. J. Mason, “The development and evaluation of ultrasound for the treatment of bacterial suspensions. A study of frequency, power and sonication time on cultured Bacillus species,” *Ultrasonics Sonochemistry*, vol. 10, no. 6, pp. 315–318, Oct. 2003, doi: 10.1016/S1350-4177(03)00101-9.

[69] A. A. Tahi, S. Sousa, K. Madani, C. L. M. Silva, and F. A. Miller, “Ultrasound and heat treatment effects on Staphylococcus aureus cell viability in orange juice,” *Ultrasonics Sonochemistry*, vol. 78, p. 105743, Oct. 2021, doi: 10.1016/j.ultsonch.2021.105743.

[70] J. Li *et al.*, “Analysis of Staphylococcus aureus cell viability, sublethal injury and death induced by synergistic combination of ultrasound and mild heat,” *Ultrasonics Sonochemistry*, vol. 39, pp. 101–110, Nov. 2017, doi: 10.1016/j.ultsonch.2017.04.019.

[71] M. H. Dehghani, “Effectiveness of Ultrasound on the Destruction of E. coli,” *American J. of Environmental Sciences*, vol. 1, no. 3, pp. 187–189, Mar. 2005, doi: 10.3844/ajessp.2005.187.189.

[72] I. Álvarez, P. Mañas, F. J. Sala, and S. Condón, “Inactivation of *Salmonella enterica* Serovar Enteritidis by Ultrasonic Waves under Pressure at Different Water Activities,” *Appl Environ Microbiol*, vol. 69, no. 1, pp. 668–672, Jan. 2003, doi: 10.1128/AEM.69.1.668-672.2003.

[73] N. G. Stoforos, “Thermal Process Calculations Through Ball’s Original Formula Method: A Critical Presentation of the Method and Simplification of its Use Through Regression Equations,” *Food Eng. Rev.*, vol. 2, no. 1, pp. 1–16, Mar. 2010, doi: 10.1007/s12393-010-9014-4.

[74] K. Kieran *et al.*, “Refining Histotripsy: Defining the Parameter Space for the Creation of Nonthermal Lesions With High Intensity, Pulsed Focused Ultrasound of the In Vitro Kidney,”

Journal of Urology, vol. 178, no. 2, pp. 672–676, Aug. 2007, doi: 10.1016/j.juro.2007.03.093.

[75] H. Hassan, C. F. Iskandar, R. Hamzeh, N. J. Malek, A. El Khoury, and M. G. Abiad, "Heat resistance of *Staphylococcus aureus, Salmonella* sp., and *Escherichia coli* isolated from frequently consumed foods in the Lebanese market," *International Journal of Food Properties*, vol. 25, no. 1, pp. 2435–2444, Dec. 2022, doi: 10.1080/10942912.2022.2143521.

[76] J. Kennedy, I. S. Blair, D. A. McDowell, and D. J. Bolton, "An investigation of the thermal inactivation of Staphylococcus aureus and the potential for increased thermotolerance as a result of chilled storage," *J Appl Microbiol*, vol. 99, no. 5, pp. 1229–1235, Nov. 2005, doi: 10.1111/j.1365-2672.2005.02697.x.

[77] J. J. Iandolo and Z. J. Ordal, "Repair of Thermal Injury of *Staphylococcus aureus*," *J Bacteriol*, vol. 91, no. 1, pp. 134–142, Jan. 1966, doi: 10.1128/jb.91.1.134-142.1966.

[78] Z. Herceg, A. R. Jambrak, V. Lelas, and S. M. Thagard, "The Effect of High Intensity Ultrasound Treatment on the Amount of Staphylococcus aureus and Escherichia coli in Milk," 2012.

[79] J. W. Shaevitz, "Microbiology: Peeling Back the Layers of Bacterial Envelope Mechanics," *Current Biology*, vol. 28, no. 20, pp. R1210–R1211, Oct. 2018, doi: 10.1016/j.cub.2018.09.023.

[80] A. Typas, M. Banzhaf, C. A. Gross, and W. Vollmer, "From the regulation of peptidoglycan synthesis to bacterial growth and morphology," *Nat Rev Microbiol*, vol. 10, no. 2, pp. 123–136, Feb. 2012, doi: 10.1038/nrmicro2677.

[81] Ž. Pandur, M. Dular, R. Kostanjšek, and D. Stopar, "Bacterial cell wall material properties determine E. coli resistance to sonolysis," *Ultrasonics Sonochemistry*, vol. 83, p. 105919, Feb. 2022, doi: 10.1016/j.ultsonch.2022.105919.

[82] R. T. Ellison and T. J. Giehl, "Killing of gram-negative bacteria by lactoferrin and lysozyme.," *J. Clin. Invest.*, vol. 88, no. 4, pp. 1080–1091, Oct. 1991, doi: 10.1172/JCI115407.

[83] E. Berg, "A new spin on the old gram stain," *Chemical Engineering News*, Apr. 28, 2015.

[84] S. Drakopoulou, S. Terzakis, M. S. Fountoulakis, D. Mantzavinos, and T. Manios, "Ultrasound-induced inactivation of gram-negative and gram-positive bacteria in secondary treated municipal wastewater," *Ultrasonics Sonochemistry*, vol. 16, no. 5, pp. 629–634, Jun. 2009, doi: 10.1016/j.ultsonch.2008.11.011.

[85] T. Monsen, E. Lövgren, M. Widerström, and L. Wallinder, "In Vitro Effect of Ultrasound

on Bacteria and Suggested Protocol for Sonication and Diagnosis of Prosthetic Infections," *J Clin Microbiol*, vol. 47, no. 8, pp. 2496–2501, Aug. 2009, doi: 10.1128/JCM.02316-08.

[86] H. Alliger, "Ultrasonic disruption," *American Laboratory*, vol. 7, no. 10, pp. 75–85, Oct. 1975.

[87] M. Cameron, L. D. McMaster, and T. J. Britz, "Electron microscopic analysis of dairy microbes inactivated by ultrasound," *Ultrasonics Sonochemistry*, vol. 15, no. 6, pp. 960–964, Sep. 2008, doi: 10.1016/j.ultsonch.2008.02.012.

[88] J. Zevnik and M. Dular, "Cavitation bubble interaction with compliant structures on a microscale: A contribution to the understanding of bacterial cell lysis by cavitation treatment," *Ultrasonics Sonochemistry*, vol. 87, p. 106053, Jun. 2022, doi: 10.1016/j.ultsonch.2022.106053.

[89] J. M. Gere, "Mechanics of Materials, Brief ed.," 2011.

[90] J. M. Monteiro *et al.*, "The pentaglycine bridges of Staphylococcus aureus peptidoglycan are essential for cell integrity," *Sci Rep*, vol. 9, no. 1, p. 5010, Mar. 2019, doi: 10.1038/s41598-019-41461-1.

[91] E. L. Carstensen *et al.*, "Lysis of erythrocytes by exposure to CW ultrasound," *Ultrasound in Medicine & Biology*, vol. 19, no. 2, pp. 147–165, Jan. 1993, doi: 10.1016/0301-5629(93)90007-b.

[92] M. Cameron, "Impact of low-frequency high-power ultrasound on spoilage and potentially pathogenic dairy microbes".

[93] G. Kozmus, J. Zevnik, M. Hočevar, M. Dular, and M. Petkovšek, "Characterization of cavitation under ultrasonic horn tip – Proposition of an acoustic cavitation parameter," *Ultrasonics Sonochemistry*, vol. 89, p. 106159, Sep. 2022, doi: 10.1016/j.ultsonch.2022.106159.

[94] J. Zevnik and M. Dular, "Cavitation bubble interaction with a rigid spherical particle on a microscale," *Ultrasonics Sonochemistry*, vol. 69, p. 105252, Dec. 2020, doi: 10.1016/j.ultsonch.2020.105252.

[95] J. Zevnik and M. Dular, "Liposome destruction by a collapsing cavitation microbubble: A numerical study," *Ultrasonics Sonochemistry*, vol. 78, p. 105706, Oct. 2021, doi: 10.1016/j.ultsonch.2021.105706.

[96] M. Lokhandwalla and B. Sturtevant, "Mechanical haemolysis in shock wave lithotripsy

(SWL): I. Analysis of cell deformation due to SWL flow-fields," *Phys. Med. Biol.*, vol. 46, no. 2, pp. 413–437, Feb. 2001, doi: 10.1088/0031-9155/46/2/310.

APPENDIX A

Derivation of the equation of volume of an axially symmetric ellipsoid as a function of major axis and cross-sectional area along the plane passing through major and any of the minor axes.

Let a,b,c be the semi-axis of an ellipsoid, with 'a' being the longest (or semi-major) axis. Let the major axis (cavitation cloud height) be h. The ellipsoid considered is axially symmetric, hence b = c. 'A' is the area of the cross-section of the ellipsoid along a-b plane. Let V be the ellipsoid volume.

$V = \frac{4}{3}\pi abc$ (1)

$V = \frac{4}{3}\pi ab^2$ (since b = c)

The area of an ellipse is:-

$A = \pi ab$

Which means,

$b = \frac{A}{\pi a}$ (2)

Substituting equation (2) in (1),

$V = \frac{4}{3}\pi a \frac{A^2}{\pi^2 a^2}$

$V = \frac{4A^2}{3\pi a}$ (3)

The major axis (cavitation cloud height) is:-

$h = 2a$ (4)

Substituting (4) in (3)

$V = \frac{8A^2}{3\pi h}$

APPENDIX B

Following is the process of obtaining z-value from heat control studies. Log kill values at 40-minute treatments at 50°C and 52.5°C were used. Assumptions were that thermal inactivation kinetics (i.e. time dependence) were linear, and the minutes to reach the target temperature were not considered. Following these assumptions, D-value was calculated for each temperature. The magnitude of the reciprocal of the slope of the plot of log D vs temperature is the z-value, which was 8.33^0C.

Temperature (^{0}C)	Minutes to reach temperature	Minutes at temperature	Kill	D value	Log D
50	5	35	2.49	14.05	1.14
52.5	7	33	4.68	7.04	0.84

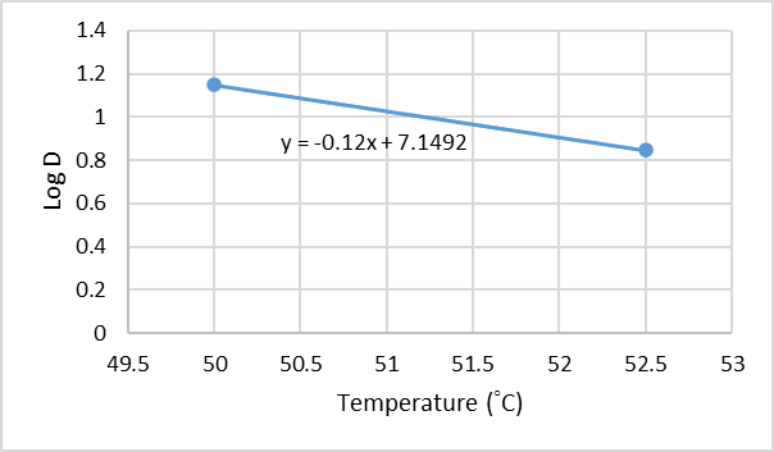

Figure. Thermal destruction (TD) curve for Staphylococcus USA300 in 3% tryptic soy broth.

APPENDIX C

Design and fabrication of ballistic gel sample holder used in chapter 6. Credit – Mr. Kaizer Contreras

Design

A novel high temperature compression mold was constructed for in-house fabrication of an acoustically transparent sample holder. Utilizing rapid prototyping manufacturing and off the shelf products. The final part is constructed from 10% Ballistic Gel (ClearBallistics, Greenville, SC, USA).

Ballistic gel

Ballistic Gel is a well-documented material for the use in studying acoustics. With a measured speed of sound of 1537 ± 39 m/s and density similar to water , and an impedance of 1.07 dB/cm at 1MHz (Alves A.K., 2020, UMB). Other groups have confirmed that their measurements fall within 6% of that of soft tissue (Sjostrand, 2020, UMB). These properties make it an excellent material for creating phantoms. In this application, we are taking advantage of its acoustic transparency, gel stability for repeated use, and ability to re-create complex geometry.

3D Modeling

In Solidworks 3D CAD (Dassault Systèmes SolidWorks Corp., Waltham, Massachusetts, USA), a compression mold was designed, shown in the Figure below. The part produced is being designed to fit within a cylindrical sample vial. With this tool we can create smaller volumes without occluding the transducer beam path.

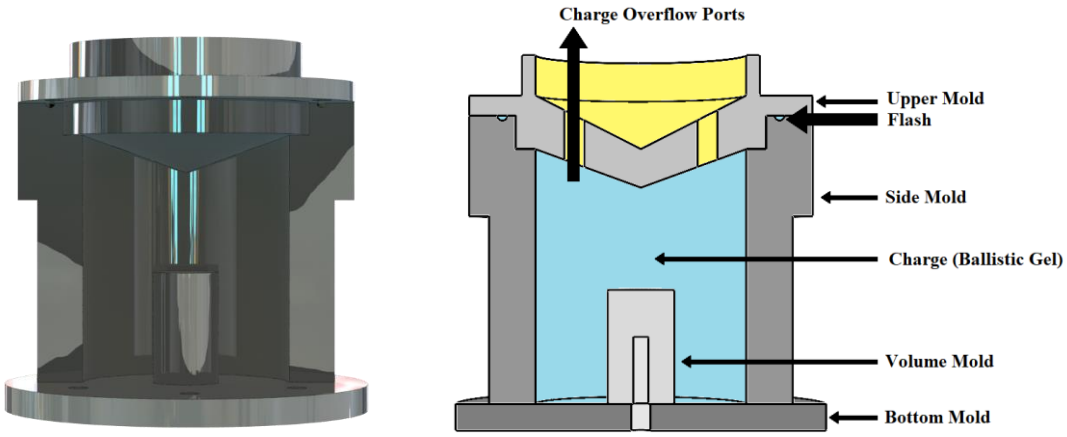

Figure. 3D Render of compression mold assembled with one side removed to show interior (Left) 2D Cross section of compression mold with labels on each part. (Right)

Material Selection

In prototyping a rapid system to create high temperature volumetric molds, aluminum cylinders and rods were first explored. This mold could not be separated without damaging the part, so aluminum foil was added and used to line the edges of the cylinder and create a lining that could be separated. As the texture of the aluminum foil would transfer to the sides of the part it would not be appropriate for this experiment where precision is required (see Figure below), and where complex shapes need to be produced. High Temp Resin (Formlabs, Somerville, MA, USA) was explored as a rapid prototyping tooling material which could be manufactured to any shape and is within our lab's production capabilities. This material has a heat deflection temperature of 238 °C at 0.45 MPa, as specified in the manufacturer's documentation. Our maximum runaway temperature is 150°C. This is the material used in the molds.

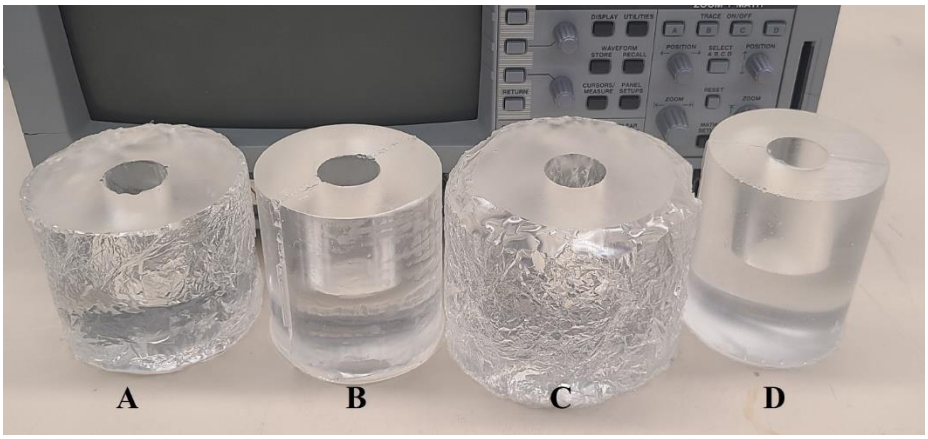

Figure. Contact surface material effect on surface finish. A: Medium outer diameter with aluminum foil. B: 3D printed mold with brushed on UV resin glossy coat. C: Large outer diameter with aluminum foil. D: 3D printed mold without release agent, standard quality.

Part Preparation Steps

1. Ballistic gel is melted in a large aluminum vat inside a vacuum oven at 150°C.

2. The gel is degassed until no bubbles remain.

3. Any small bubbles are removed with an aluminum spatula

4. The high temperature mold is placed into the oven to reach equal temperature as the gel.

5. The ballistic gel is poured into the heated high temp mold, acting as a charge and the upper mold is bolted to the body of the mold.

6. The mold is allowed to cool overnight.

7. The mold is separated into parts to retrieve the final part.

VITA

Pratik Ambekar received his B.E. degree in mechanical engineering from Savitribai Phule Pune University, Pune, India, in 2018, and the M.S. degree in mechanical engineering from the University of Washington, Seattle, WA, USA, in 2021, where he is currently pursuing his Ph.D. degree. His research interests include histotripsy-induced bacterial inactivation. He served as the student representative for the Technical Committee on Engineering Acoustics of the Acoustical Society of America from 2022 to 2024.